Experimental investigation of topological insulators and superconductors

ACADEMISCH PROEFSCHRIFT

ter verkrijging van de graad van doctor
aan de Universiteit van Amsterdam
op gezag van de Rector Magnificus
prof. dr. ir. K.I.J. Maex
ten overstaan van een door het College voor Promoties ingestelde
commissie, in het openbaar te verdedigen in de Agnietenkapel
op woensdag 02 november 2016, te 14:00 uur

door

Yu Pan

geboren te Sichuan, China

Promotiecommissie:

Promotor:	Prof. dr. M.S. Golden, Universiteit van Amsterdam
Copromotor:	Dr. A. de Visser, Universiteit van Amsterdam
Overige leden:	Prof. dr. A. Brinkman, Universiteit Twente
	Prof. dr. T. Gregorkiewicz, Universiteit van Amsterdam
	Prof. dr. C.J.M. Schoutens, Universiteit van Amsterdam
	Prof. dr. F. Schreck, Universiteit van Amsterdam
	Dr. U. Zeitler, Radboud Universiteit

Faculteit der Natuurwetenschappen, Wiskunde en Informatica

The research reported in this thesis was carried out at the Van der Waals-Zeeman Institute, Institute of Physics, University of Amsterdam. This work was part of the research programme of the Foundation for Fundamental Research on Matter (FOM), which is part of the Netherlands Organisation for Scientific Research (NWO).

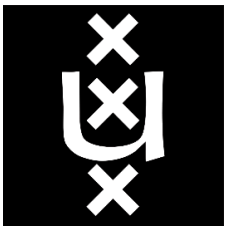

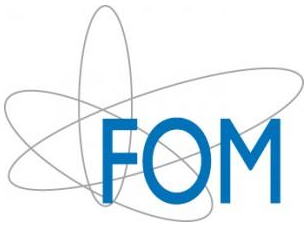

Cover picture taken from NL Architects for an ideas competition on the Hong Kong-Zhuhai-Macau Bridge
Experimental investigation of topological insulators and superconductors
Ph.D. thesis, University of Amsterdam
Printed by: Ipskamp Printing
ISBN: 978-94-028-0357-0

Contents

Chapter 1

Introduction

1.1 General introduction

Topological insulators (TIs) represent an exotic state of quantum matter. TI crystals act as a normal insulator with a gapped band structure in the interior, while the boundary hosts peculiar metallic edge or surface states. The edge or surface states are immune to back scattering by non-magnetic impurities and crystal defects due to the combination of time reversal symmetry and spin orbit interaction. Besides, they exhibit spin-moment locking and possess a π Berry phase. The discovery of TIs has initiated a surge of research activities because of novel theoretical ideas and potential technological applications, such as the topological magnetoelectric effect, Majorana fermions and fault-tolerant quantum computation [1–3].

The story of the TIs can be traced back to the discovery of the integer quantum Hall effect (IQHE) by von Klitzing *et al.* in 1980 [4]. Two-dimensional (2D) electrons subjected to low temperatures and strong magnetic fields show a vanishing longitudinal conductivity σ_{xx} together with a quantized Hall conductivity $\sigma_{xy} = N\frac{e^2}{h}$, where N is an integer, e is the electron charge and h is Planck's constant. The quantization of the Hall conductivity obviously points to a quantum phenomenon. Interestingly, this state does not show any symmetry breaking, which has been the conventional approach to classify distinctive quantum phases of matter in condensed matter physics in the last century. In 1982, Thouless, Kohmoto, Nightingale and den Nijs (TKNN) [5] showed that the IQHE is not only a quantum mechanical phenomenon but also a topological one, which facilitated the emergence of a completely different characterization of quantum phases based on the concept of topology. Topology was first used by mathematicians to classify different geometrical objects and is essentially the study of classes of objects invariant under smooth deformations. For example, a coffee cup is topologically equivalent to a doughnut but topologically distinct from an orange; a coffee cup can be smoothly reshaped into a doughnut without closing or poking a hole, but this is not possible for the orange. Analogously, the concept of topology can be extended to classify band structures in physics. If Bloch Hamiltonians can be smoothly deformed into each other, they are topologically equivalent and belong to the same topological class with a defined topological invariant. In the case of a quantum Hall system, the TKNN invariant specifies its topology which is characteristic of a 2D system with broken time reversal symmetry (TRS), in this case, because of the magnetic field.

In 2005 and 2006, Kane and Mele [6] and Bernevig and Zhang [7] independently proposed the idea of the quantum spin Hall (QSH) insulator, which is essentially two copies of the quantum Hall system with two spin polarized edge states to preserve TRS. In principle the QSH insulator can be realized in certain theoretical models with spin-orbit coupling (SOC). Soon thereafter, Bernevig, Hughes and Zhang [8] theoretically predicted that a QSH phase can be realized in CdTe/HgTe/CdTe quantum wells (QWs). In 2007

König *et al.* verified this prediction with the experiment observation that G_{xx} is quantized to $2e^2/h$ (the conductance of a pair of edge channels) in zero magnetic field [9]. In terms of topology, the QSH insulator is topologically different from a QH system and the former is characterized by the $\mathbb{Z}_2$ topological invariant ν, which can take the value 0 or 1 [10]. This value classifies the topological character of systems: $\nu = 0$ means that the system is topologically trivial, whereas $\nu = 1$ means that the system is topologically nontrivial and has topologically protected edge states (resulting from SOC rather than from a magnetic field). For the QSH insulator, ν takes the value of 1. A QSH insulator is called a 2D topological insulator.

Before the experimental verification of 2D topological insulators, theorists generalized the topological classification to 3D systems, where four $\mathbb{Z}_2$ topological invariants $(\nu_0, \nu_1, \nu_2, \nu_3)$ are used to characterize the topology [11–13]. By layering 2D topological insulators, a 3D version of a topological insulator can be constructed, similar to the construction of the QSH insulator from QH states. However, this layered state is not stable to disorder and is referred to as a weak topological insulator with index $\nu_0 = 0$. The genuine 3D topological insulator, also called a strong topological insulator, has an index value $\nu_0 = 1$. In 2007, Fu and Kane theoretically predicted that the $Bi_{1-x}Sb_x$ alloy with x ranging from 0.07 to 0.22 should be a strong topological insulator [14]. This prediction was experimentally confirmed in 2008 by Hsieh *et al.* by mapping the unusual surface band structure of $Bi_{0.9}Sb_{0.1}$ (111) using angle-resolved photoemission spectroscopy (ARPES) [15]. Given the importance of topological insulators as new quantum states of matter, together with the rather complicated surface structure and small band gap of $Bi_{1-x}Sb_x$ alloys, this motivated an extensive search for topological insulators with a simple surface structure and large band gap. In 2009, Zhang *et al.* theoretically predicted via first-principles electronic structure calculations that Bi_2Se_3, Bi_2Te_3, and Sb_2Te_3 are 3D topological insulators, whereas Sb_2Se_3 is not [16]. Especially, for Bi_2Se_3 the calculation predicted that its surface state is a nearly ideal single Dirac cone and that the bulk band gap is around 0.3 eV, sufficiently large for applications [16]. Indeed, ARPES experiments conducted by Xia *et al.* in 2009 confirmed the theoretical predictions [17]. **Figure** 1.1 shows (a) the surface electronic band dispersion on the (111) surface of Bi_2Se_3 measured using high-resolution ARPES and (b) the schematic of the spin texture based on spin-resolved ARPES data. The spin-polarized surface states cross the bulk band gap and enclose a single Dirac point centered at $\bar{\Gamma}$. These theoretical predictions and experimental results opened up the exciting field of topological insulators and generated a lot of research activity aimed at addressing topological phases of matter.

The 3D topological insulators Bi_2Se_3, Bi_2Te_3 and Sb_2Te_3, which are called second generation 3D topological insulators, became ideal model systems and have been investigated widely. These materials all crystallize in the rhombohedral structure with the space group $R\bar{3}m$. Here we take Bi_2Se_3 as an example, of which the crystal structure is

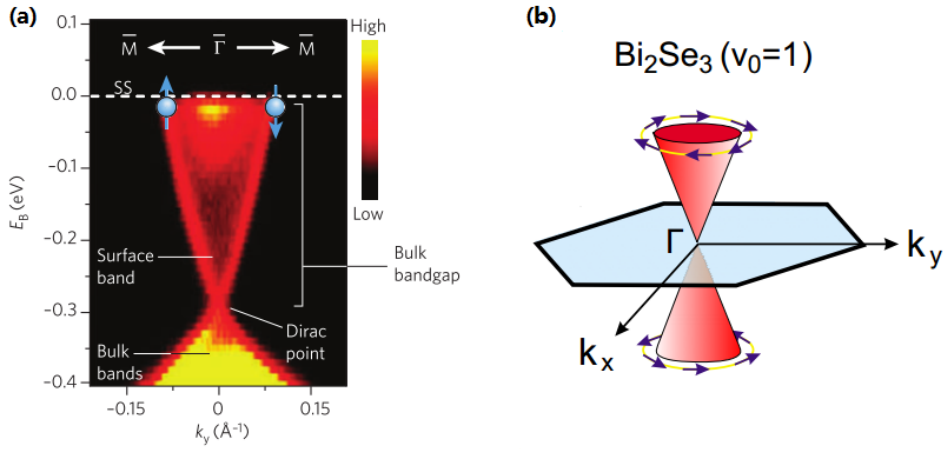

Figure 1.1: *(a) The surface electronic band dispersion on the (111) surface of Bi_2Se_3 measured by high-resolution ARPES with an incident photon energy of 22 eV along $\bar{\Gamma} - \bar{M}$, showing a clear Dirac cone. (b) the schematic of the spin texture (blue arrows) based on spin-resolved ARPES data. Figures taken from Refs. [2, 17] and [1, 18].*

shown in **Figure** 1.2. It possesses a layered structure built up of quintuple layers (QLs) consisting of a stack of Se – Bi – Se – Bi – Se atomic layers. The QL has a thickness of about 1 nm, and acts as the very building block of the structure. Three QLs stack sequently to give the unit cell with a thickness of ∼3 nm. The covalent bonding between the atomic layers within one QL is much stronger than the van der Waals bonding between two QLs, therefore, the crystals cleave at the interface of two QLs. In spite of the unambiguous characterization of the topological surface states of these materials with the help of surface-sensitive techniques, such as ARPES and Scanning-Tunneling Microscopy (STM) [18–22], the transport properties of the surface states, which are fundamentally interesting and useful for future device applications, turn out to be difficult to measure due to the inherent large bulk conductivity in single crystals of these materials [23–25]. For example, crystals nominally stoichiometric Bi_2Te_3 show a surface contribution of only 0.3% to the total transport response, according to measurements of Shubnikov-de Haas (SdH) oscillations [24]. In order to achieve a truly bulk-insulating state in a TI material, it is crucial to engineer a small residual bulk carrier density and/or mobility. A successful approach in this respect has proven to be chemical substitution. Bi_2Se_3 is mostly n-type due to Se vacancies and Bi_2Te_3 mainly behaves as p-type owing to anti-site defects between Bi and Te. A logical solution is to combine both materials. Experiments showed that the optimal combination is Bi_2Te_2Se (BTS) and its resistivity values exceed 1 Ωcm [26] and the surface contribution amounts to 6% of the total transport [27, 28]. Ren *et al.* showed that BTS can be further optimized by introducing Sb on the Bi positions together with reducing the Te:Se ratio. The result of the optimization is shown in **Figure** 1.3. Fixing the Sb content x and optimizing the Se content y for x yields the optimal composition

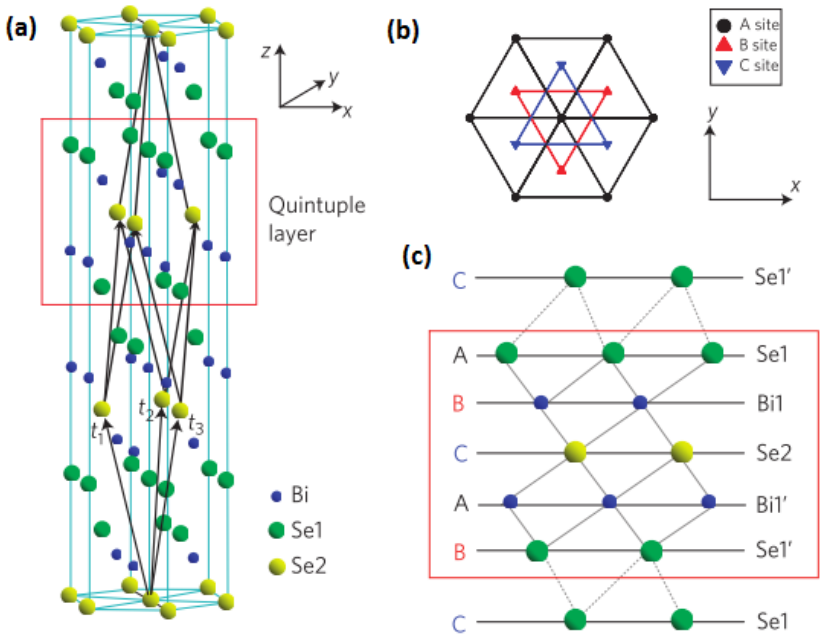

Figure 1.2: *(a) Crystal structure of Bi_2Se_3. $\boldsymbol{t}_{1,2,3}$ represent three primitive lattice vectors. The quintuple layer (QL) with Se1 – Bi1 – Se2 – Bi1' – Se1' enclosed by the red square is the main building block of the structure. The unit cell is comprised of a stack of 3 QLs. (b) Top view along the* z*-direction. There are three different positions, A, B and C, in one QL of the triangle lattice. (c) Side view of the QL structure. The stacking of the QLs are in the – A(Se1) – B(Bi1) – C(Se2) – A(Bi1') – B(Se1') – manner along the z-direction. The structure possesses inversion symmetry, that is, Se2 atoms act as inversion center and invert the Se1(Bi1) layer to the Se1' (Bi1') layer. Figures taken from Ref. [16].*

$Bi_{1.5}Sb_{0.5}Te_{1.7}Se_{1.3}$ [29]. The material shows high bulk resistivity values and surface dominated transport, in which the surface contribution is as high as 70% [30].

Besides the widespread research on Bi-based materials, a great effort has been made to discover new topological materials, such as selected half-Heusler compounds. Half-Heusler compounds with chemical formula XYZ are derived from Heusler compounds X_2YZ named after Fritz Heusler who discovered the first Heusler compound Cu_2MnAl in 1903 [32]. Half-Heusler compounds crystallize in a non-centrosymmetric cubic structure with space group $F\bar{4}3m$. The crystal structure is shown in **Figure** 1.4(c). It can be derived by combining an ionic rock salt-type structure (**Figure** 1.4(a), similar to that of NaCl) formed by X and Z atoms and a covalent Zinc blende-type structure (**Figure** 1.4(b), similar to that of HgTe) formed by Y and Z atoms. The X, Y and Z atoms occupy the 4b, 4c and 4a Wyckoff positions in the unit cell, respectively. Normally, X and Y are transition or rare earth elements and Z is a heavy element. Half-Heusler compounds possess inherent flexibility in the size of the unit cell and large variability in the composition, which allows for tunable functions in the fields of spintronics, thermoelectricity, superconductivity and magnetism [33–36]. The electronic properties of half-Heusler compounds can be

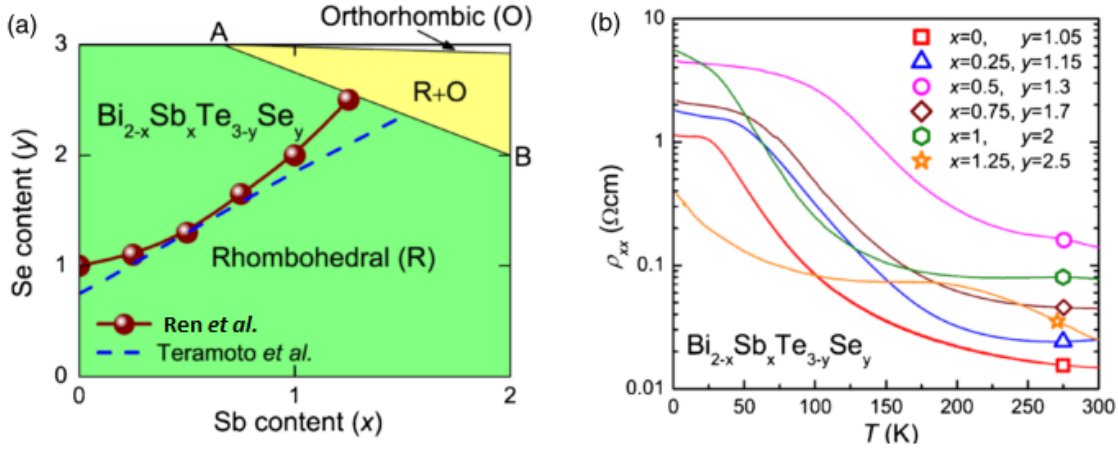

Figure 1.3: *(a) Composition phase diagram of the $Bi_{2-x}Sb_xTe_{3-y}Se_y$ (BSTS) system. The diagram was determined by fixing the Sb content x and optimizing the Se content y for x. The red points denote the compositions where the compensation between n- and p-type carriers is maximally achieved. The dashed line denotes the insulating composition previously suggested by Teramoto et al. [31]. (b) Temperature dependence of the resistivity ρ_{xx} for the series of BSTS samples at optimized ompositions. Figures taken from Ref. [29].*

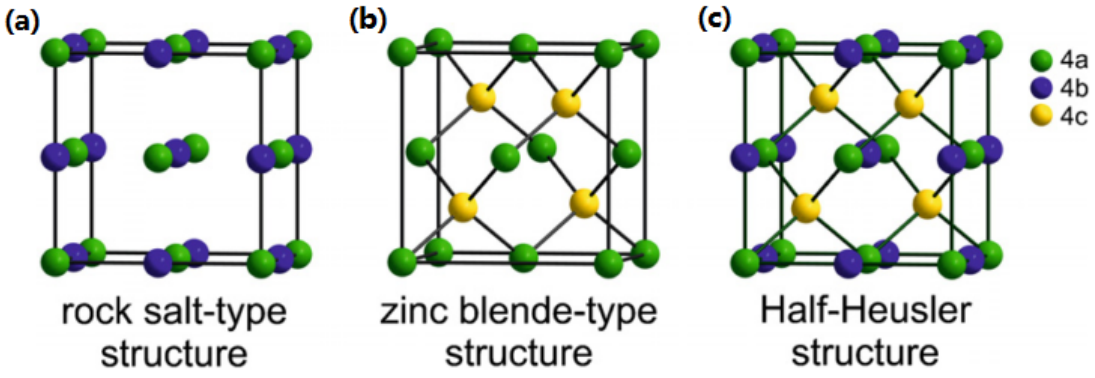

Figure 1.4: *(a) Rock salt-type structure. (b) Zinc blende-type structure. (c) Half-Heusler structure. The Wyckoff positions 4a, 4b, 4c are occupied by atoms Z (green), X (blue) and Y (yellow) respectively. Figures taken from Ref. [38].*

predicted by counting the number of valence electrons. For example, when the number of valence electrons is 18 for the closed shell, half-Heuslers are usually non-magnetic and semiconducting [37]. Furthermore, their band gaps can be tuned from 0 (e.g. LiMgN) to about 4 eV (e.g. ScPtBi) by choosing the XYZ chemical composition [37].

Because it was realized that the band structure of some half-Heusler compounds is analogous to that of CdTe or HgTe [34, 35], in which the topologically trivial or non-trivial case can be judged by the band order of the s-like Γ_6 state and the p-like Γ_8 state [8], many half-Heusler compounds were evaluated using first-principle band structure calculations in order to search for new topological materials. **Figure** 1.5 shows the energy difference between the Γ_6 and Γ_8 states, that is $E_{\Gamma_6} - E_{\Gamma_8}$, for many half-Heusler compounds as

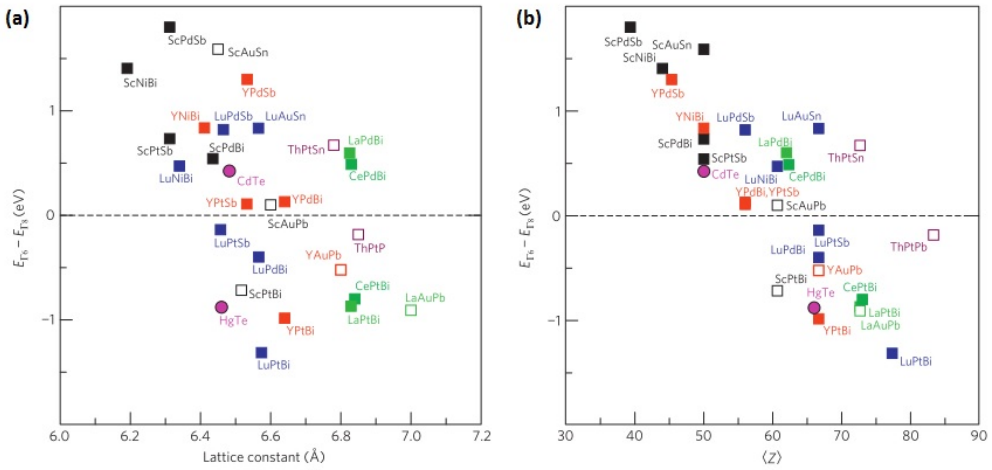

Figure 1.5: *The band inversion strength for several half-Heusler compounds defined by the energy difference $E_{\Gamma_6} - E_{\Gamma_8}$ as a function of (a) the lattice constant (b) the average nuclear charge $\langle Z \rangle$. When $E_{\Gamma_6} - E_{\Gamma_8} > 0$, there is no band inversion, indicating a trivial band structure, whereas when $E_{\Gamma_6} - E_{\Gamma_8} < 0$, band inversion is present, indicating a nontrivial band structure. Figures taken from Ref. [34].*

a function of the lattice constant and the average nuclear charge. When $E_{\Gamma_6} - E_{\Gamma_8} > 0$, like in ScPtSb, the material is a trivial insulator, whereas when $E_{\Gamma_6} - E_{\Gamma_8} < 0$, like in ScPtBi, the material is a TI candidate. The topological non-trivial nature was theoretically proven through two approaches: (i) no topological phase transitions occur when executing an adiabatic transformation between the half-Heuslers and a known $\mathbb{Z}_2$ topological insulator [35], and (ii) a topological phase transition takes place when driving the half-Heuslers to a known trivial system [34]. However, in practice, most of these half-Heusler compounds are semi-metals or zero-gap semiconductors in their native states. To realize intrinsic insulating behavior, a combination of crystal strain and uniaxial strain has been reported to open an energy gap [35, 39]. Recently, ARPES measurements on the half-Heusler compounds LuPtBi and YPtBi revealed the presence of topological surface states, with a Dirac point being found at a binding energy of ~ 0.5 eV, which indicated the topological nature of these systems [40]. Additional properties found in some potential half-Heusler TI compounds are: magnetism in LnPtBi (Ln = Nd, Sm, Gd, Tb, Dy) [41, 42] and LnPdBi (Ln = Er, Ho, Dy, Tb, Gd, Sm) [43–46], heavy fermion behavior in YbPtBi [47], and superconductivity in LnPtBi (Ln = Y, La, Lu) [48–53] and LnPdBi (Ln = Tm, Er, Ho, Dy, Sm, Lu, Y) [43–46, 54, 55]. We conclude that half-Heusler compounds offer a versatile platform for the realization of interesting topological phenomena.

Based on the Bogoliubov-de Gennes Hamiltonian for the quasiparticles of a superconductor, which is analogous to the Bloch hamiltonian of a band insulator, research on time-reversal-invariant topological insulators has been extended to time-reversal-invariant topological superconductors (TSCs) [56, 57]. A TSC has a full superconducting gap in the bulk and a gapless Andreev bound state on the edge or surface. The gapless state

is predicted to host a Majorana zero mode, which has potential applications in quantum computation [58]. As regards candidates for TSCs, a few promising compounds have attracted much attention: half-Heusler compounds as mentioned above, doped 3D topological insulators, such as $Cu_xBi_2Se_3$ [59, 60] and $Sr_xBi_2Se_3$ [61], and doped crystalline topological insulators, such as $In_xSn_{1-x}Te$ [62, 63]. The experimental confirmation of topological superconductiviy in these compounds is a prominent research topic in the field of TIs.

1.2 Overview

In this thesis, an extensive investigation of the transport properties of the 3D topological insulator $Bi_{2-x}Sb_xTe_{3-y}Se_y$ (BSTS) is presented. Besides, the magnetic and superconducting properties of ErPdBi, a member of the half-Heusler TI family, are presented. Finally, rotational symmetry breaking in the topological superconductor $Sr_xBi_2Se_3$ is reported, as probed by upper-critical field experiments. The thesis comprises seven chapters. After this introductory chapter, the remainder is organized as follows.

In Chapter 2, we start with the description of the preparation and characterization of the BSTS, ErPdBi and $Sr_xBi_2Se_3$ crystals used in the investigation in the next chapters. Then we present several cryogenic techniques that were employed for the transport and magnetic property studies. Specifically, we describe the physical property measurement system (PPMS Dynacool) and its measurement options, including the resistivity option, horizontal rotator option, VSM option and ACMS II option.

In Chapter 3, we present a general theoretical description of topological insulators involving the $\mathbb{Z}_2$ topological invariant, the existence of topologically protected edge or surface states and the intriguing properties of the nontrivial edge or surface states. In order to give a clear view of the bulk behavior of current topological insulator materials, the Mott and Ioffe-Regel criteria for the metal-to-insulator transition as well as band bending effects are described. Furthermore, we introduce two transport phenomena, the weak anti-localization effect and the Shubnikov de Haas effect, both of which are frequently employed to analyze the transport properties of topological insulators.

In Chapter 4, we systematically study the bulk-insulating properties of $Bi_{2-x}Sb_x$ $Te_{3-y}Se_y$ single crystals with compositions around $x = 0.5$ and $y = 1.3$ via resistance and Hall effect measurements. Next, we report resistance measurements on BSTS crystals with different thicknesses and analyze the resistivity behavior with a parallel resistor model. Chapter 4 is concluded with the magnetoconductance of an exfoliated BSTS nanoflake with a thickness of 130 nm and the analysis of its transport properties in the framework of the weak anti-localization effect.

In Chapter 5, we report a high-field magnetotransport study on selected low-carrier crystals of the topological insulator $Bi_{2-x}Sb_xTe_{3-y}Se_y$. Monochromatic Shubnikov - de

Haas oscillations (SdHOs) are observed at low temperatures. We present the temperature dependence and angular dependence of the SdHOs. Then we calculate important transport parameters of the surface states, including the carrier density, cyclotron mass and mobility, in the framework of the Lifshitz-Kosevich theory. In the end, we acquire the Berry phase by linearly extrapolating the Landau level plot and analyze the deviation of the Berry phase from the ideal value π in terms of the non-ideal linear dispersion relation of the Dirac cone of the Bi-based topological insulators and the Zeeman splitting in high magnetic field.

In Chapter 6, we present the discovery of superconductivity and magnetism in the non-centrosymmetric half-Heusler compound ErPdBi. First, we show the results of electrical transport, ac-susceptibility and dc-magnetization measurements that revealed superconductivity at $T_c = 1.22$ K. These data sets were used to extract the temperature dependence of the upper critical field. After that, we report the magnetic transition observed at $T_N = 1.06$ K. We present the magnetic and superconducting phase diagram and discuss the coexistence of superconductivity and magnetic order. Besides, we present the calculated electronic bulk band structure of ErPdBi that revealed its topological nature.

In Chapter 7, we report the discovery of rotational symmetry breaking in the topological superconductor $Sr_xBi_2Se_3$ probed by upper-critical field experiments. We present a detailed magnetotransport study of the angular variation of the upper critical field for a rotation of the applied field in the trigonal basal plane. Surprisingly, a pronounced two-fold anisotropy is observed, with B_{c2}^{a} almost a factor 3 larger than $B_{c2}^{a^*}$. This unusual anisotropy cannot be explained by the anisotropic effective mass Ginzburg-Landau model or the effect of flux flow induced by the Lorentz force. We propose two possibilities: unconventional superconductivity with an odd-parity polarized triplet Cooper pair state (Δ_4-pairing) recently proposed for rhombohedral topological superconductors, or a structural nature, such as self-organized stripe ordering of Sr atoms.

Chapter 2

Experimental techniques

In this chapter, first the preparation and characterization of the $Bi_{2-x}Sb_xTe_{3-y}Se_y$ (BSTS), ErPdBi and $Sr_xBi_2Se_3$ crystals used in this thesis project are described. Then, the cryogenic techniques used to investigate the transport and magnetic properties of these crystals are presented, with an emphasis on the newly installed instrument PPMS Dynacool. Finally, the resistivity option, horizontal rotator option, the VSM and ACMS II options of the PPMS Dynacool are presented.

2.1 Sample preparation

2.1.1 Bulk samples

The BSTS samples used in this thesis are all prepared at the Van der Waals-Zeeman Institute (WZI) by Dr. Y.K. Huang and Dr. D. Wu. The BSTS crystals were grown using the Bridgman method. The raw materials with a purity of at least 5N were weighed according to their nominal compositions and sealed in an evacuated quartz tube. The tube was placed vertically in the uniform temperature zone of a box furnace and heated up to 850 °C to melt the raw materials, and kept at this temperature for three days. Next the tube was cooled down to 520 °C at a rate of 3 °C/h and kept at this temperature for another three days to anneal the crystals that formed. In the final step, the tube was cooled down to room temperature at a rate of 10 °C/h. A small size of the growth boules was chosen to maximize the compositional homogeneity. The crystals were cleaved with Scotch tape to obtain flat and shiny surfaces at both sides and cut into a rectangular shape using a scalpel blade.

The ErPdBi single crystals were grown at the WZI by Dr. Y.K. Huang using a flux technique. The starting materials were Er, Pd and Bi with a purity of 3N5, 4N and 5N, respectively. First Er and Pd were arc-melted together in the ratio of 5 : 2, and Pd and Bi in the ratio of 3 : 5. Then both alloys were melted together to form ErPdBi. After that, the ErPdBi alloy was put in an alumina crucible with additional Bi which served as the flux. The ratio of ErPdBi : Bi was 1 : 5. The alumina crucible was placed in a quartz tube that was pumped to high vacuum and then filled with 0.3 bar high-purity argon gas and sealed. The tube was heated in an oven to 1150 °C and kept at this temperature for 36 h. Finally the tube was slowly cooled down to 500 °C at a rate of 3 °C/h in order to obtain the crystals. Samples were cut in a bar-shape by using a wire saw in a spark-erosion machine (AGIEPLUS).

The $Sr_xBi_2Se_3$ single crystals with $x = 0.10$ and $x = 0.15$ were grown at the WZI by Dr. Y.K. Huang by the Bridgman method. The raw materials Sr, Bi and Se with a purity of 3N5, 5N and 5N, respectively, were weighed and mixed together in the nominal ratio. The mixture was sealed in an evacuated quartz tube and heated up to 850 °C at a rate of 5 °C/h. Before cooling to 650 °C at the rate of 3 °C/h, the temperature was kept at 850 °C for around 3 h. In the end, the temperature was lowered to room temperature at a rate of 20 °C/min. Samples were cut along the crystal axes a and a^* after these were identified using Laue back-scattering diffraction (see **Section** 2.2).

2.1.2 Hall bar

BSTS Hall bars were fabricated at the University of Twente by Dr. M. Snelder. Smooth flakes were prepared through a mechanical exfoliation process from a bulk BSTS crystal,

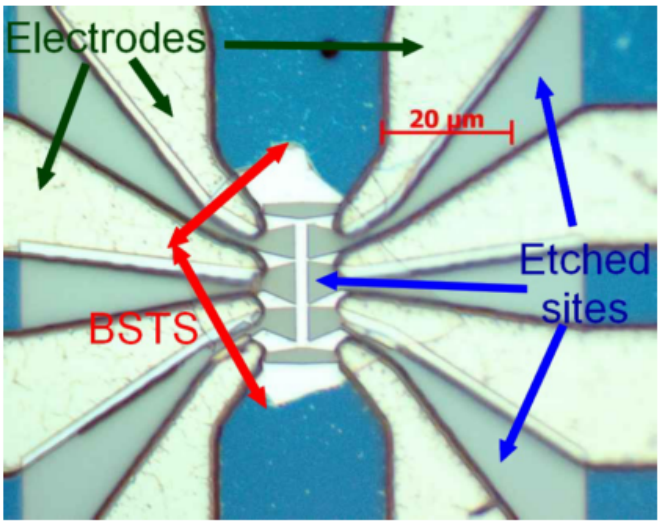

Figure 2.1: *Image of a Hall bar made from a $Bi_{1.46}Sb_{0.54}Te_{1.7}Se_{1.3}$ nanoflake. The sample, electrodes and etched sites are displayed. The white region in the middle is the $Bi_{1.46}Sb_{0.54}Te_{1.7}Se_{1.3}$ nanoflake. The blue background is the SiO_2 substrate, the light blue areas are the etched sites and grey regions are the electrodes. Figure taken from Ref. [64].*

and were deposited on a silicon-on-insulator substrate. First, standard photolithography and lift-off were used to define the Au electrodes on the flakes. Then, electron beam lithography was applied to shape the flake in a Hall bar structure. In both procedures, argon ion etching was employed and the sample was covered with either e-beam resist or photo-resist to avoid surface damage or contamination. The image of a typical BSTS Hall bar is shown in **Figure** 2.1.

2.2 Sample characterization

Sample characterization such as the crystal structure, composition and homogeneity is essential before any further investigation of the physical properties. **Figure** 2.2 shows the powder X-ray diffraction (XRD) pattern of $Bi_{1.5}Sb_{0.5}Te_{1.7}Se_{1.3}$, as well as the calculated pattern of Bi_2Se_3 for comparison. Both patterns are essentially the same and all the peaks are in good agreement with the rhombohedral crystal structure with space group $R\bar{3}m$. The shift of the diffraction peaks to lower 2θ values of $Bi_{1.5}Sb_{0.5}Te_{1.7}Se_{1.3}$ compared to Bi_2Se_3 is attributed to an increase of the lattice parameters. To check the homogeneity of the crystals, the electron probe micro analysis (EPMA) technique was used. **Figure** 2.3(a) shows the Sb content at 5 different positions on a $Bi_{1.46}Sb_{0.54}Te_{1.7}Se_{1.3}$ crystal. The intensities of the 5 peaks are almost the same, showing no sign of significant stoichiometric variation of the Sb content and thus this attests to a homogenous sample. In addition, the Sb content of 6 BSTS samples with nominal Sb content varying from 0.42 to 0.58 was traced using EPMA, as shown in **Figure** 2.3(b). The peak intensity systematically increases with increase of the nominal Sb content, indicating that the nominal weigh-in

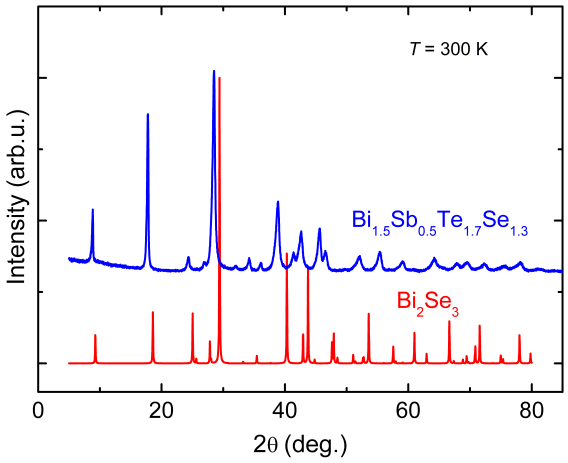

Figure 2.2: *Powder X-ray diffraction pattern of $Bi_{1.5}Sb_{0.5}Te_{1.7}Se_{1.3}$ at room temperature and the calculated pattern for Bi_2Se_3.*

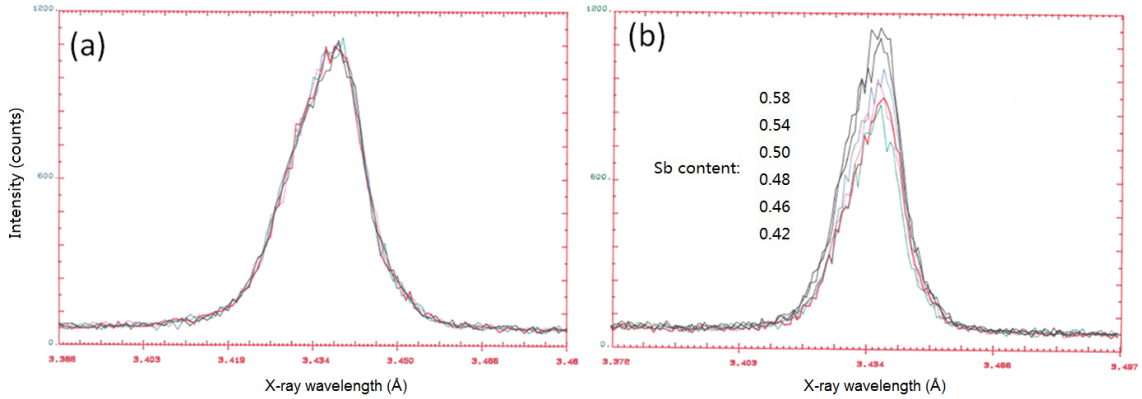

Figure 2.3: *Electron Probe Micro Analysis: (a) spectrum of Sb content at 5 different positions on a $Bi_{1.46}Sb_{0.54}Te_{1.7}Se_{1.3}$ sample; (b) spectrum of Sb content of 6 BSTS samples with nominal Sb content varying from 0.42 to 0.58 (the lowest curve to the highest curve).*

stoichiometry is well transferred to the final crystals.

The crystallographic structure of as-grown ErPdBi was verified and the sample purity was determined by the powder XRD technique. The powder XRD pattern shown in **Figure** 2.4(a) is taken on a powder obtained by grinding the as-grown ErPdBi crystal. The experimental data (red line) are in good agreement with a simulation (blue line) for the Half Heusler $F\bar{4}3m$ space group with lattice parameter a = 6.5953 Å. Four tiny extra peaks can be assigned to Bi inclusions with the total volume amount of less than 4%. The phase homogeneity and the stoichiometry of the crystals were further investigated via EPMA and scanning electron microscopy (SEM). EPMA revealed the main phase has the composition ErPdBi. A SEM picture shown in **Figure** 2.4(b) displayed well defined sample regions with a main phase (dark grey) and Bi flux precipitates (light grey). Crystals for transport and magnetic measurements were cut-out in selected regions to avoid Bi inclusions. Moreover, the single-crystalline nature was checked by means of back-scattering Laue diffraction,

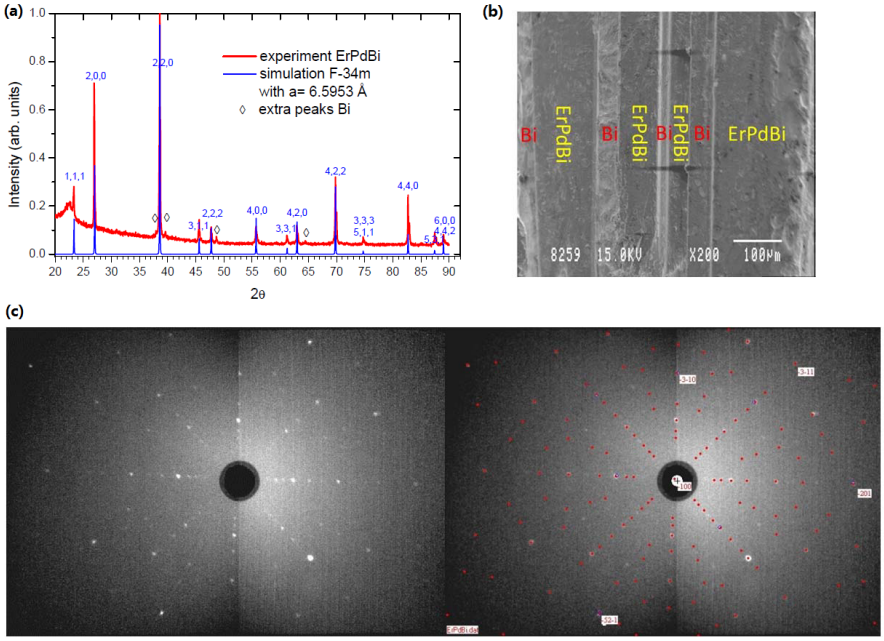

Figure 2.4: *(a) Powder X-ray diffraction pattern of the ErPdBi crystal. (b) Scanning electron microscope picture of the surface of the ErPdBi crystal. (c) Back-scattering Laue diagram of ErPdBi. Left picture: measured. Right picture: simulated pattern(red dots) superposed on the measured pattern.*

which shows well defined spots in the Laue diffraction diagram, see **Figure** 2.4(c).

The crystallographic structure of as-grown $Sr_xBi_2Se_3$ was verified and the sample purity was determined using powder XRD. **Figure** 2.5(a) shows the powder XRD patterns for $Sr_{0.10}Bi_2Se_3$ (blue line) and $Sr_{0.15}Bi_2Se_3$ (red line), both recorded at room temperature. The patterns are in excellent agreement with the calculated pattern for Bi_2Se_3 and the space group $R\bar{3}m$. The lattice parameters ($a = 4.137$ Å and $c = 28.65$ Å) are identical for both compositions within the experimental resolution. The tiny extra peaks (black arrows) in the diffraction pattern of $Sr_{0.15}Bi_2Se_3$ point to the presence of a minority impurity phase. In order to investigate whether $Sr_{0.15}Bi_2Se_3$ undergoes a structural transition the powder X-ray diffraction pattern was measured by Dr. Y. Matsushita at the National Institute for Materials Science in Japan down to $T = 10$ K. No change in crystal structure was observed (see **Figure** 2.5(b)). The lattice parameters a and c both show a small decrease with decreasing temperature. The tiny extra peaks (black arrows) in the diffraction pattern point to the presence of a minority impurity phase. To confirm their single-crystalline nature and identify the crystal axes a and a^*, Laue back-scattering diffraction was carried out on the $Sr_xBi_2Se_3$ crystals (see **Figure** 2.6). The Laue diagrams show well defined spots and confirm the trigonal symmetry in the basal plane.

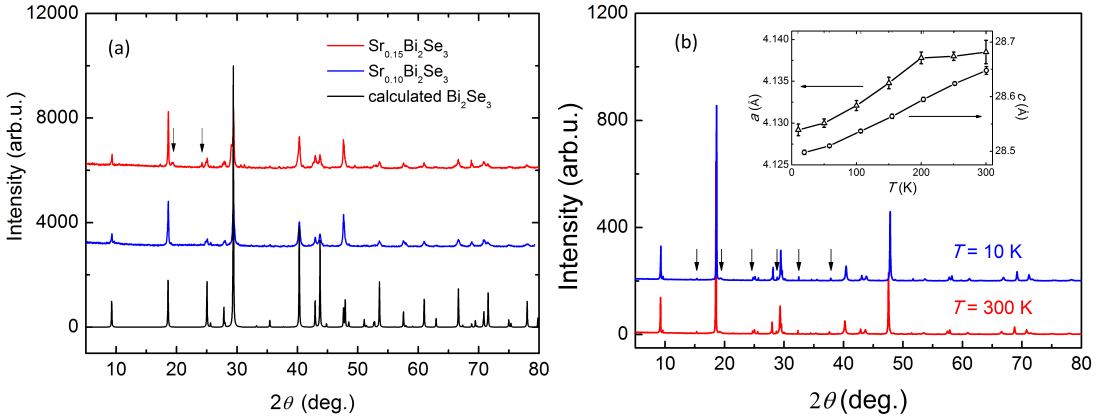

Figure 2.5: *(a) Powder X-ray diffraction pattern of $Sr_{0.10}Bi_2Se_3$ (blue line) and $Sr_{0.15}Bi_2Se_3$ (red line) at room temperature. The black line is the calculated pattern for Bi_2Se_3. (b) Powder X-ray diffraction pattern of $Sr_{0.15}Bi_2Se_3$ at 300 K (red line) and at 10 K (blue line). The inset shows the temperature variation of the lattice parameters a and c.*

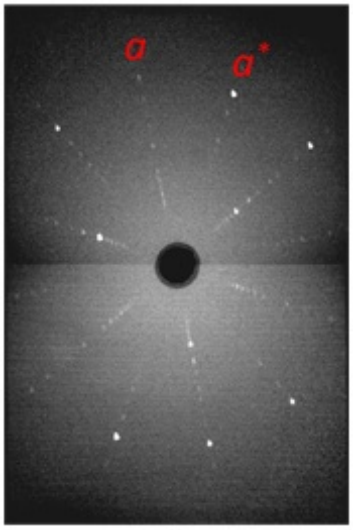

Figure 2.6: *Laue back-scattering pattern of $Sr_{0.15}Bi_2Se_3$ with the incoming beam along the c-axis. The diffraction pattern has trigonal symmetry. The a and a^* axis are indicated.*

2.3 Cryogenic techniques

In order to study the low temperature properties of the samples, several experimental facilities at the WZI, including a home-made ^{4}He bath cryostat, a MagLab Exa (Oxford Instruments), a HelioxVL ^{3}He refrigerator (Oxford Instruments) and a Physical Property Measurement System (PPMS) Dynacool (Quantum Design) were used. In addition, low-temperature high-field measurements were carried out at the High Field Magnet Lab (HFML) in Nijmegen using a ^{4}He bath cryostat. Since the PPMS Dynacool was newly installed at the WZI in the summer of 2013, an overview of the system and its measurement options is presented here. The other experimental set-ups will be presented very briefly since detailed information can be found in Refs. [65–67].

The home-made ^{4}He bath cryostat in the WZI enables transport measurement in the temperature range from 300 K to 4.2 K using liquid ^{4}He as a cryogen.

The MagLab Exa is equipped with a Variable Temperature Insert (VTI) for measurements in the temperature range 2-360 K. It is fitted with a 9 T superconducting magnet.

The HelioxVL ^{3}He refrigerator is operated in a liquid ^{4}He cryostat equipped with a 14 T superconducting magnet. The operation temperature runs from base temperature 0.25 K up to 300 K in zero field and from 0.25 K up to 100 K in field. To reach the base temperature, ^{3}He gas is first condensed into ^{3}He pot with help of a pumped ^{4}He stage, that is a 1 K pot with the temperature around 1.5 K. Then the vapour pressure of the ^{3}He liquid is lowered using the built-in cryogenic adsorption pump. In this way, a base temperature of 0.25 K can be reached.

The PPMS Dynacool allows for measurement temperatures in the range from 1.9 K to 400 K without the need to supply liquid cryogens. Instead a two-stage pulse tube cryocooler, as well as a gas flow regulation system is used. A schematic diagram of the cryostat is displayed in **Figure** 2.7 [68]. The two-stage pulse tube cryocooler is located in a cryogenic bucket (green outline) filled with helium gas. The first stage of the cryocooler typically runs at around 45 K and cools the main radiation shield (black dashed line) by conduction through a small gas gap. The other first stage components, including the annulus radiation shield, the first stage of the cryopump, the electrical wiring heat loads and the mechanical support heat loads coming from room temperature, are cooled by solid contact to the main radiation shield. The second stage of the cryocooler typically runs at around 4.2 K with the 4 K plate cooled by contact with around 150 cc of liquid helium in the bottom of the bucket. The other second stage components, including the superconducting magnet, the second stage of the cryopump, the helium gas and liquid for sample chamber cooling, the electrical wiring heat loads and the mechanical support heat loads coming from the first stage temperature, are cooled by solid contact to the 4 K plate. The sample chamber (grey) sits inside the annulus tube and is cooled by helium flow. The helium flow is driven by the pressure difference between the cooling annulus and the bucket (maintained at a pressure of around 1 atmosphere by controlling the 4 K plate at 4.2 K). The circulation pump maintains the pressure of the cooling annulus at moderate vacuum and causes helium from the bucket to flow up the cooling annulus to cool the sample chamber. The exhausted helium from the circulation pump is returned to the bucket and cooled by the cryocooler for reuse. Materials with a low thermal conductivity are employed between cryostat components to maintain temperature differences and to avoid heat leaks.

There are two cooling flow modes, the main flow and low temperature flow modes, for temperature ranges 300–10 K and 10–1.9 K, respectively. In the main flow, the 4.2 K helium gas taken from the bucket flows up the counter-flow heat exchanger (CFE), goes through the mass flow controller and back down the CFE. Then, it travels through the

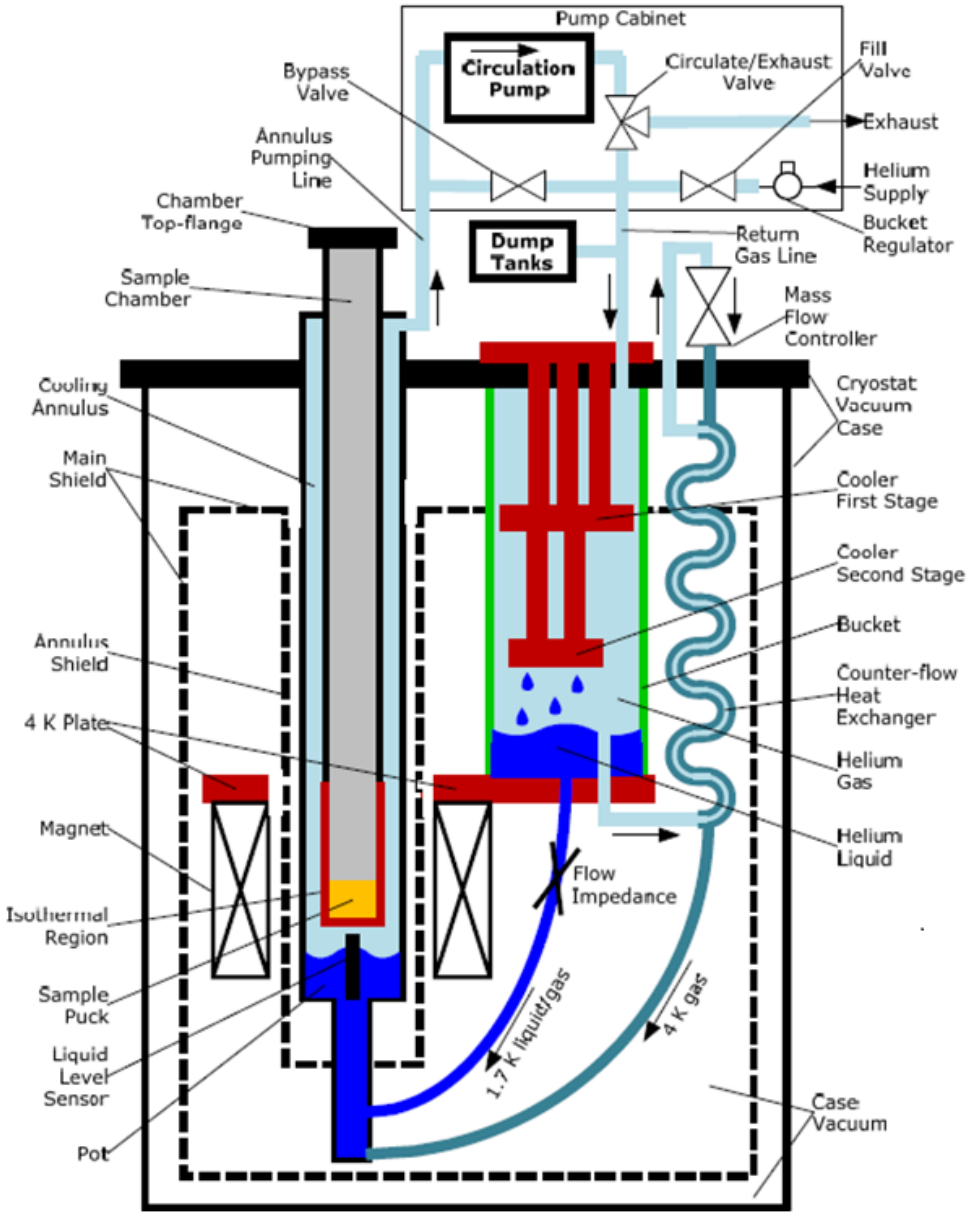

Figure 2.7: *A schematic diagram of the Dynacool cryostat. The two stage pulse tube cryocooler sits in the bucket (in green) filled with helium gas. The first stage cooler running at around 45 K has solid contact to the main shield (black dashed line), through which the other first stage components are cooled. The liquid helium in the bottom of the bucket cools the 4 K plate, through which the other second stage components such as the superconducting magnet are cooled. The sample chamber (in grey) is embedded in the annulus and the sample puck (in yellow) is located in the isothermal region at the bottom of the sample chamber. Two lines connected to the bottom of the sample chamber represent the two cooling flow modes – main flow (in dark cyan) and low temperature flow modes (in blue)– of the sample chamber. Helium gas and helium liquid are shown in light cyan and blue respectively and the direction of the helium flow is indicated by arrows. Figure taken from Ref. [68].*

connecting tube and into the cooling annulus. The temperature is controlled by adjusting the main flow rate and the annulus pressure through the mass flow controller. In the low temperature flow, the 4.2 K liquid helium flows through the capillary flow impedance, where the helium undergoes expansion because of the pressure difference between the bucket (1 atmosphere) and the annulus ($\sim$13 mbar). At the same time, some of it evaporates resulting in a mixture of liquid and gas at about 1.7 K. This mixture goes through the connecting tubes to the bottom of the cooling annulus. To provide a thermally uniform region for the sample and experiment, high-conductivity copper is used at the sample tube (in red) to minimize thermal gradients. For experiments, a robust 12-pin sample holder, normally called sample puck (in yellow), is employed. It is placed at the bottom of the isothermal region and is tightly connected to the block thermometer outside the sample chamber that is used to record the temperature. The sample puck can be cooled down from 300 to 1.9 K in 40 minutes and the temperature stability is $\pm$ 0.02% for T > 20 K and $\pm$ 0.1% for T < 20 K.

The PPMS Dynacool allows for measurements in magnetic fields ranging from 9 to -9 T with a 9 T switch-less superconducting solenoid magnet. The superconducting solenoid resides in the cryostat vacuum space and is cooled by direct thermal contact to the 4 K plate. The superconducting solenoid magnet is directly connected to the magnet controller via the magnet leads. The magnet controller provides a maximum current of 60 A and a typical current of 55 A is needed for a maximum field of 9 T. The magnetic field is produced in a vertical direction (downwards) with a homogeneity of $\pm$ 0.01% in a range of 3 cm at axis and centered at 4.05 cm above the sample puck. The resolution of the magnetic field is 0.016 mT and the maximum sweep rate is 22 mT/s. There is a built-in magnetic shield made up of steel. The stray field at a distance of 30 cm outside of the cryostat cabinet is smaller than 0.5 mT.

At the High Field Magnet Laboratory at the Radboud University in Nijmegen, a Bitter magnet with a maximum magnetic field of 33 T was employed to produce high magnetic fields. The direction of the magnetic field is in the direction from top to bottom with the homogeneity of 0.1% (10^{-3} in 1 cm diameter of spherical volume). The diameter of the bore is 32 mm at room temperature. A bath cryostat is used to cool the sample insert from 300 to 1.7 K. Circulated cooling water is employed to prevent the magnet from overheating during the experiments.

2.4 Measurement options of the PPMS Dynacool

2.4.1 Resistivity measurements

The resistivity measurements were conducted using a four-point configuration, which eliminates the contribution of the leads and the voltage contacts allowing for an accurate

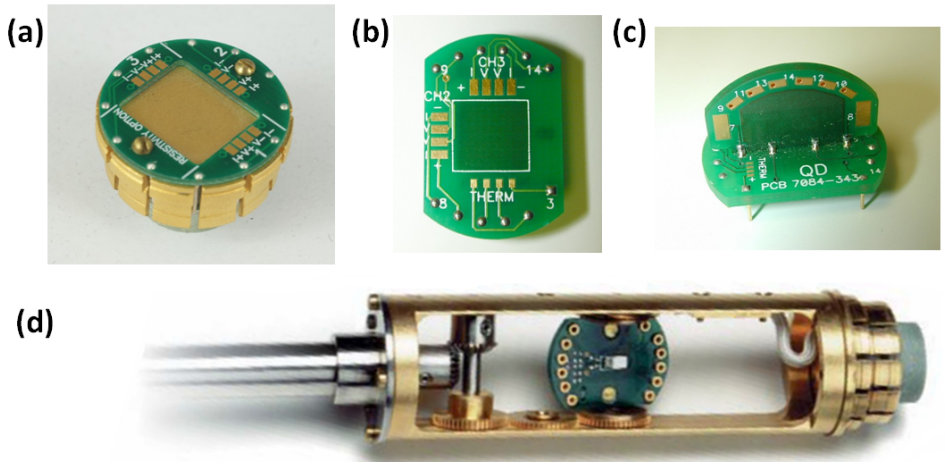

Figure 2.8: *PPMS sample pucks for (a) resistivity option and (b)(c) horizontal rotator option for out-of-plane and in-plane sample rotation. (d) Horizontal rotator transfer case with rotator platform circuit board. Figures taken from Ref. [69].*

determination of low resistance values. In this configuration, two outer leads are used to pass the current I through the sample and two inner leads are employed to measure the potential drop V over the sample. The resistance R is calculated according to Ohm's law $R = V/I$ and the resistivity ρ is calculated via the relation $\rho = R\frac{A}{L}$, where A is the cross section of the sample and L is the distance between the two voltage contacts.

In the PPMS Dynacool the resistivity option with a configurable resistance bridge board is installed to perform resistivity measurements. Four channels are available on the resistance bridge board and up to three samples can be mounted on the resistivity sample puck (see **Figure** 2.8) to make the resistivity measurements. The measurements do not take place simultaneously, but begin from the lowest channel when more than one channel is activated. Once a channel is active, the current is running through the sample regardless of whether a measurement is performed or not. The excitation current, voltage and power can be set in the range of $\pm$ 0.01–5000 μA, 1–95 mV and 0.001–1000 μW, respectively. The measurement errors are within 1% when the measured resistance R < 4 MΩ, and increase considerably when R > 4 MΩ. The AC drive mode for the excitation current in the form of a square-wave is made on the resistance bridge board and is synchronized to the line frequency of 50 Hz with the measurement rate of 8.33 Hz. In the resistivity option, the sample temperature and the control temperature are both obtained from the value of the block thermometer. The noise in the sample temperature is around ± 0.01 K. To install and remove the sample puck, a special tool named the puck insertion tool is used. Detailed instructions are given in the PPMS Dynacool User's Manual [68].

The resistivity option can be combined with the so-called horizontal rotator option. This allows for the rotation of the sample platform with respect to the magnetic field. **Figure** 2.8 (b)(c)(d) show the sample pucks for out-of-plane and in-plane sample rotation, and the transfer case with rotator platform circuit board of the horizontal rotator option,

respectively. In this instrument, the horizontal rotator with serial number HRE527 can be installed. The rotation is in the range from -10° to 370°, where 0° and 360° denote the face-up orientation. The rotator can be operated manually or automatically with a rotator motor. It is of great importance that the position reported in the software matches the actual orientation of the sample in the measurements. Therefore, proper position calibration is necessary before the real measurement starts. This calibration procedure is presented in the PPMS horizontal rotator option user's manual. Another issue that should be kept in mind about the position is the backlash of the rotator. This is caused by the effect of the temperature dependence of the mesh on the rotator gears and the torsional spring which allows for alternate sticking and slipping behaviour while it is being unwound. The backlashes at 300 K, 150 K and 10 K are roughly around 2°, 8°, 6°, respectively. To reduce backlash and conduct good measurements, the rotation should always proceed in the same direction, that is, in the direction of decreasing angles. For temperature control, the rotator is equipped with a custom thermometer that serves to measure the sample temperature and the control temperature. Two other aspects that should be considered are: (i) the speed of the temperature control is slower resulting from the thermal load of the horizontal rotator, and the noise of the sample temperature is around ± 0.1 K with an oscillation-like form; (ii) channel 1 of the sample puck is used for the custom thermometer and channel 2 and 3 can be used to mount samples, however, the signal of channel 2 and 3 on the sample puck are transferred to channel 1 and 2 of the user bridge board during measurements. Given the delicate parts of the horizontal rotator, a rotator support tool is provided to help avoid denting and bending the rotator insert and a sample removal tool is used to avoid damaging gears and wiring.

2.4.2 DC magnetization and AC susceptibility measurements

DC magnetization measurements were performed with the Vibrating Sample Magnetometer (VSM) option of the PPMS Dynacool. The basic principle of operation is as follows: first, magnetize the sample by placing it in a uniform magnetic field, and then move the sample sinusoidally by means of the VSM linear motor in and out of a pickup coil, which will induce a voltage. The induced voltage is proportional to the DC magnetic moment of the sample and is measured with help of a lock-in amplifier using the position signal from the VSM linear motor as a reference signal.

Figure 2.9 shows the typical sample holders for the VSM measurements. The quartz paddle with a diameter of 4 mm (**Figure** 2.9(a)) is designed for the lowest magnetic moment samples. A brass trough-shaped sample holder that fits samples up to a diameter of 4 mm (**Figure** 2.9(b)(c)) provides versatility. Considering the high accelerations during VSM measurements, the sample should be firmly mounted on the sample holder. There are normally two methods to secure the sample to the holder: (i) with help of glue, such as GE

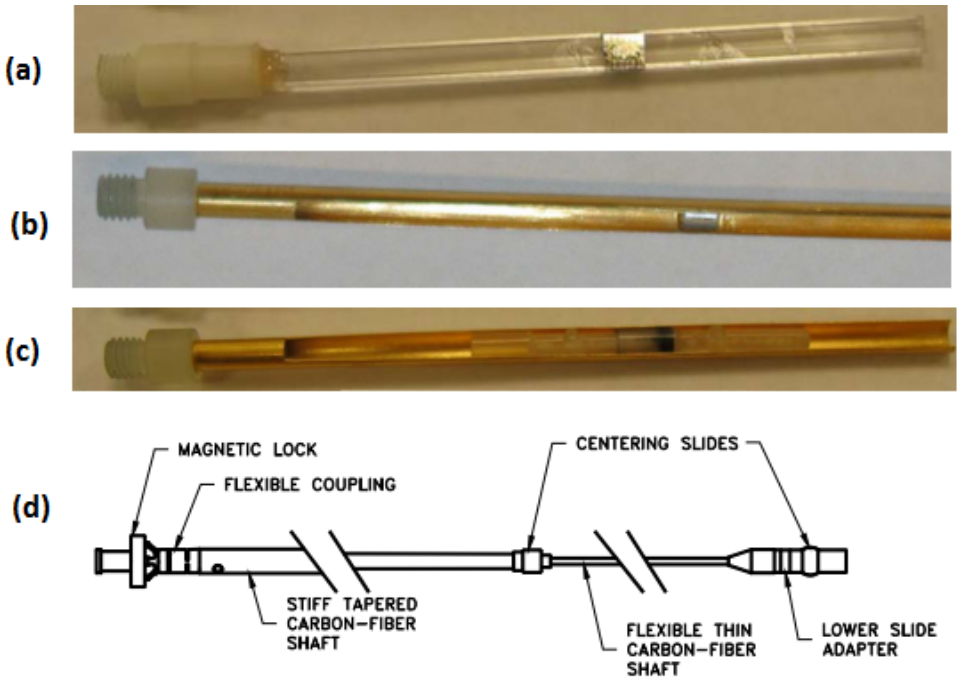

Figure 2.9: *VSM sample holders with samples mounted: (a) quartz paddle and (b)(c) brass trough for solid and powder samples. (d) VSM sample rod made from carbon fiber. Figures taken from Ref. [70].*

varnish used at low temperature, Duco cement used at room temperature with materials of similar thermal properties, and Superglue used at room temperature with a fast drying speed, (ii) with the help of tape, such as kapton tape and thin teflon tape. As regards powder samples, an injection molded plastic container (shown in **Figure** 2.9(c)) serves as the holder to keep the powder in place. Since the sample position is important for the VSM measurements, a sample-mounting station is provided to precisely locate the sample on the sample holder.

The VSM linear motor makes the sample vibrate at a rate of 40 Hz with the peak-to-peak amplitude of 1-4 mm. To hold the sample rod which is used to suspend the sample holder (see **Figure** 2.9(d)) in place, a magnetic-locking mechanism is applied by using small magnets at the top of the sample rod. It is worth noting that the sample will be exposed to vertical magnetic fields of up to approximately 200 Gauss when passing through the top of VSM linear motor transport. The pickup coilset (shown in **Figure** 2.10(a)) has the serial number 495, which is used to identify the coil calibration information. The center of the coil is 40.1 mm above the puck surface, which is in the high homogeneity field region of the external magnet. The bore diameter is 6.33 mm, which is the sample width limitation. A thermometer for monitoring the sample temperature is mounted near the pickup coils. The measurement temperature, sample temperature and control temperature are all given by the value of the coil thermometer. The detection system has a sensitivity of 10^{-9} Am^2 at a data rate of 1 Hz and is not significantly affected by large magnetic

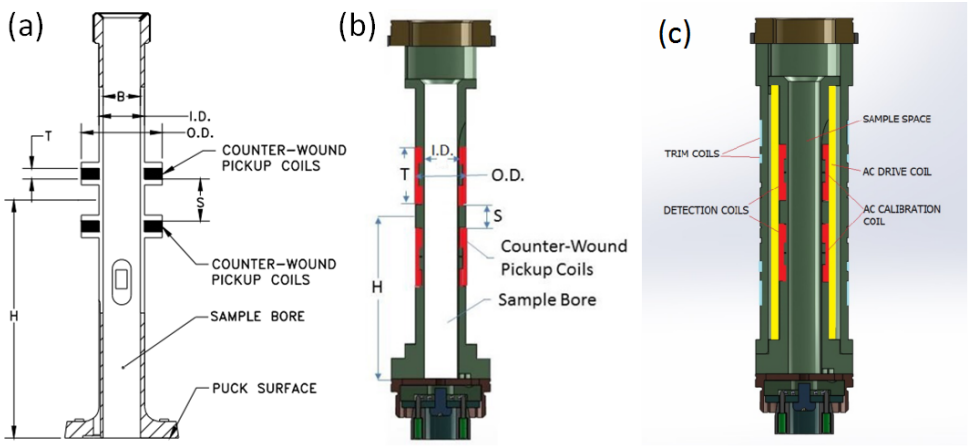

Figure 2.10: *(a) Schematic diagram of the VSM standard coil set puck, Bore diameter (B) = 6.33 mm; coil thickness (T) = 1.78 mm; coil spacing (S) = 7.11 mm; coil inner diameter (I.D.) = 7.73 mm; coil outer diameter (O.D.) = 13.7 mm; height above puck surface (H) = 40.1 mm. (b)(c) schematic diagrams of the ACMS II standard coil set puck, I.D. = 8.1 mm; T = 14.0 mm; S = 5.9 mm; O.D. = 12.4 mm; H = 40.1 mm. Figure taken from Ref. [70, 71].*

fields. To obtain VSM measurement results of high quality, the sample size and shape as well as sample position should be taken into account. The sample diameter should be less than 4 mm to avoid rubbing against the coil set and the sample length should be less than 5 mm to maintain the accuracy of the point source dipole approximation in evaluating the magnetic moment. It is recommended to mount the sample on the sample holder 35 mm above the bottom of the sample holder considering the height of the coilset of 40.1 mm and a maximum VSM vibration amplitude of 4 mm. Periodic touchdown operations, which adjust for changes in the sample position, should be performed to keep the center position stable within about 0.1 mm for accurate VSM measurements. Particularly, when sweeping the temperature from 300 K to 2 K, there is no significant change in the length of the sample rod because of the very low thermal expansion coefficient of the carbon fiber, while the stainless steel of the sample chamber will contract in length by ~ 2 mm. Even when the temperature is stabilized, the sample position is still moving within 4 hours. Therefore, it is recommended to make a touch down operation every 10 K when sweeping temperature and touch down every 10 minutes when at stable temperature.

AC susceptibility measurements were conducted via the AC Measurement System (ACMS II) option of PPMS Dynacool. The basic principle of operation is as follows: first, an AC drive magnetic field is generated by a small AC current in the drive coil, which will result in a time-changing magnetization in the sample; then the time-dependent magnetization will lead to a change in flux, which will induce a voltage in the pickup coils. The induced voltage is proportional to the magnetization and is detected with lock-in amplifiers.

In fact, the ACMS II option can also be used to measure DC magnetization. The

ACMS II option is similar to the VSM option. The main difference is the coilset puck and accuracy. ACMS II option has a sensitivity of $\sim 10^{-11}$ Am^2 and is two orders higher than that of VSM option. The serial number of the coilset puck of the ACMS II option is wf026 and schematic diagrams of the coilset are shown in **Figure** 2.10(b)(c). The sample bore diameter is 8.1 mm and the sample diameter limitation is extended to 6 mm. The height of the pickup coil is 14 mm and the sample length should be less than 6 mm. Since the center for the bottom pickup coil is 25 mm above the puck surface, the sample should be mounted on the sample holder near 25 mm above the bottom of the sample holder. The frequency of the AC drive current of the AC drive coil ranges from 10 Hz to 10 KHz. The maximum drive field that can be generated is 17 Oe. However, considering the Joule heating caused by the eddy currents in the copper portion of the sample chamber because of the AC drive field, the applied AC drive field should be limited at temperatures below 25 K to avoid warming.

Chapter 3

Theoretical aspects

In this chapter the theoretical background of my PhD research is presented. First, a general description of topological insulators is given starting from symmetry arguments ($\mathbb{Z}_2$ topological invariant) towards band inversion and electronic structure calculations. Then, as regards to transport measurements, the simple criteria given by Mott and Ioffe-Regel are provided to judge the intrinsic insulating behavior of TIs. Also band bending effects which affect the transport properties are presented. Next, the focus is turned to two transport phenomena: the weak anti-localization effect and Shubnikov de Haas effect. Finally, a short introduction to time-reversal invariant topological superconductivity is presented.

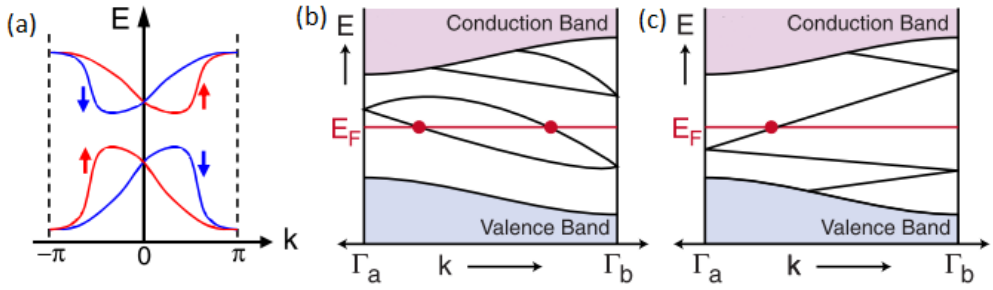

Figure 3.1: *(a) The energy bands of a system with time reversal symmetry come in pairs, with the state +**k** and the state -**k** having the same energy. When the spin-orbit coupling lifts the degeneracy of the bands, the degeneracy remains at the time reversal invariant points where +**k** becomes equivalent to -**k** due to the periodicity of the Brillouin Zone. There are two time reversal invariant points, $k = 0$ and $k = \pi$. At the right: schematic picture of half of the Brillouin zone displaying the edge states between two time reversal invariant points,Γ_a and Γ_b, for (b) topologically trivial and (c) topologically nontrivial cases. Figures were taken from Ref. [1, 72].*

3.1 Topological insulators

Topological insulators preserve time reversal symmetry (TRS). For particles with spin 1/2 under TRS, a constraint known as Kramers' theorem (that is, all eigenstates of a Hamiltonian with TRS are at least twofold degenerate) will take effect, because the time reversal operator Θ which is given by $\Theta = \exp(i\pi S_y)K$ has the important property $\Theta^2 = -1$. Here S_y is the spin operator and K is complex conjugation. This can be proved by applying Θ on a non-degenerate state $\mid \psi >$. Then we have $\Theta \mid \psi >= c \mid \psi >$ with a constant c. Applying Θ on both sides of the equation we obtain $\Theta^2 \mid \psi >= \mid c \mid^2 \mid \psi >$. This contradicts $\Theta^2 = -1$, because $\mid c \mid^2 \neq -1$. When there is no spin-orbit coupling (SOC), there is degeneracy between spin up and spin down. When the SOC is present, the degeneracy will be lifted except for the time reversal invariant points where +**k** becomes equivalent to -**k** due to the periodicity of the Brillouin Zone (BZ). This is because when the Hamiltonian preserves TRS, $H(\mathbf{k})$ satisfies $H(-\mathbf{k}) = \Theta H(\mathbf{k})\Theta^{-1}$, which means the state +**k** and the state -**k** are at the same energy (see **Figure** 3.1(a)).

Topological insulators can be distinguished from conventional insulators by the $\mathbb{Z}_2$ topology, characterized by the $\mathbb{Z}_2$ topological invariant ν. In 2D systems a single $\mathbb{Z}_2$ topological invariant is enough to characterize the time reversal invariant band structure. In 3D systems four $\mathbb{Z}_2$ topological invariants are needed. Several approaches are used to evaluate the $\mathbb{Z}_2$ topological invariants. One of them, proposed by Fu and Kane [14], is commonly used because of its simplicity when a material system possesses inversion symmetry, which is the case for BSTS. The $\mathbb{Z}_2$ topological invariant ν can be determined by the following formulas:

$$(-1)^{\nu} = \prod_i \delta_i \tag{3.1}$$

$$\delta_i = \prod_{m=1}^{N} \xi_{2m}(\Gamma_i) \tag{3.2}$$

where $\xi_{2m}(\Gamma_i) = \pm 1$ and represents the parity eigenvalue of the $2m$th occupied energy band at the ith time reversal invariant **k**-point, Γ_i. The product in **Equation** 3.1 runs over all four and eight time reversal invariant **k**-points for 2D and 3D systems, respectively. The product in **Equation** 3.2 runs over all $2N$ occupied energy bands for every time reversal invariant **k**-point. This approach has been carried out successfully by Zhang *et al.* [16] to predict that the layered, stoichiometric crystals Sb_2Te_3, Bi_2Te_3 and Bi_2Se_3 are topological insulators, while Sb_2Se_3 is not. **Figure** 3.2 (a) shows the parity eigenvalues of the highest fourteen occupied bands and the lowest unoccupied band at the time reversal invariant point Γ for these four crystals. When comparing the parities of the occupied bands of the trivial material Sb_2Se_3 to those of the nontrivial ones, there is an exchange of the parity between the highest occupied band and the lowest unoccupied band for the nontrivial materials. This is due to strong spin orbit coupling which leads to so-called band inversion. Let us take Bi_2Se_3 as an example. **Figure** 3.2 (b) shows the energy diagram near the Fermi energy of Bi_2Se_3, transformed from the atomic energy levels of Bi ($6s^26p^3$) and Se ($4s^24p^4$). Only the p orbitals are considered since the closed s shell is not near the Fermi energy. Three effects should be taken into account. First, the chemical bonding between Bi and Se hybridizes the energy states and pushes up the Bi states, while pushing down the Se states. Then, the crystal field decreases the degeneracy of the Bi and Se states $|P_{x,y,z}>$. The $|P_{x,y,z}>$ states are split into $|P_{x,y}>$ and $|P_z>$ states, where the $|P_z>$ states end up being close to the Fermi energy. Finally, the effect of SOC leads to repulsion between the $|P_z, \uparrow (\downarrow)>$ and $|P_{x+iy} \uparrow (\downarrow)>$, $|P_{x-iy} \uparrow (\downarrow)>$ states. As a result, the $|P1_z, \uparrow (\downarrow)>$ state originating from Bi is pushed down and the $|P2_z, \uparrow (\downarrow)>$ originating from Se is pushed up. When the SOC is strong enough, the two states $|P1_z, \uparrow (\downarrow)>$ and $|P2_z, \uparrow (\downarrow)>$, closest to Fermi energy, become inverted. As these two states have opposite parity, the parity of the occupied valence bands is altered as a whole, which leads to the transformation from a trivial insulator to a topologically nontrivial insulator.

The physical consequence of a nontrivial $\mathbb{Z}_2$ topological invariant (ν = 1) is the appearance of topologically protected edge or surface states. The topological invariant ν determines whether an even number (ν = 0) or odd number (ν = 1) of surface bands intersect the Fermi level inside the bulk gap [14]. **Figure** 3.1(b) and 3.1(c) schematically show the topologically trivial and nontrivial cases. In the figure, half of the BZ is shown with two time reversal invariant **k**-points labeled Γ_a and Γ_b. The bulk conduction and valance bands are displayed as shaded regions and are separated by an energy gap. There are two possible ways to connect the edge or surface states at the time reversal invariant points (see **Figure** 3.1 (b) and (c)). In **Figure** 3.1 (b) the Fermi level intersects the bands an even number of times. In this case, it is possible that the edge states are pulled out of the gap by varying the surface Hamiltonian. In contrast, in **Figure** 3.1 (c) there is an odd

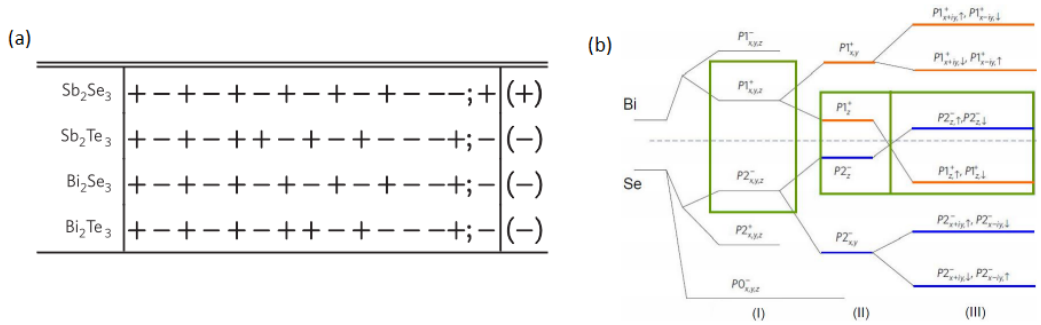

Figure 3.2: *(a) The parity eigenvalues of the highest fourteen occupied bands and the lowest unoccupied band at the time reversal invariant point* Γ *for* Sb_2Se_3*,* Sb_2Te_3*,* Bi_2Te_3 *and* Bi_2Se_3 *crystals. The product of the parity eigenvalue for the fourteen occupied bands is displayed in brackets. (b) Energy diagram displaying the atomic* p *orbital of Bi and Se transforming to conduction and valence bands of* Bi_2Se_3 *at the* Γ *point under the effects of chemical bonding (I), crystal field (II) and spin orbit coupling (III). The spin orbit coupling leads to band inversion near the Fermi energy (dashed line). Figures taken from Ref. [16].*

number of bands that intersects the Fermi level. In this case, no matter how the surface Hamiltonian varies, the edge state is guaranteed to cross any Fermi level inside the bulk gap.

The spin of the topologically protected edge or surface states are locked to their momentum and this makes them robust to disorder and immune to backscattering. Take the edge states of the QSH system as an example. **Figure** 3.3 shows that when an electron with spin 1/2 scatters from a nonmagnetic impurity, there are two possible time reversal paths, clockwise (blue curve) and anticlockwise (red curve). As a result, the spin rotates by an angle of π and -π, respectively, and the phase difference between these two paths is a 2π rotation of spin. As we know, spin 1/2 systems have an antisymmetric wave function: $\psi(\theta) = -\psi(\theta + 2\pi)$. This implies that these two paths will interfere destructively and the quantum mechanical probability of the backscattering dramatically decreases. In other words, the backscattering is heavily suppressed and there is almost no dissipation. However, if the impurity carries a magnetic moment, the TRS will be broken in the system and the interference between the two paths is no longer destructive, which can then lead to dissipation.

The topologically protected edge or surface states possess another prominent property, a π Berry phase. The Berry phase is the phase picked up by an external parameter of a quantum system after it adiabatically makes a closed path in parameter space [74]. Consider a quantum system described by a time dependent Hamiltonian H which is specified by the parameter $\mathbf{R}(t)$. Assuming the system starts out at the n-th eigenstate $|n, \mathbf{R}(t)>$, then the parameter $\mathbf{R}$ adiabatically goes through a closed path C, and the Berry phase γ_n acquired during this process can be expressed as

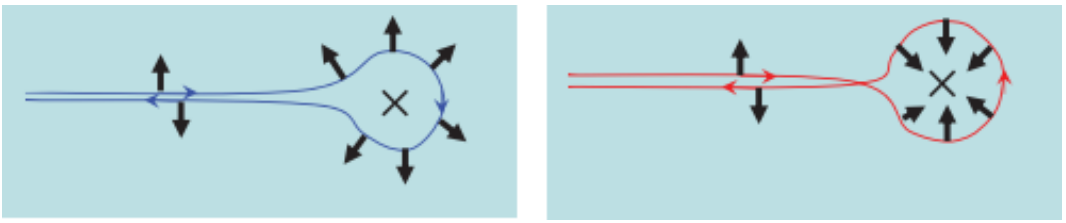

Figure 3.3: *A scheme of a backscattering by a nonmagnetic impurity for a quantum spin Hall edge state. There are two possible time reversal paths the electrons are scattered: one, going clockwise along the blue curve with spin rotating by π; the other, going anticlockwise along the red curve with spin rotating by -π. These two paths lead to a destructive interference and the backscattering is suppressed. Figures taken from Ref. [73].*

$$\gamma_n = \mathrm{i} \oint_c < n, \mathbf{R} | \nabla_R | n, \mathbf{R} > d\mathbf{R}. \tag{3.3}$$

As mentioned above, in topological insulators, the topologically protected edge or surface states have the property of spin-momentum locking. When an electron with spin locked to its momentum moves in a closed path in momentum space, it picks up a π Berry phase [75].

The existence of topologically protected edge or surface states is an important property of topological insulators. These states can be obtained by analytically solving the Hamiltonian of the explicit model of a material with open boundary conditions [76–79], such as has been done in models for HgTe-type compounds [8], Bi_2Se_3-type crystals [16], the perovskite oxide $BaBiO_3$ [80] and the KHgSb-type materials [81]. As an example we consider the Bernevig-Hughes-Zhang (BHZ) model for HgTe [8], which led to the experimental discovery of the first 2D TI material (CdTe/HgTe/CdTe quantum wells). This model is derived from $\mathbf{k} \cdot \mathbf{p}$ perturbation theory of bulk materials with a Taylor expansion up to the quadratic term. The effective Hamiltonian is written as follows:

$$H = \varepsilon(\mathbf{k})\mathrm{I}_{4\times4} + \begin{vmatrix} M(\mathbf{k}) & Ak_+ & 0 & 0 \\ Ak_- & -M(\mathbf{k}) & 0 & 0 \\ 0 & 0 & M(\mathbf{k}) & -Ak_- \\ 0 & 0 & -Ak_+ & -M(\mathbf{k}) \end{vmatrix} \tag{3.4}$$

with $\varepsilon(\mathbf{k}) = C - D\mathbf{k}^2$, $M(\mathbf{k}) = M_0 + B\mathbf{k}^2$ and $k_\pm = k_x \pm ik_y$. $\mathrm{I}_{4\times4}$ is the 4×4 unitary matrix. A, B, C, D, M are material parameters that can be determined by fitting the energy spectrum of the effective Hamiltonian to that of the *ab initio* calculation [16]. By diagonalizing the effective Hamiltonian **Equation** 3.4 with open boundary conditions, the topological edge states can be obtained on the condition that $M/B > 0$ which means an inverted band gap regime. The topological edge states are spin polarized.

3.2 Transport studies of the 3D topological insulator bulk

Even though the 3D topological insulator Bi_2Se_3 has an energy gap of about 0.2-0.3 eV [82, 83] in bulk, single crystalline from it shows metallic behavior in transport measurements. The conductivity is dominated by the bulk due to the presence of defects and impurities, which hampers a proper measurement of the transport properties of the topological surface states. Therefore, it is important to first understand the bulk properties of 3D topological insulators from the view point of their bulk carrier density. An interesting approach in this respect has recently been presented by Brahlek *et al.* [84]. Since the bulk Fermi energy $E_F = \hbar^2/(2m^*)(3\pi^2 N_{BD})^{2/3}$ under the assumption of isotropic Fermi surface and absolute zero temperature, where m^* is the effective mass and N_{BD} is the bulk carrier density, the Fermi energy E_F can be moved into the bulk conduction or valence bands when N_{BD} reaches a certain value, which results in a metallic bulk. Take Bi_2Se_3, which has an effective mass m^* of about $0.15m_e$ (m_e is the electron mass) [85], as an example. When the bulk carrier density is below 10^{17} /cm^3, E_F is pinned at the bottom of the conduction band [84]. To judge whether a metal-to-insulator transition (MIT) occurs with reducing carrier densities and E_F is situated in the band gap, there are two criteria, that of Mott and Ioffe-Regel.

The Mott criterion states the critical point for the MIT, that is $a_B N_{BD}^{1/3} \approx 0.25$ [86]. Here a_B is the effective Bohr radius, calculated using $a_B = \varepsilon(m_e/m^*)a_0$ in which ε denotes the dielectric constant and $a_0 = 0.5$ Å being the free space Bohr radius. The idea is simple: when the carrier density decreases, the average distance between the carriers increases and becomes larger than the effective Bohr radius, which results in the localization of the electrons bound to the atoms and no free movement of electrons between neighboring atoms. As a consequence, the metal changes to an insulator. This simple criterion has been applied to many systems as reported in Ref. [87], including doped semiconductors, high-T_c superconductors, metal-ammonia solutions and metal-noble gas alloys, to numerically predict for a MIT [88–92]. For the case of Bi_2Se_3, N_{BD} is calculated to be around $3\times$ 10^{14} cm^{-3} with $\varepsilon \approx 110$ and $m^* \approx 0.15m_e$ [85]. This value is two orders of magnitude smaller than the lowest density achieved so far for Bi_2Se_3 (around 10^{16} cm^{-3} [85]). Thus from the view point of the Mott criterion, the current topological insulators, such as Bi_2Se_3, are not intrinsic insulators.

The Ioffe-Regel criterion describes that when the mean free path ℓ of the electrons in a material is smaller than its Fermi wave vector k_F, that is, $k_F\ell < 1$, the electrons become trapped and the material goes through a metal-to-insulator transition [93]. For an isotropic 3D Fermi surface, k_F can be obtained by the formula $k_F = (3\pi^2 N_{BD})^{1/3}$ and ℓ can be calculated through the electron mobility $\mu = e\ell/\hbar k_F$, which results in $\ell = (\hbar\mu/e)(3\pi^2 N_{BD})^{1/3}$. Here e is the electron charge. Therefore, when $\mu < (e/\hbar)(3\pi^2 N_{BD})^{-2/3}$,

the material will be in a weakly insulating state even through the carrier density is larger than that calculated from the Mott criterion. The resistance behavior of this weakly insulating state (in 3D) can be described by 3D variable range hopping with $R \sim exp(T/T_0)^{1/4}$, where R is the resistance of the material, T is the temperature and T_0 is a constant depending on the density of states at the Fermi level [94]. Since this weakly insulating state is only truly insulating at the temperature around zero and stays conducting at a finite temperature, the materials at this state are generally called bad metals. **Figure** 3.4 shows the Mott and Ioffe-Regel criteria for the metal-to-insulator transition and the positions of well-known Bi-based topological insulators depending on their carrier densities N_{BD} and electron mobilities μ. The vertical line denotes the critical value of the bulk carrier density $N_{BD} = 3 \times 10^{14}$ cm^{-3} calculated based on the Mott criterion. The left region denotes truly insulating states in the Mott sense. The diagonal lines are obtained from the Ioffe-Regel criterion $k_F\ell \sim 0.3 - 3$. The region above the Ioffe-Regel criterion $k_F\ell \sim 3$ with high carrier density and high mobility belongs to good metals and the region below the Ioffe-Regel criterion $k_F\ell \sim 0.3$ having high carrier density but low mobility displays bad metals. Brahlek *et al.* [84] compiled a plot of the transport data of Bi-based topological insulators including Bi_2Se_3, Bi_2Te_3 , Bi_2Te_2Se and $Bi_{2-x}Sb_xTe_{3-y}Se_y$ which are obtained from Refs. [25, 27–29, 95–103]. Bi_2Se_3, Bi_2Te_3 are in the good metal region and Bi_2Te_2Se and $Bi_{2-x}Sb_xTe_{3-y}Se_y$ are in the bad metal region at the cost of low mobility, which challenges the observation of the Shubnikov-de Haas effect.

In 3D topological insulators, band-bending phenomena commonly occur due to the difference between the bulk and the surface Fermi levels. This results in the charge transfer between bulk and surface to balance the Fermi level in the material. Depending on the surface carrier density, there are three band-bending directions: flat band, bent upward and bent downward. Let us take Bi_2Se_3 as an example. The calculations are taken from Ref. [84] for the purpose of demonstration. First consider the flat band condition, that is, the Fermi levels of both the bulk and the surface are at the same position, which according to the Mott criterion will be at the bottom of the conduction band. Given that the Fermi level E_F of the surface is around 210 meV above the Dirac point [104] and the Fermi velocity $\upsilon_F \approx 4 \times 10^5$ m/s, the Fermi wave vector k_F is calculated to be around 0.08 Å^{-1} using the formula $E_F = \hbar k_F \upsilon_F$ for the Dirac linear dispersion. Then the carrier density of one surface state n_{SS} can be calculated from the formula $n_{SS} = k_F^2/4\pi$ to be around 5×10^{12} cm^{-2}. If $n_{SS} > 5 \times 10^{12}$ cm^{-2}, the conduction band needs to bend downward and the carriers are transferred from surface to bulk, resulting in a bulk carrier accumulation at the surface. If $n_{SS} < 5 \times 10^{12}$ cm^{-2}, the conduction band needs to bend upward and the carriers transfer from bulk to surface, resulting in a bulk carrier depletion at the surface. These three conditions are schematically shown in **Figure** 3.5(a)(b)(c) respectively. In the literature, due to the initial n_{SS}, some of Bi_2Se_3 crystals [100] and Bi_2Se_3 thin films [105] show upward band bending while some of them [102, 104] show

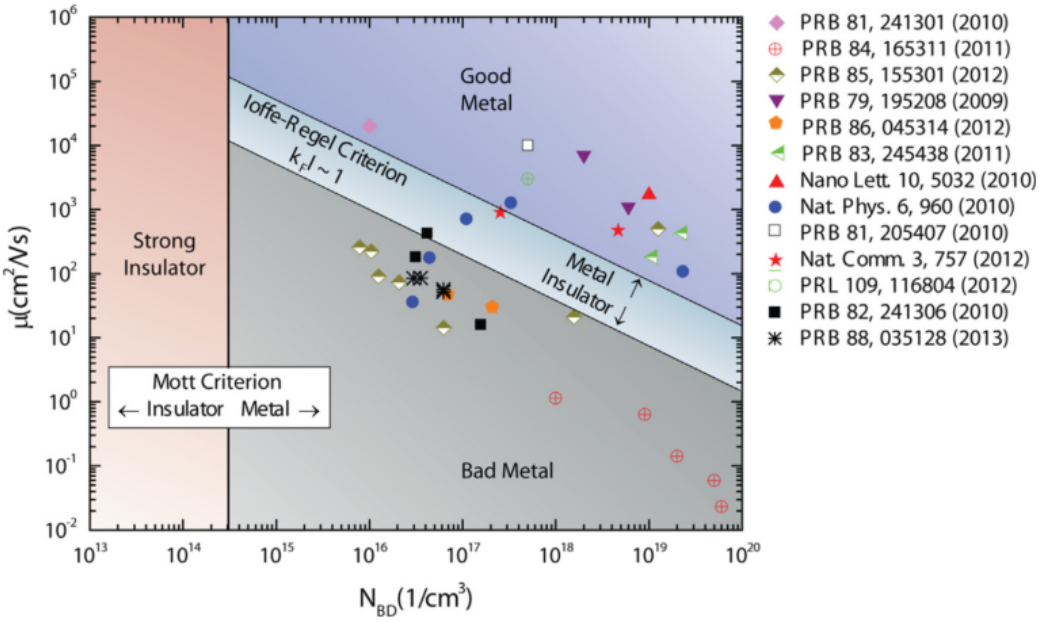

Figure 3.4: *A diagram of the Mott and Ioffe-Regel criteria for the metal-to-insulator transition. The vertical line denotes the critical value of the bulk carrier density $N_{BD} = 3 \times 10^{14}$ cm^{-3} calculated based on the Mott criterion. The diagonal lines are obtained from the Ioffe-Regel criterion $k_F \ell \sim 0.3 - 3$. The well-known Bi-based topological insulators, including Bi_2Se_3, Bi_2Te_3, $Bi_2Te_2Se_1$ and $Bi_{2-x}Sb_xTe_{3-y}Se_y$ are put into the diagram depending on their carrier densities N_{BD} and electron mobilities μ. Data are obtained from Refs. [25, 27–29, 95–103]. Figure taken from Ref. [84].*

downward band bending. In addition, the presence of the adsorbates at the surface could lead to downward band-bending of the bulk bands [84, 106]. Upward band bending is favourable for the observation of Shubnikov-de Haas Oscillations of the topological surface states [84].

3.3 Weak (anti-)localization

Weak anti-localization (WAL) and weak localization (WL) are quantum interference phenomena observed in transport measurements on disordered electron systems. WAL and WL give a correction to the conductivity of a material by enhancing or suppressing the conductivity with decreasing the temperature and show a negative or positive magneto-conductivity with a sharp change in small magnetic fields. In the following paragraphs we give the explanation of WAL as presented in Ref. [84, 107].

Conductivity is related to the scattering events of electrons on propagating through the material. When an electron encounters a scattering center, it has many different possible (closed) paths. In quantum mechanics, conductivity is based on the probability obtained from summing up the quantum mechanical amplitudes of every path, which results in quantum interference terms. The interference terms between most paths are usually

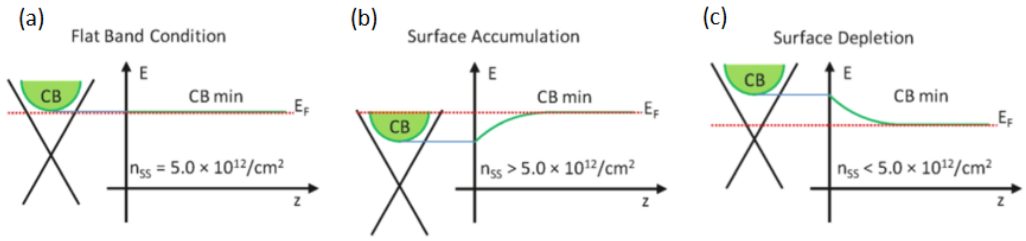

Figure 3.5: *Three band-bending directions of Bi_2Se_3 based on the surface carrier density: (a) flat band condition, the Fermi levels of both the bulk and the surface are at the same position — the bottom of the conduction band according to the Mott criterion, resulting in the surface carrier density $n_{SS} \approx 5 \times 10^{12}$ cm^{-2}; (b) downward band-bending, when $n_{SS} > 5 \times 10^{12}$ cm^{-2}, the conduction band bends downward and the carriers transfer from surface to bulk, resulting in a bulk carrier accumulation at the surface; (c) upward band-bending, when $n_{SS} < 5 \times 10^{12}$ cm^{-2}, the conduction band bends upward and the carriers transfer from bulk to surface, resulting in a bulk carrier depletion at the surface. Here E is the energy, z is the distance relative to the surface of the material, E_F is the Fermi energy with blue line and red dashed line denoting the bulk and surface Fermi level respectively. Figure taken from Ref. [84].*

averaged out to zero, except for those between the time reversible paths in which electrons go in a clockwise or anticlockwise manner in a system possessing time reversal symmetry. Assume the electron wave function before scattering is denoted as ψ. During scattering, the electron will gain a phase $\pm\phi$ for the clockwise and anticlockwise paths, respectively, which results in the wave functions $\psi_+ = \psi e^{i\phi}$ and $\psi_- = \psi e^{-i\phi}$. The probability for the electron to return to the original position is given by $P = |\psi_+ + \psi_-|^2 = |2\psi\cos(\phi)|^2$. In the case without spin-orbit coupling, the phase $\phi = 0$, and the two paths interfere constructively, giving $P = 4|\psi|^2$. This should be compared to the classical case without interference effects for which the probability $P = |\psi|^2 + |\psi|^2 = 2|\psi|^2$. As a result, in the quantum situation, the probability for the electrons to return to the original position is greater, which causes a suppression of the conductivity of the material, known as weak localization or WL. On the other hand, in a system with strong spin-orbit coupling, the phase $\phi = \pi$, and the two paths interfere destructively, yielding $P = 0$. Now the probability for the electrons to return to their original location is suppressed, resulting in an enhancement of the conductivity of the material, known as weak antilocalization or WAL. When an external magnetic field is applied, time reversal symmetry is broken and an extra phase $e\Phi/\hbar$ (Φ is the magnetic flux) is acquired by the carriers. With the increase of the applied magnetic field, the extra phase accordingly increases and gradually destroys the exact constructive or destructive interference operative in WL or WAL, which leads to a positive or negative magneto-conductivity, respectively. **Figure** 3.6 shows these two effects. In addition, as pointed out in Ref. [108], three characteristic length scales are important to consider whether WL or WAL may occur. First, the mean free path ℓ, the average distance travelled by an electron before scattering, should be smaller than

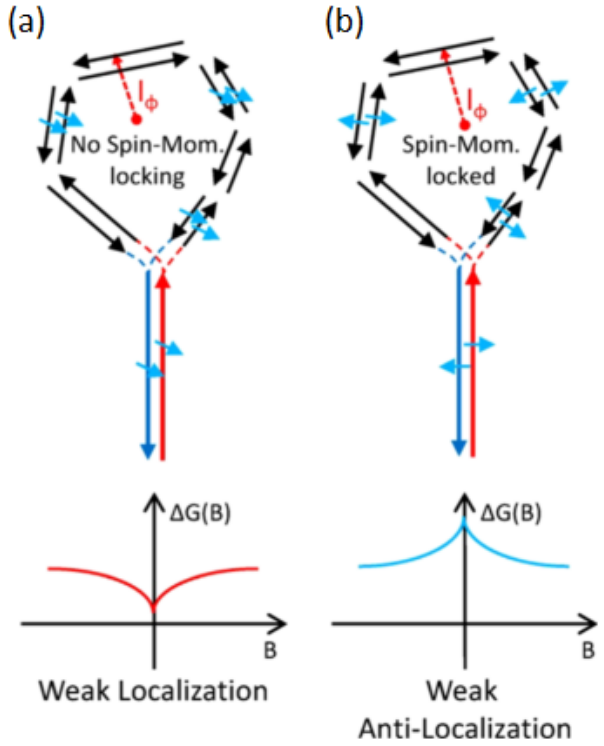

Figure 3.6: *Schematic illustration of constructive and destructive interference between time reversal paths, and the behavior of the conductance in a small magnetic field: positive and negative magneto-conductance $\Delta G(B)$ for (a) weak localization and (b) weak anti-localization, respectively. ℓ_ϕ is the phase coherence length. Figures taken from Ref. [84].*

the sample size L, otherwise the electrons can travel through the sample without being scattered. Also, the phase coherence length ℓ_ϕ, the average distance over which an electron retains its phase coherence, should be larger than the mean free path ℓ: a prerequisite for the quantum interference. In short, $L > \ell$, $\ell_\phi > \ell$.

The magnetic field dependence of the conductivity σ_{xx} of the WL and WAL effect in 2D systems is normally analyzed using the Hikami-Larkin-Nagaoka (HLN) formula [109]:

$$\Delta\sigma_{xx}(B) = \sigma_{xx}(B) - \sigma_{xx}(0) = \alpha\frac{e^2}{2\pi^2\hbar}[\Psi(\frac{\hbar}{4e\ell_\phi^2 B} + \frac{1}{2}) - \ln(\frac{\hbar}{4e\ell_\phi^2 B})] \tag{3.5}$$

where Ψ is the digamma function, $\hbar$ is Planck's constant divided by 2π, e is the electron charge, B is the magnetic field. α and ℓ_ϕ are two fitting parameters: ℓ_ϕ being the phase coherence length, and α a dimensionless parameter related to the number of 2D conduction channels. $\alpha = 1$ for WL and -1/2 for WAL for each conduction channel. As ℓ_ϕ is usually determined by inelastic scattering due to the electron-phonon and electron-electron interactions, ℓ_ϕ is expected to be temperature dependent. It is empirically expressed as $\ell_\phi \propto T^{-p/2}$ [110] with p related to dephasing mechanisms and dimensionality [111].

For 3D topological insulators, the topological surface states are spin-momentum locked and carry a π Berry phase, which can lead to the observation of WAL. Experimentally,

the α fitted from the WAL using the HLN formula is mostly in the range of -0.4 to -1.1, which indicates the contribution from one or two surfaces bands [97, 112–115]. In order to investigate the contributions from the bulk for WAL, Lu and Shun have derived a unified model, the 2D modified Dirac model [107], which shows the magnetoconductivity of bulk bands may have WL or unitary behavior. The bulk channels with unitary behavior in the magnetoconductivity will not influence the study of the WAL of the surface states, while the bulk channels with WL behavior in the magnetoconductivity can compensate the WAL of the surface states.

3.4 The Shubnikov-de Haas effect

The Shubnikov-de Haas effect (SdH) is a periodic oscillation of the conductivity of a material as a function of the magnetic field B and was discovered by L. Shubnikov and W.J. de Haas in 1930. The oscillation is periodic in $1/B$ and originates from the Landau quantization of the electron energy. In the following paragraphs the SdH effect is explained using Ref. [116].

Consider an electron with an isotropic effective mass m^* in a magnetic field B applied in the z direction. In this case we choose the vector potential in the gauge $\mathbf{A} = (0, Bx, 0)$, and the Hamiltonian is given by

$$\mathbf{H} = \frac{p_x^2}{2m^*} + \frac{1}{2m^*}(p_y - eBx)^2 + \frac{p_z^2}{2m^*}. \tag{3.6}$$

For simplicity, the interaction between the spin of the electron and the magnetic field is ignored. If we write for the momentum $p_y = \hbar k_y$, and change the coordinate x to $x' = x - x_0$ with $x_0 = \frac{\hbar k_y}{eB}$, the Hamiltonian can be written as

$$\mathbf{H} = \frac{p_x'^2}{2m^*} + \frac{1}{2}m^*{\omega_c}^2 x'^2 + \frac{p_z^2}{2m^*}, \tag{3.7}$$

where we used the definition $\omega_c = eB/m^*$. This is the Hamiltonian for a quantum harmonic oscillator plus a constant energy along the direction of the magnetic field. Therefore, the energy of the states is given by

$$E_n = (n + \frac{1}{2})\hbar\omega_c + \frac{\hbar^2 k_z^2}{2m^*},\ n = 0, 1, 2, \ldots. \tag{3.8}$$

The energy is quantized in the k_x-k_y plane and continuous in the k_z direction, which is known as Landau quantization. The quantized energy levels are called Landau levels (LL). The quantization scheme in **k** space is shown in **Figure** 3.7. For simplicity, we assume $k_z = 0$ and consider the degeneracy of each LL. Suppose a material within a rectangular shape of size of L_x, L_y. The center of the quantum harmonic oscillator $x_0 = \frac{\hbar k_y}{eB}$ should be inside the material, that is $0 \leq x_0 \leq L_x$. Besides, k_y is quantized in units of $2\pi/L_y$, that is

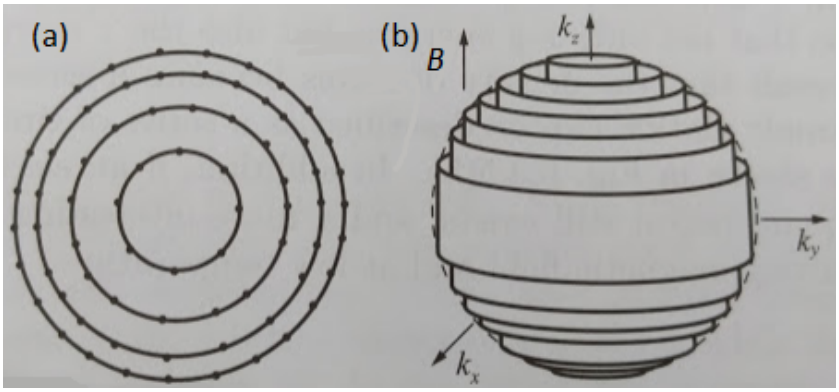

Figure 3.7: *Quantization scheme for electrons in the magnetic field shown (a) in the k_x-k_y plane and (b) in the whole of **k** space. Figure taken from Ref. [116].*

$\Delta k_y = 2\pi/L_y$, which means x_0 takes a series of values separated by $\Delta x_0 = 2\pi\hbar/eBL_y$. The degeneracy of each LL is

$$D = \frac{L_x}{\Delta x_0} = L_x L_y \frac{eB}{2\pi\hbar} = \frac{eB}{2\pi\hbar} S. \tag{3.9}$$

Here $S = L_x L_y$ is the area of the material perpendicular to the magnetic field. When considering the spin degeneracy, a factor of 2 needs to be taken into account. The density of states (DOS) of the 2D system is $g_{2D}(E) = \frac{eB}{\pi\hbar}$. To obtain the DOS of the 3D system, the density of states (DOS) of the k_z direction $g_{1D}(E) \propto [E - (n + 1/2)\hbar\omega]^{-1/2}$ should be taken into account which results in

$$g_{3D}(E) = \frac{eB}{\pi\hbar} g_{1D}(E). \tag{3.10}$$

As the magnetic field increases, the separation ($\Delta E(k_z) = \hbar\omega$) between the Landau levels increases. Therefore the highest filled Landau level sweeps through the Fermi level and becomes empty (see **Figure** 3.8). During this process, the conductance of the system shows a peak. Then, as the field continues to rise, the process repeats itself. For simplicity, assuming $k_z = 0$ and $T = 0$ K and the number of electrons is N. The Fermi level is E_F, and is in the middle of a Landau level. When the magnetic field increases to B_n, E_F is located just above the n-th Landau level, and the conductance will show a minimum. All n Landau levels are occupied and

$$N = S\frac{eB_n}{\pi\hbar} \times n \tag{3.11}$$

As the magnetic field continuously increases, the $(n-1)$-th Landau level will now move up to the Fermi level E_F. When E_F is at the middle of the $(n-1)$-th Landau level, the conductance will show a maximum. When the magnetic field increases to B_{n-1}, E_F is located just above the $(n-1)$-th Landau level, and the conductance will show a minimum again and

$$N = S\frac{eB_{n-1}}{\pi\hbar} \times (n-1) \tag{3.12}$$

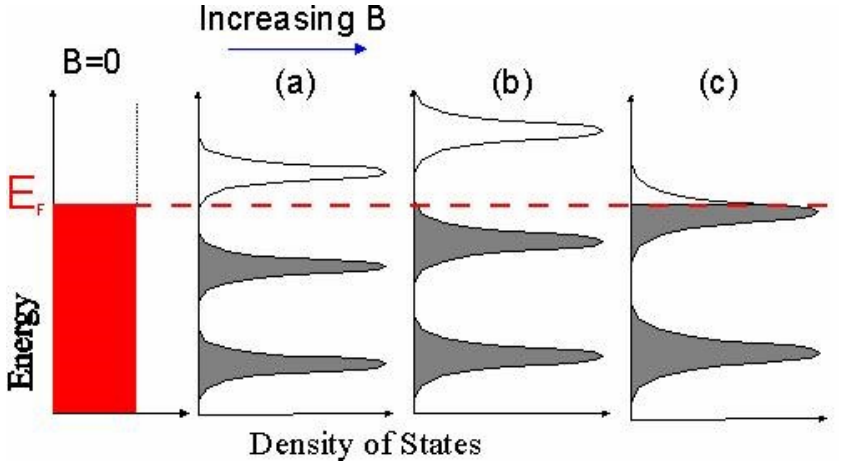

Figure 3.8: *Scheme of the filling of the Landau levels with increasing the magnetic field. Figure taken from Ref. [118]*

From **Equation** 3.11 and 3.12, we obtain

$$\Delta(\frac{1}{B}) = (\frac{1}{B_n} - \frac{1}{B_{n-1}}) = \frac{eS}{\pi\hbar N} \tag{3.13}$$

The conductance shows minima at B_n and B_{n-1}, and $\Delta(1/B) = (1/B_n - 1/B_{n-1})$ is a constant, which means the conductance oscillates with a period of $1/B$. It is known that the density of states in 2D k space for the free electrons is $S/2\pi^2$, then the area of the Fermi surface filled by N electrons is $A_k(E_F) = 2\pi^2 N/S$. Therefore, **Equation** 3.13 can be written as

$$\Delta(\frac{1}{B}) = \frac{2\pi e}{\hbar}\frac{1}{A_k(E_F)} \tag{3.14}$$

The oscillation period therefore depends on the extremal area of the Fermi surface $A_k(E_F)$, which was proved by Onsager [117] in 1952. When the oscillations originate from a 2D Fermi surface, there is only one extremal area of the Fermi surface and therefore only a single oscillation period or frequency is expected. When rotating the material with respect to the magnetic field, the oscillation frequency will show a cosine dependence on the angle between the normal direction of the material surface and the field direction: i.e. the quantum oscillations will be stationary when plotted against $1/B\cos\theta$

At the same time, the DOS of the Landau levels (see **Equation** 3.10) also increases with the increase of the magnetic field, which results in the increase of the amplitude of the oscillations. The analysis of the amplitude of the SdH oscillations can be carried out with the help of Lifshitz-Kosevich theory [119]

$$\Delta G_{xx} \propto R_T R_D \cos[2\pi(\frac{F}{B} - \gamma)], \tag{3.15}$$

where $R_T = \frac{\alpha T}{B}/\sinh(\frac{\alpha T}{B})$ with $\alpha = 2\pi^2 k_B m_c/\hbar e$ and $R_D = \exp(-\alpha T_D/B)$ with $T_D = \hbar/2\pi k_B \tau_D$ are called the thermal and Dingle damping factors, respectively, F is the oscillation frequency and γ is the phase factor. From the equation above we can acquire

important transport parameters, for example the cyclotron mass m_c. When fixing the magnetic field B, R_D does not change, but R_T shows a temperature dependence from which the cyclotron mass m_c can be obtained through fitting. If we then fix the temperature T, the oscillation amplitudes have a magnetic field dependence which allows one to obtain the Dingle temperature T_D. Furthermore, some other transport parameters such as the Fermi velocity υ_F, mean free path ℓ and mobility μ can also be calculated.

Importantly, the phase factor γ can also be obtained, as the conductance shows the n-th minimum when n Landau levels are completely filled. Then, according to **Equation** 3.15,

$$2\pi(\frac{F}{B_n} - \gamma) = (2n-1)\pi. \tag{3.16}$$

From a linear fit of the plot of $1/B_n$ versus n, the intercept is $\gamma - 1/2$. When $\gamma = 1/2$ or 0, it corresponds to the system with either 0 or π Berry phase, respectively.

The conditions for the observation of SdH oscillations are $\omega_c\tau > 1$ (τ is the scattering time, the separation between the Landau levels should be larger than the line broadening due to scattering) and $\hbar\omega_c > k_BT$ (the separation between the Landau levels should be larger than their thermal broadening). This means that to observe SdH oscillations materials should have high mobility ($\omega_c\tau > 1$ can be transformed into $\mu B > 1$, μ is the mobility) and high magnetic fields and low temperatures should be available.

3.5 Criterion for identification of topological superconductors

Topological superconductors have attracted much attention in the condensed matter physics community due to the existence of gapless surface Andreev bound states that are predicted to host Majorana zero modes [120]. It is important, therefore, to distinguish topological superconductors from normal superconductors. Fu and Berg have provided a criterion to identify time-reversal-invariant topological superconductors with inversion symmetry, that is, (i) the superconducting pair wave function has odd-parity symmetry and the superconducting gap is fully gapped; (ii) the Fermi surface encloses an odd number of time-reversal invariant momenta [121]. The Fermi surface topology for topological superconductors (point (ii)) can be extended from that of topological insulators discussed above due to the analogy between the Bogoliubov-de Gennes Hamiltonian of a superconductor and the Bloch Hamiltonian of a band insulator. Here, we focus on odd-parity superconducting pairing. A superconducting pair wave function consists of an orbital (spatial) and a spin component. In a simple case, the orbital component is labeled by the orbital angular momentum L with $L = 0, 1, 2, \ldots$, and the spin component can be presented by the spin angular momentum S with $S = 0, 1$ for the spin-singlet and spin-triplet state respectively. Spin-triplet pairing is referred as odd-parity pairing. A famous example of a topological

Table 3.1: *The form of the pairing potential, irreducible representation, spin state, orbital state, and energy gap structure for four different pairing symmetries. c carries an orbital index (1 or 2), and spin index ($\uparrow$ or $\downarrow$). Table adapted from Ref. [127]*

Pairing potential	Form	Representation	Spin	Orbital	Energy gap
$\hat{\Delta}_1$	$c_{1\uparrow}c_{1\downarrow}$ + $c_{2\uparrow}c_{2\downarrow}$ $c_{1\uparrow}c_{2\downarrow}$ - $c_{1\downarrow}c_{2\uparrow}$	A_{1g}	Singlet	Intra	Isotropic full gap
$\hat{\Delta}_2$	$c_{1\uparrow}c_{2\downarrow}$ + $c_{1\downarrow}c_{2\uparrow}$	A_{1u}	Triplet	Inter	Anisotropic full gap
$\hat{\Delta}_3$	$c_{1\uparrow}c_{1\downarrow}$ - $c_{2\uparrow}c_{2\downarrow}$	A_{2u}	Singlet	Intra	Point nodes at poles
$\hat{\Delta}_4$	($c_{1\uparrow}c_{2\uparrow}$, $c_{1\downarrow}c_{2\downarrow}$)	E_u	Triplet	Inter	Point node on equator

superfluid is the time-reversal-invariant ^{3}He B phase with L=1 and S=1 [56, 122, 123]. For the electron doped TI, $Cu_xBi_2Se_3$, Fu and Berg developed a two-orbital model to investigate the pairing symmetry based on the $Cu_xBi_2Se_3$ crystal point group D_{3d} [121]. According to group theory, four different pairing symmetries, with representations A_{1g}, A_{1u}, A_{2u}, and E_u were found in the D_{3d} point group that were assigned to the corresponding pairing order parameters $\hat{\Delta}_i$, $i = 1, \ldots, 4$. **Table** 3.1 shows the symmetry properties of $\hat{\Delta}_i$. Except for $\hat{\Delta}_1$, the pairings have odd-parity symmetry, among which only $\hat{\Delta}_2$ pairing has a full superconducting gap. This is in agreement with specific heat data reported in Ref. [124]. $\hat{\Delta}_2$ pairing was considered to be the most likely pairing state for the topological superconducting phase in $Cu_xBi_2Se_3$ according to the criterion of Fu and Berg. Soon afterwards, Fu proposed that the $\hat{\Delta}_4$ pairing state with the 2D representation E_u would also be fully gapped in $Cu_xBi_2Se_3$, when taking into account the spin-orbit interaction associated with the hexagonal warping of the Fermi surface. Thus, the $\hat{\Delta}_4$ state is also a possible topological superconducting phase [125]. We remark that only the $\hat{\Delta}_4$ pairing matches the experimental observation in NMR measurements of rotational symmetry breaking in the Knight shift in the basal plane [125, 126]. According to the two-orbital model mentioned above, the $\hat{\Delta}_4$ pairing generates a subsidiary nematic order with a direction $\mathbf{n} = (n_x, n_y)$ in the basal plane determined by zero total spin. Only when the nematic direction $\mathbf{n}$ is along one of the three twofold axes, that is $\mathbf{n} = (\cos\theta, \sin\theta)$ with $\theta = 0, \pm\pi/3, \pm 2\pi/3$ (see **Figure** 3.9(a) for the coordinate system), are there nodes in the superconducting gap. For example, when $\mathbf{n} = \hat{x}$, there are nodes along y in the superconducting gap (see **Figure** 3.9(c)). In all other cases, the nodes are destroyed by hexagonal warping and a full superconducting gap is present. In particular, when $\mathbf{n} = \hat{y}$, the structure of the superconducting gap is as shown in **Figure** 3.9(d).

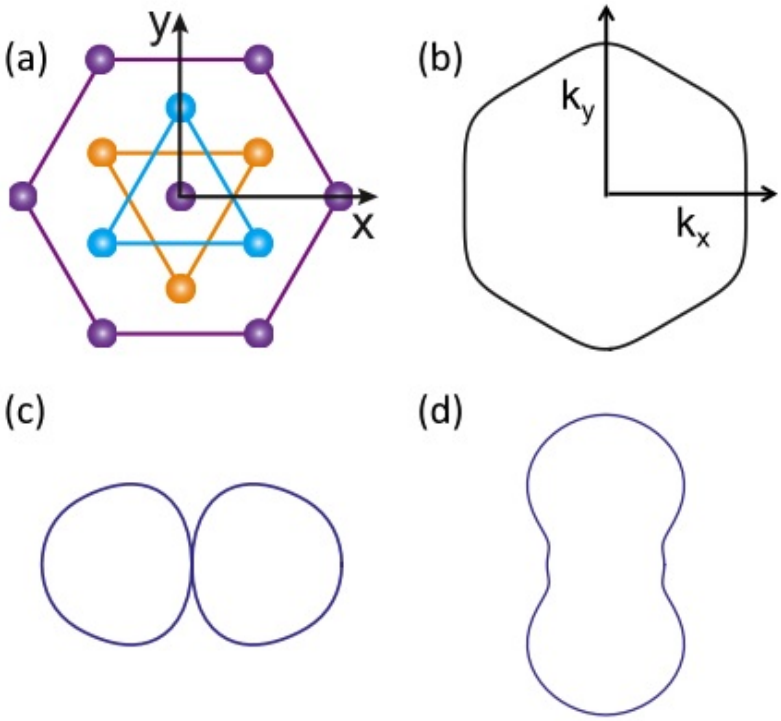

Figure 3.9: *(a) View of the crystal structure of $Cu_xBi_2Se_3$ along the c-axis. The coordinates in the basal plane are x and y, where the x-axis is perpendicular to a mirror plane. (b) Fermi contour at $k_z = 0$. (c) and (d) display the angular dependence of the anisotropic superconducting gap at $k_z = 0$ with the Fermi contour for the $\hat{\Delta}_4$ pairing being shown for $\mathbf{n} = \hat{x}$ and $\mathbf{n} = \hat{y}$, respectively. Figure taken from Ref. [125]*

Chapter 4

Low carrier concentration crystals of the topological insulator $Bi_{2-x}Sb_xTe_{3-y}Se_y$: a magnetotransport study

In 3D topological insulators achieving a genuine bulk-insulating state is an important research topic. Recently, the material system $(Bi,Sb)_2(Te,Se)_3$ (BSTS) has been proposed as a topological insulator with high resistivity and a low carrier concentration (Ren *et al.* [29]). Here we present a study to further refine the bulk-insulating properties of BSTS. We have synthesized $Bi_{2-x}Sb_xTe_{3-y}Se_y$ single crystals with compositions around $x = 0.5$ and $y = 1.3$. Resistance and Hall effect measurements show high resistivity and record low bulk carrier density for the composition $Bi_{1.46}Sb_{0.54}Te_{1.7}Se_{1.3}$. The analysis of the resistance measured for crystals with different thicknesses within a parallel resistor model shows that the surface contribution to the electrical transport amounts to 97 % when the sample thickness is reduced to 1 μm. The magnetoconductance of exfoliated BSTS nanoflakes shows 2D weak antilocalization with $\alpha \simeq -1$ as expected for transport dominated by topological surface states.

4.1 Introduction

Three dimensional (3D) topological insulators (TIs) have generated intense research interest, because they offer unmatched opportunities for the realization of novel quantum states [1, 3]. Theory predicts the interior of the TI sample (the bulk) is insulating, while the metallic surface states have a Dirac cone dispersion and a helical spin structure. Because of time reversal symmetry and a strong spin-orbit interaction, the surface charge carriers are insensitive to backscattering from non-magnetic impurities and disorder. This makes TIs promising materials for a variety of applications, ranging from spintronics and magnetoelectrics to quantum computation [123, 128, 129]. The topological surface states of exemplary TIs, such as $Bi_{1-x}Sb_x$, Bi_2Te_3, Bi_2Se_3, Sb_2Te_3, *etc*., have been probed compellingly via surface-sensitive techniques, like angle-resolved photoemission spectroscopy (ARPES) [15, 17, 19, 130] and scanning tunneling microscopy (STM) [21, 22]. However, the transport properties of the surface states turn out to be notoriously difficult to investigate, due to the dominant contribution from the bulk conduction resulting from intrinsic impurities and crystallographic defects. At the same time, potential applications strongly rely on the tunability and robustness of charge and spin transport at the device surface or interface. Therefore, achieving surface-dominated transport in the current families of TI materials remains a challenging task, in spite of the progress that has been made recently, including charge carrier doping [96, 99], thin film engineering and electrostatic gating [131, 132].

Recently, it was reported that the topological material Bi_2Te_2Se exhibits variable range hopping (VRH) behavior in the transport properties, which leads to high resistivity values exceeding $1\ \Omega$cm at low temperatures [27]. This ensures the contribution from the bulk to electrical transport is small. At the same time the topological nature of the surface states was probed by Shubnikov - de Haas oscillations [27, 28]. Further optimizing studies include different crystal growth approaches [26], Bi excess [133] and Sn doping [95, 134]. Bi_2Te_2Se has an ordered tetradymite structure (spacegroup $R\bar{3}m$) with quintuple-layer units of Te-Bi-Se-Bi-Te with the Te and Se atoms occupying distinct lattice sites. Next the composition of Bi_2Te_2Se was optimized by Ren *et al.* [29] by reducing the Te:Se ratio and introducing Sb on the Bi sites. An extended scan of isostructural $Bi_{2-x}Sb_xTe_{3-y}Se_y$ (BSTS) solid solutions resulted in special combinations of x and y, notably $x = 0.5$ and $y = 1.3$, where the resistivity attains values as large as several Ωcm at liquid helium temperature. In addition values of the bulk carrier concentration as low as 2×10^{16} cm^{-3} were achieved [30]. The topological properties of BSTS samples with x and y near these optimized values were subsequently examined by a number of techniques, like ARPES [135], terahertz conductivity [136], and STM and STS [137, 138].

In this paper we report an extensive study conducted to confirm and further investigate the bulk-insulating properties of $Bi_{2-x}Sb_xTe_{3-y}Se_y$ with x and y around 0.5 and 1.3,

respectively. In the work of Ren *et al.* [29] the BSTS composition was scanned with a step size Δx and Δy of typically 0.25. For our study we prepared single crystals with much smaller step sizes, typically $\Delta x = 0.02$ and $\Delta y = 0.10$. Magnetotransport measurements showed that the carrier type in $Bi_{2-x}Sb_xTe_{1.7}Se_{1.3}$ changes from hole to electron when $x < 0.5$, while the carrier type remains unchanged in $Bi_{1.46}Sb_{0.54}Te_{3-y}Se_y$ when y is varied from 1.2 to 1.6. The composition $Bi_{1.46}Sb_{0.54}Te_{1.7}Se_{1.3}$ presented the highest resistivity (12.6 Ωcm) and lowest bulk carrier density (0.2×10^{16} cm^{-3}) at $T = 4$ K.

In addition, the effect of reducing the sample thickness on the ratio between the surface and bulk conductivity was investigated. For this study we used the composition $Bi_{1.46}Sb_{0.54}Te_{1.4}Se_{1.6}$ and gradually thinned down a 140 μm thick sample to 6 μm. The analysis of the resistance data in terms of a two-resistor model reveals the surface contribution to the total conductivity can be as large as 97 % at $T = 4$ K when the sample thickness is $\sim$1 μm. The angular variation of the magnetoconductance of a nanoflake with composition $Bi_{1.46}Sb_{0.54}Te_{1.7}Se_{1.3}$ shows a pronounced weak antilocalization (WAL) term, whose field dependence followed the Hikami-Larkin-Nagaoka formula [109] with a fit parameter α close to -1 as expected for topological surface states [107]. We conclude that good quality BSTS single crystals can be achieved via careful compositional variation and thickness reduction such that the topological surface transport overwhelms the bulk conduction channel.

4.2 Methods

High quality $Bi_{2-x}Sb_xTe_{3-y}Se_y$ single crystals were obtained by melting stoichiometric amounts of the high purity elements Bi (99.999 %), Sb (99.9999 %), Te (99.9999 %) and Se (99.9995 %). The raw materials were sealed in an evacuated quartz tube which was vertically placed in the uniform temperature zone of a box furnace. Both this choice of growth approach and our choice to keep the growth boules of small size (maximal dimension 1 cm) were made so as to maximize the homogeneity within each single crystal run. The molten material was kept at 850 °C for 3 days and then cooled down to 520 °C with a speed of 3 °C/h. Next the batch was annealed at 520 °C for 3 days, followed by cooling to room temperature at a speed of 10 °C/min. In the following all x- and y-values refer to nominal concentrations. Electron probe micro analysis (EPMA) carried out on six crystals selected within the series showed the nominal compositions to be in good agreement with the stoichiometry in the final single crystals produced. In addition, EPMA showed there to be no observable spatial inhomogeneity across the sample, which is in keeping with the homogeneous secondary electron images the crystals gave and the lack of any measurable impurity phases seen in standard X-ray diffraction characterisation of the samples. The systematic thickness dependence reported in the following also argues for an acceptable level of sample homogeneity. The as-grown platelet-like single crystals

were cleaved with Scotch tape parallel to the ab-plane to obtain flat and shiny surfaces at both sides. Care was taken to maintain a sample thickness of ~ 100 μm for all samples. Next the samples were cut into a rectangular shape using a scalpel blade. For the transport measurements in a five-probe configuration, thin (50 μm) copper wires were attached to the samples using silver paint. Current and voltage contacts were made at the edges of the sample to ensure contact with the bulk and the upper and lower surface. The exposure time to air between cleaving and mounting the samples in the cryostat was kept to a minimum of about 1 h.

Four-point, low-frequency, ac-resistivity and Hall effect measurements were performed in a MaglabExa system (Oxford Instruments) equipped with a 9 T superconducting magnet in the temperature range from 4 to 300 K. The excitation current was typically 1000 μA. Selected measurements were spot-checked using a PPMS system (Dynacool, Quantum Design) with 100 μA excitation current. Measurements were always made for two polarities of the magnetic field after which the Hall resistance, R_{xy}, and longitudinal resistance, R_{xx}, were extracted by symmetrization. When investigating the effect of the sample thickness, layers were removed from the sample by Scotch tape. Special care was taken to maintain a uniform thickness across the sample, as well as the same lateral dimensions. For the thickness-dependent series, the resistance measurements were made in a bath cryostat in the temperature range 4.2-300 K using an AC Resistance Bridge (Model 370, LakeShore Cryotronics).

For our investigation of the WAL effect, flakes of thickness in the range of 80 to 200 nm were mechanically exfoliated on silicon-on-insulator substrates. Au Hall bar electrodes were prepared by standard photolithography followed by e-beam lithography and argon ion etching to shape the flake in a Hall bar structure. During the fabrication steps we covered the devices with e-beam or photoresist to avoid damaging and contamination of the surface. The Hall bars have a total length of 24 μm and have widths in the range of 0.5-2.0 μm. Transport measurements on these samples were carried out in a PPMS (Dynacool, Quantum Design) in the temperature range 2-300 K with an excitation current of 5 μA. The field-angle dependence of WAL was measured for a rotation of the Hall bar around its long axis (the current direction).

ARPES measurements were carried out on cleaved single crystals of Bi_2Se_3 and $Bi_{1.46}Sb_{0.54}Te_{1.7}Se_{1.3}$ at the SIS beamline of the Swiss Light Source at the Paul Scherrer Institute. The photon energies used were 27 and 30 eV, and the sample temperature was 17 K. In both cases, the surfaces were exposed to sufficient residual gas such that the downward band bending – as documented in [139, 140] for Bi_2Se_3 – has saturated and thus was no longer changing as a function of time. The energy resolution was 15 meV.

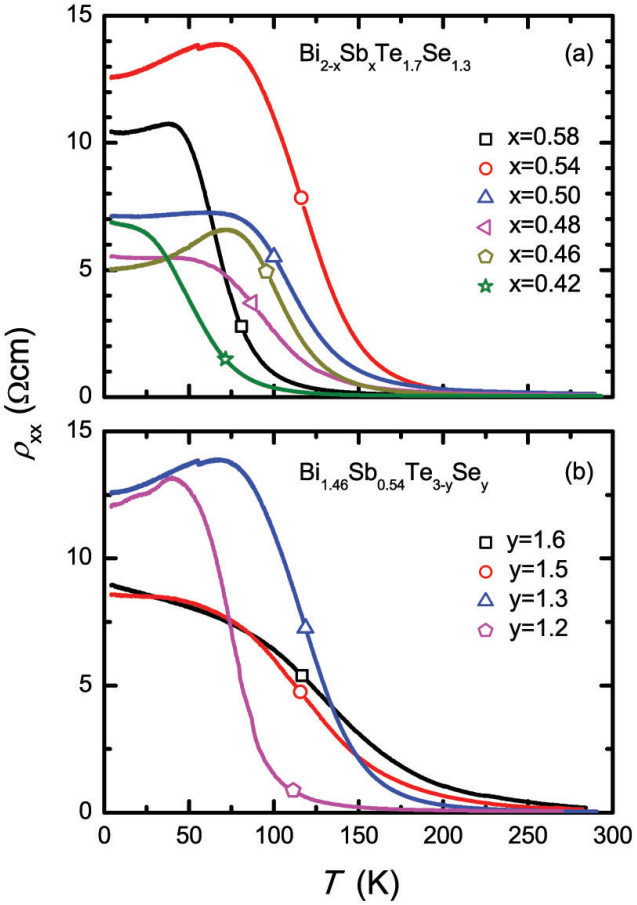

Figure 4.1: *Temperature dependence of the resistivity of $Bi_{2-x}Sb_xTe_{3-y}Se_y$ crystals with (a) $y = 1.3$ and x-values as indicated, and (b) $x = 0.54$ and y-values as indicated. The typical sample thickness is 100 μm.*

4.3 Results and analysis

4.3.1 Composition variation

In this section we present the resistivity, ρ_{xx}, and Hall effect, ρ_{xy}, data. Rather than simply re-growing the optimal (x, y)-values of (0.5,1.3) reported by Ren *et al.* [29], we first varied x from 0.42 to 0.58 while keeping y fixed at 1.3. Next, we fixed x at 0.54 and varied y from 1.2 to 1.6. The size of the steps taken in both x and y were smaller than those reported earlier. The temperature variation of the resistivity for these two series of crystals is shown in **Figure** 4.1(a) and **Figure** 4.1(b), respectively. All the samples display an overall similar resistivity behavior. Upon cooling below 300 K the resistivity increases first slowly and then faster below ~ 150 K till ρ_{xx} reaches a maximum value at 50-100 K. Next the resistivity shows a weak decrease and levels off towards 4 K. The increase of the resistivity can be described by an activated behavior $\rho_{xx} \propto \exp(\Delta/k_BT)$ where Δ is the activation energy, followed by a 3D VRH regime $\rho_{xx} \propto \exp[(T/T_0)^{-1/4}])$ where T_0 is a constant [29]. These different regimes show considerable overlap as illustrated

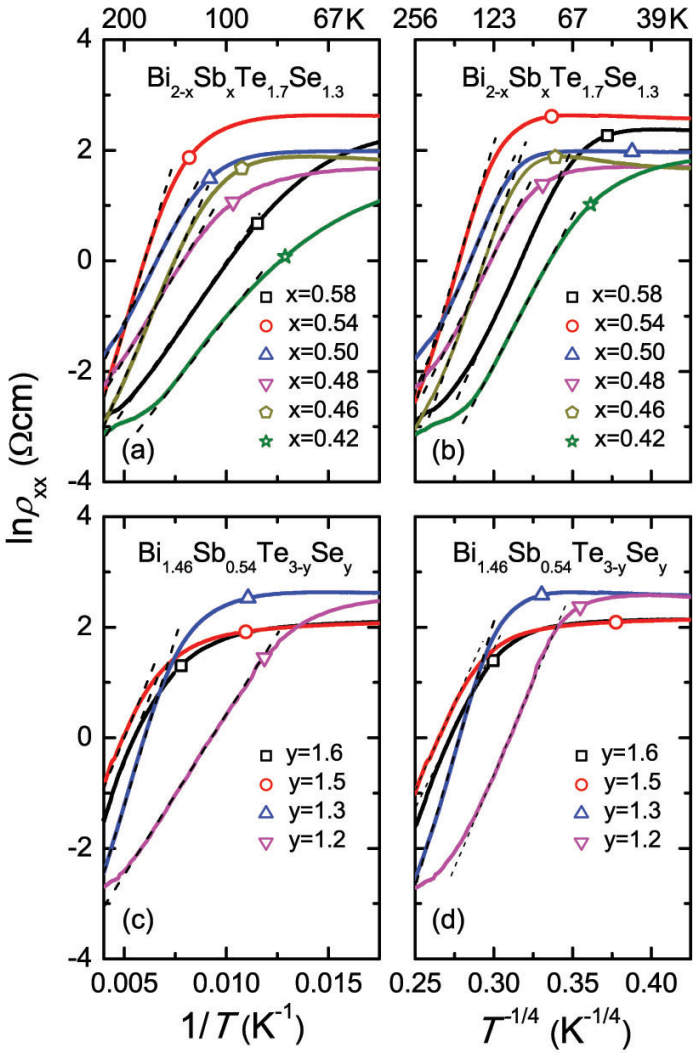

Figure 4.2: *Temperature variation of the resistivity of BSTS in a plot of* $\ln \rho_{xx}$ *versus* $1/T$ *in frames (a) and (c), and versus* $T^{-1/4}$ *in frames (b) and (d). The linear dashed lines represent the activation behavior and the 3D VRH behavior (see text). In frames (a) and (b) we have traced the resistivity for* $y = 1.3$ *and* x*-values as indicated, and in frames (c) and (d) the resistivity for* $x = 0.54$ *and* y*-values as indicated.*

in **Figure** 4.2(a) and (b), and in **Figure** 4.2(c) and (d). Below ~ 50 K the resistivity is described by a parallel circuit of the insulating bulk and the metallic surface states (see the next subsection).

In **Table** 4.1 we have collected the ρ_{xx}-values at 280 K and 4 K and the activation energy Δ for a number of samples. The data in this table represent the summary of 35 individual measurements, 15 of which were carried out on the $x = 0.54$ and $y = 1.3$ composition. The resistivity values at $T = 4$ K all exceed 5 Ωcm. We remark that in our first series of crystals with a fixed value $y = 1.3$ the sample with $x = 0.54$ has a record-high ρ_{xx}-value of 12.6 Ωcm at $T = 4$ K, and the largest value $\Delta = 102$ meV as well. Subsequent small changes of y in the range 1.2-1.6 did not yield a further increase of the low temperature resistivity.

Table 4.1: *Transport parameters obtained from resistivity and Hall effect measurements of BSTS crystals with composition as given in the first column: $\rho_{xx}(280\ K)$, $\rho_{xx}(4\ K)$, activation energy Δ estimated from the linear part in $\ln \rho_{xx}$ vs. $1/T$, the low-field Hall coefficient $R_H(200\ K)$ and $R_H(4\ K)$, the bulk carrier density n_b and the transport mobility μ calculated in a single band model.*

Composition $Bi_{2-x}Sb_xTe_{3-y}Se_y$	ρ_{xx}(280 K) (mΩcm)	ρ_{xx}(4 K) (Ωcm)	Δ (meV)	R_H(200 K) (cm^3/C)	R_H(4 K) (cm^3/C)	n_b(4 K) (10^{16} cm^{-3})	μ(4 K) (cm^2/Vs)
$x = 0.58$; $y = 1.3$	50.5	10.4	44	—	-468	1.3	45
$x = 0.54$; $y = 1.3$	53.6	12.6	102	30	-3110	0.2	247
$x = 0.50$; $y = 1.3$	141	7.1	56	27	380	1.6	54
$x = 0.48$; $y = 1.3$	81.9	5.5	48	20	-167	3.7	30
$x = 0.46$; $y = 1.3$	36.6	5.0	72	31	1657	0.4	331
$x = 0.42$; $y = 1.3$	44.4	6.8	36	4	6	107	0.9
$x = 0.54$; $y = 1.6$	133	8.6	83	-92	-707	0.9	82
$x = 0.54$; $y = 1.5$	214	8.9	66	37	-278	2.2	31
$x = 0.54$; $y = 1.2$	—	12.1	48	8	-1940	0.3	160

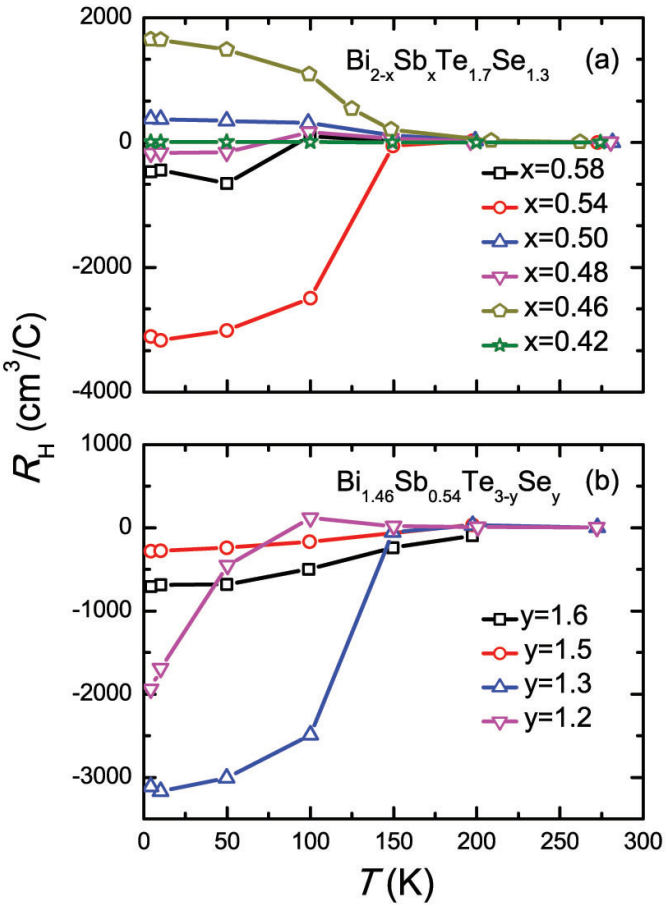

Figure 4.3: *Temperature dependence of the low-field Hall coefficient R_H of BSTS crystals with (a) $y = 1.3$ and x-values as indicated, and (b) $x = 0.54$ and y-values as indicated.*

Given these resistivity data, Hall experiments are of interest to examine the character and quantity of bulk carriers in these samples. The temperature variation of the low-field Hall coefficient $R_{\rm H}(T)$ for the two series of crystals with fixed $y = 1.3$ and fixed $x = 0.54$ is shown in **Figure** 4.3(a) and (b), respectively. The Hall coefficients were obtained by fitting the linear Hall resistivity for $B \leq 1$ T. For the first series (**Figure** 4.3(a)), $R_{\rm H}$ of all samples is positive at temperatures above 200 K and the values gradually increase upon lowering the temperature. Near 150 K, *i.e.* near the temperature where the resistivity starts to rise quickly, the absolute value of the Hall coefficient increases rapidly. For an increasing Sb content with respect to $x \approx 0.5$, $R_{\rm H}$ turns negative, whereas for a decreasing Sb content $R_{\rm H}$ remains positive. For the second series of samples (**Figure** 4.3(b)) $R_{\rm H}$ of all samples starts positive near room temperature, but eventually attains fairly large negative values near 4 K.

The carrier type and concentration in BSTS and related compounds is in general connected to the competition between two effects: (*i*) (Bi,Sb)/Te antisite defects which act as electron acceptors (or hole dopants), and (*ii*) Se vacancies which act as electron donors. This tells us that in the high temperature regime where $R_{\rm H} > 0$ (Bi,Sb)/Te antisite defects are dominant in providing carriers. However, at low temperatures $R_{\rm H} < 0$ and Se vacancies prevail, except for the crystals with a reduced Sb content ($x < 0.5$). $R_{\rm H}$-values at 200 K and 4 K are listed in **Table** 4.1. In order to compare the transport parameters with values reported in the literature we have listed the bulk carrier density, $n_{\rm b}$, and mobility $\mu = 1/ne\rho_{\rm xx}$ as well, assuming a simple single band model. Clearly, in these data, the crystal with the composition $Bi_{1.46}Sb_{0.54}Te_{1.7}Se_{1.3}$ stands out as the one with the highest resistivity, the largest activation gap and the lowest carrier concentration $n_b = 0.2 \times 10^{16}$ cm^{-3}.

We grew three batches of single crystals of this composition and the measurement of 15 single crystals of $Bi_{1.46}Sb_{0.54}Te_{1.7}Se_{1.3}$ gave a reproducible picture that this composition generally gave the most bulk-insulating behaviour. There is some sample to sample variation in the transport parameters. For example, the low-T resistivity for the $x = 0.54$, $y = 1.3$ composition of 12.6 Ωcm given in **Table** 4.1 was representative, but values were also measured to be in the range of 11-15 Ωcm.

4.3.2 Thickness variation

A simple and elegant way to separate the contribution from the surface and the bulk to the total conductivity of a topological insulator is by reducing the sample thickness, t [30, 115, 141, 142]. In **Figure** 4.4(a) we show the resistivity $\rho(T)$ of a $Bi_{1.46}Sb_{0.54}Te_{1.4}Se_{1.6}$ crystal with $t = 140$ μm that subsequently was thinned down in 12 steps to 6 μm. Here $\rho = (A/l) \times R$ where $A = t \times w$ is the cross sectional area for the current (w is the sample width) and l the distance between the voltage contacts. The overall behavior $\rho(T)$ for all

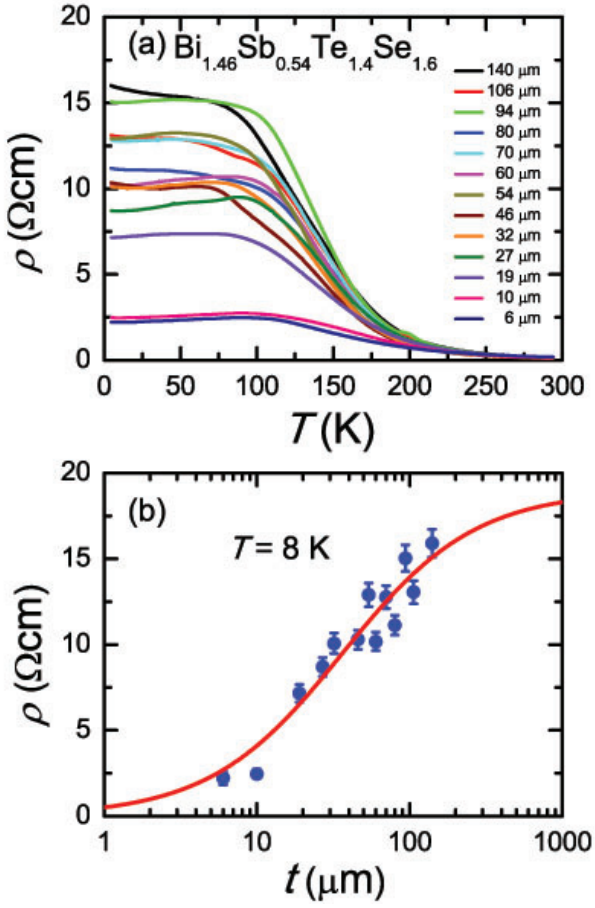

Figure 4.4: *(a) Temperature dependence of the resistivity of a $Bi_{1.46}Sb_{0.54}Te_{1.4}Se_{1.6}$ crystal with thickness $t = 140$ μm thinned down in 12 steps to 6 μm as indicated. (b) Measured resistivity at 8 K as a function of thickness (solid dots). The solid line represent a fit of the data to the parallel resistor model (see text).*

thicknesses is similar to the results presented in **Figure** 4.1. However, while the curves almost overlap at high temperatures, the ρ-value at low temperatures decreases significantly when reducing the sample thickness. This tells us the ratio between the surface and bulk contribution changes with thickness.

For a proper analysis the parallel resistor model is used:

$$\rho = \frac{\rho_b \rho_s (t_b + 2t_s)}{2t_s \rho_b + t_b \rho_s} \tag{4.1}$$

where ρ_b and ρ_s are the resistivities, and t_b and t_s the thicknesses, of the bulk and the surface layer [29], respectively. For t_s we may take 3 nm which is the thickness of 1 unit cell. The factor 2 in the **Equation** 4.1 above counts the top *and* the bottom surface of the sample. In **Figure** 4.4(b) we have traced ρ taken at 8 K as a function of $t \cong t_b$. The uncertainty in the ρ-values is mainly due to the error in the geometrical factor, especially in the value of l ($\pm 5\%$) because of the finite size of the silver paint contacts. The solid line represents a least square fit to **Equation** 4.1 with fit parameters $\rho_b = 19.0\ \Omega$cm and $\rho_s = 3.14 \times 10^{-3}\ \Omega$cm, or expressed as conductivities $\sigma_b = 0.053\ \Omega^{-1}\text{cm}^{-1}$ and $\sigma_s = 318\ \Omega^{-1}\text{cm}^{-1}$. Consequently,

the surface conductance $G_s = 2 \times t_s \times \sigma_s = 1.91 \times 10^{-4}\ \Omega^{-1}$. We remark our value for σ_b compares favorably to (is smaller than) the values 0.1 Ω^{-1}cm^{-1} and 0.12 Ω^{-1}cm^{-1} for sample compositions $Bi_{1.5}Sb_{0.5}Te_{1.7}Se_{1.3}$ and $Bi_{1.5}Sb_{0.5}Te_{1.8}Se_{1.2}$ reported in [30] and [115], respectively. The ratio of the surface conductance over the total sample conductance can be calculated as $G_s/(G_s + t\sigma_b)$. With our fit parameters we calculate for samples with a thickness of 100, 10 and 1 μm a surface contribution of 27 %, 78 % and 97 %, respectively. For a nanoflake with typical thickness of 130 nm (see the next subsection), we obtain a value of 99.6 %. We conclude surface-dominated transport can be achieved in our BSTS crystals grown with a global composition $Bi_{1.46}Sb_{0.54}Te_{1.4}Se_{1.6}$ when the sample thickness is less than ~ 1 μm.

4.3.3 Weak antilocalization

The thickness dependence of the resistivity shows dominance of surface transport for thin samples. A further test as to whether the surface dominated transport is consistent with the presence of topological surface conduction channels is to search for and characterise possible signals of weak antilocalization. For our study of weak antilocalization we selected the BSTS composition we found to give crystals with the highest bulk resistivity: $Bi_{1.46}Sb_{0.54}Te_{1.7}Se_{1.3}$. The magnetoresistance of an exfoliated nanoflake, structured by e-beam lithography into a Hall bar, was measured in the temperature range 2-40 K and in magnetic fields up to 2 T. The dimensions of the Hall bar are: thickness $t = 130 \pm 5$ nm, channel width $w = 2 \pm 0.02$ μm and distance between the voltage contacts $l = 6.75 \pm 0.25$ μm. The error in l takes into account the extended size of the voltage electrodes. The temperature variation of the resistivity $\rho(T)$ of the Hall bar is shown in the inset of **Figure** 4.5(b). For this thickness the resistivity at low temperatures levels off at a low value of $0.035\ \Omega$cm, in good agreement with the functional behavior reported in **Figure** 4.4(b) for BSTS with a Se content $y = 1.6$. Since $\rho_b \gg \rho_s$ we obtain a sheet or surface conductance $G_s \approx t/\rho = 3.7 \times 10^{-4}\ \Omega^{-1}$.

In **Figure** 4.5(a) we show the resistance, R_{xx}, as a function of B, measured at $T = 2$ K. The relatively sharp increase of R_{xx} with field is ubiquitous in TIs [107, 143, 144] and is attributed to the suppression of 2D weak antilocalization, *i.e.* the constructive interference of time reversed scattering loops, generated by a magnetic field applied perpendicular to the sample surface, $B_\perp$. As the analysis of the magnetoresistance data we carry out below will show, the phase coherence length l_ϕ for the WAL in this system is of the same order as the flake thickness, justifying a double-check that the WAL behavior is indeed two-dimensional by recording the angular dependence of the WAL. In **Figure** 4.5(a), the magnetoresistance, $\Delta R \equiv R(B) - R(0)$ (we have dropped the subscript xx) is seen to be largest for B perpendicular to the sample surface ($\theta = 0°$). For an in-plane magnetic field ($\theta = 90°$) a small residual magnetoresistance is seen of unknown origin, but this has essentially

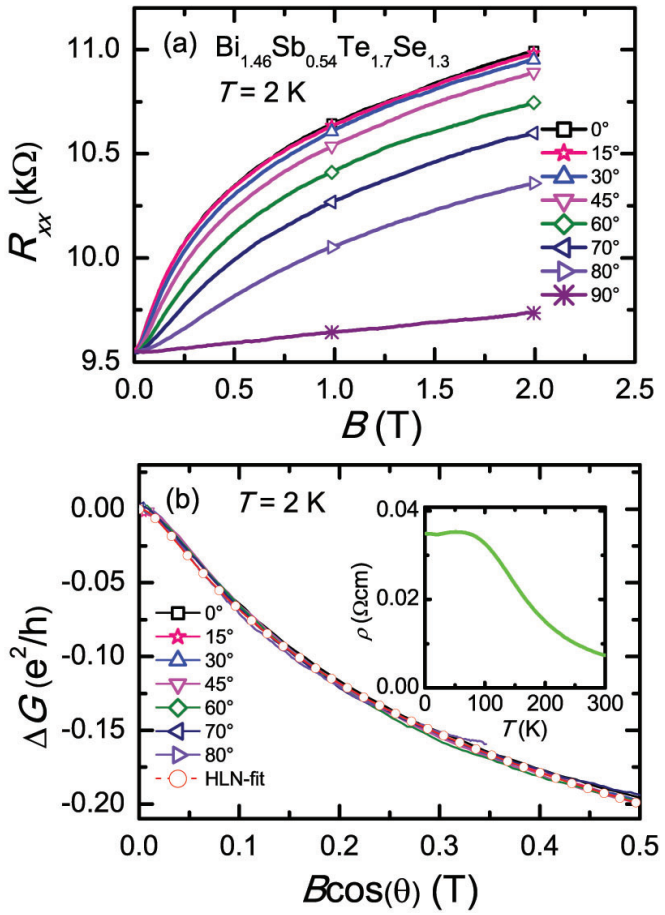

Figure 4.5: *(a) Longitudinal resistance R_{xx} of a BSTS Hall bar fabricated from a 130 nm thick flake measured at $T = 2$ K as a function of the magnetic field for different field angles as indicated. For $\theta = 0°$, B is directed perpendicular to the sample surface. (b) Magnetoconductance ΔG at $T = 2$ K plotted as a function of $B\cos\theta$, where θ is the angle between the surface normal and B. The data collapse onto an universal curve, which confirms the 2D nature of WAL. The open circles represent a fit to the HLN expression (**Equation** 4.2) in the field range $B_\perp = 0 - 0.5$ T. The fit parameters are $l_\phi = 116$ nm and $\alpha = -1.14$. Inset: ρ_{xx} of the BSTS Hall bar as a function of temperature.*

no effect on the parameters coming out of the fits to the data presented and discussed in the following. In **Figure** 4.5(b) we trace the magnetoconductance $\Delta G_{2D}(B,\theta) \equiv G(B,\theta) - G(B,\theta = 90°)$ for $0° \leq \theta \leq 80°$ as a function of $B\cos\theta$. Obviously, the data collapse onto an universal curve, which signals the two dimensional character of the WAL in these samples.

Next we compare the universal curve with the expression for the magnetoconductivity $\Delta\sigma_{2D}$ of 2D weak antilocalization put forward by Hikami, Larkin and Nagaoka (HLN) [109]:

$$\Delta\sigma_{2D} = -\frac{\alpha e^2}{2\pi^2\hbar}\left(\ln\left(\frac{\hbar}{4el_\phi^2 B}\right) - \psi\left(\frac{1}{2} + \frac{\hbar}{4el_\phi^2 B}\right)\right) \tag{4.2}$$

Here ψ is the digamma function, l_ϕ is the effective phase coherence length and α is a

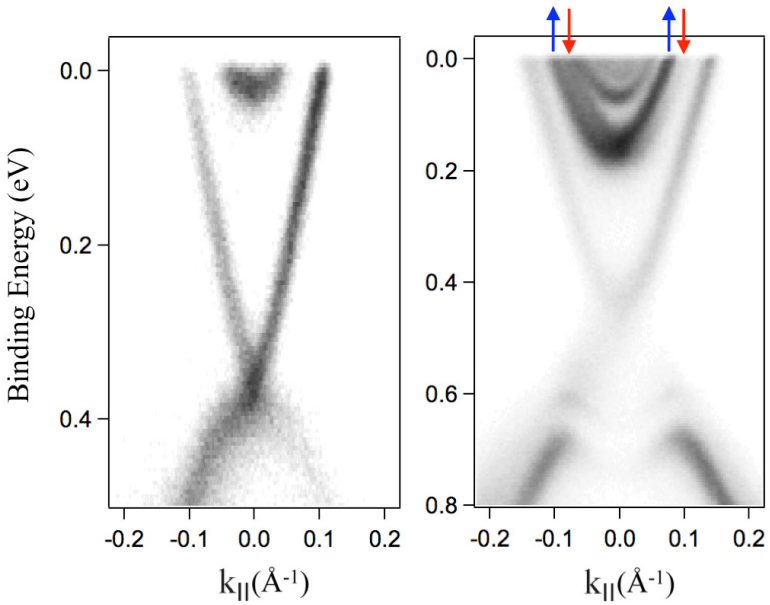

Figure 4.6: *ARPES data recorded from the surfaces of $Bi_{1.46}Sb_{0.54}Te_{1.7}Se_{1.3}$ (left) and Bi_2Se_3 (right) under conditions of saturated downward band bending due to adsorption of residual gas atoms on the surface. The data cut through the center of the surface Brillouin zone were measured using photon energies of 27 eV (BSTS) and 30 eV (Bi_2Se_3) at a temperature of 17 K. The arrows in the right panel denote the spin polarization of the Rashba-type surface states observed on band-bent Bi_2Se_3. Notice the different energy scales of the two panels*

Table 4.2: *Phase coherence length l_ϕ and prefactor α, obtained by fitting the 2D magneto-conductance of BSTS crystals to the HLN expression, **Equation** 4.2. $B_{\perp,\max}$ gives the field range for the fit (see text).*

Composition $Bi_{2-x}Sb_xTe_{3-y}Se_y$	Thickness (nm)	$B_{\perp,\max}$ (T)	l_ϕ (nm)	α	Temperature (K)	Reference
$x = 0.54$; $y = 1.3$	130	0.5	116	-1.14	2	this work
$x = 0.54$; $y = 1.3$	130	0.5	52	-0.93	40	this work
$x = 0.5$; $y = 1.3$	200	0.5	121	-0.96	2	[114]
$x = 0.5$; $y = 1.2$	596	0.5	160	-0.75	2	[115]
$x = 0.5$; $y = 1.3$	85	6	170	-1.3	4	[145]

prefactor. Each scattering channel from a band that carries a π Berry phase contributes a value $\alpha = -1/2$ [107]. For independent bottom and top topological surface channels we therefore expect $\alpha = -1$. In **Equation** 4.2, $\Delta\sigma_{2D} = \frac{l}{w}\Delta G_{2D}$, where $\frac{l}{w} = 3.38 \pm 0.13$. We have fitted the collapsed magnetoconductance data at $T = 2$ K to the HLN expression with l_ϕ and α as fit parameters. In the field interval $B\cos\theta = 0 - 0.5$ T we find $l_\phi = 116$ nm and $\alpha = -1.14 \pm 0.06$. For this value of l_ϕ we calculate $B_\phi = \hbar/4el_\phi^2 = 0.012$ T and the condition $B \gg B_\phi$ is easily met, *i.e.* the applied field is sufficiently large to suppress WAL. Furthermore, $l_\phi \ll w$ which ensures our Hall bar has the proper dimensions for 2D WAL. If we extend the field range of the fit, the value of α decreases slightly, but at the same time the quality of the fit decreases. For instance, by fitting up to 2 T we obtain $\alpha = -0.96 \pm 0.06$.

The temperature variation of the field-induced suppression of WAL has been investigated at $T = 2, 4, 10, 15, 25$ and 40 K. By increasing the temperature the WAL becomes weaker and is suppressed more easily by the magnetic field. By fitting our collapsed $\Delta G_{2\mathrm{D}}(B_\perp)$ curves, l_ϕ decreases to 52 nm at $T = 40$ K. A power-law fit yields $l_\phi \propto T^{-0.46}$ in the temperature range 10-40 K, which is close to the expected behavior $T^{-0.5}$ for 2D WAL. However, below 10 K l_ϕ levels off and the exponent drops to -0.06. The prefactor α decreases slightly to -0.93 ± 0.05 at 40 K for a fit range $0 - 0.5$ T.

4.4 Discussion

Single crystals of $Bi_{2-x}Sb_xTe_{3-y}Se_y$ with x and y around 0.5 and 1.3 can nowadays clearly be considered to have superior bulk insulating properties [29,30,114,115,145] amongst the 3D topological insulators. This makes BSTS particularly attractive for exploratory research into TI devices with functionalities based on protected surface transport. In this paper we have shown that by fine tuning the BSTS composition it is possible to obtain record high values of the resistivity. For a global composition of $Bi_{1.46}Sb_{0.54}Te_{1.7}Se_{1.3}$ low-T resistivity values exceeding $10\ \Omega$cm were common for samples with a thickness of 100 μm. At the same time Hall data show the bulk carrier concentration in these samples can be as low as 0.2×10^{16} cm^{-3} at $T = 4$ K. The strong bulk insulating behavior is furthermore demonstrated by the large value of the activation gap for transport, $\Delta \simeq 100$ meV. The data of **Table** 4.1 show there to be a non-trivial dependence of the transport characteristics on the x and y-values chosen for each single crystal batch. Our sample characterization shows that this is clearly not a consequence of random compositional irreproducibility from sample to sample. Rather, the chemistry controlling the defect density and balance (between p- and n-type) in these low-carrier concentration 3D TI materials is a subtle quantity, and not one that simply tracks the Bi/Sb and Te/Se ratios in a linear fashion. This makes a variation of composition necessary to determine the best route to the most bulk insulating behaviour. This was done in Ref. [29] and is also the approach adopted here,

resulting in excellent bulk-insulating characteristics.

Because of the genuine bulk insulating behavior of the optimized BSTS crystals, the ρ-values obtained at low temperatures are not true resistivity values but depend on the thickness when $t \leq 1$ mm (see **Figure** 4.4). Therefore the transport data result from parallel channels due to the bulk and top/bottom surfaces. Our analysis with the parallel resistor model of the resistance measured on the very same BSTS crystal made thinner and thinner shows that the surface contribution to the total transport is close to 97 % for a thickness of 1 μm. Hence we conclude that devices fabricated with submicrometer thickness are sufficiently bulk insulating to exploit the topological surface states by transport techniques. The nanoflake with a thickness of 130 nm certainly fulfills this condition.

The HLN fit of the magnetoconductance of the thin flake yields values of α close to -1, which is in keeping with the thickness dependence of the resistivity shown in **Figure** 4.4 in that for a flake of this thickness essentially all of the transport occurs through the surface states. The α value of close to -1 would suggest that it is the topological surface states at the top and bottom of the crystal which are dominating the transport. In **Table** 4.2 we have collected the fit parameters l_ϕ and α, as well as those obtained for BSTS nanoflakes reported in the recent literature. Hsiung *et al.* [114] measured a flake with enhanced surface mobility and reported an α-value close to -1 as well. The α-values reported by Xia *et al.* [115] obtained on a relatively thick nanoflake are systematically smaller than -1. Lee *et al.* [145] found a significantly larger value $\alpha = -1.3$ for a gated nanoflake at zero bias. Here the large value of α is attributed to the combined presence of non-trivial and Rashba-split conduction channels in the topologically trivial 2DEG caused by band bending.

The existence (or not) of Rashba spin-split states at the surface of BSTS is of importance for the magnetoconductance – and in particular – the WAL behaviour. The alpha value we extract for BSTS of close to -1 (**Table** 4.2) suggests there is not a contribution from Rashba spin-split states in our BSTS crystals. In Bi_2Se_3 it is well established from ARPES that topologically trivial, confined bulk states can form a 2DEG in the near surface region and that these states can also show Rashba-type spin splitting [139, 140]. Thus, in **Figure** 4.6 we show two ARPES images of the portion of k-space near the Gamma-point: one for Bi_2Se_3 and one for a BSTS crystal from the same source and of the same composition as the flake used for the WAL studies. In both cases, we show ARPES data from surfaces after significant exposure to adsorbates - *i.e.* for the case of essentially maximal band-bending. The Bi_2Se_3 data show clear signs of confinement of states related to both the conduction and valence bands, as well as of emerging Rashba-type spin splitting for the states crossing the Fermi level, in accordance with the literature [139, 140]. The left panel of **Figure** 4.6 shows analogous data for adsorbate exposed BSTS. The downward band bending has led to the population of states derived from the bulk conduction band, but there is clearly no Rashba-type spin splitting at the BSTS surface. This is fully consistent with the alpha

value close to -1 extracted from the analysis of the WAL data shown in **Figure** 4.5 and **Table** 4.2.

4.5 Summary

We have presented an extensive study of the bulk-insulating properties of BSTS single crystals. We have synthesized numerous $Bi_{2-x}Sb_xTe_{3-y}Se_y$ single crystals with compositions around $x = 0.5$ and $y = 1.3$, with steps in x of 0.02 and y of 0.1. The samples were investigated by resistance and Hall effect measurements. We show that via variation of the composition on a fine level, we could arrive at a record-high resistivity, bulk-insulating transport behaviour and a low carrier density, *e.g.* for multiple growth runs for the composition $Bi_{1.46}Sb_{0.54}Te_{1.7}Se_{1.3}$. Because of the genuine bulk insulating behavior of these optimized BSTS crystals, the ρ-values obtained at low temperatures are not true resistivity values but depend on the thickness when $t \leq 1$ mm. An analysis of the resistance vs. thickness within a parallel resistor model of the resistance measured for crystals with different thicknesses shows that the surface contribution to the electrical transport amounts to 97 % when the sample thickness is reduced to 1 μm. Hence we conclude that devices fabricated with submicrometer thickness are sufficiently bulk insulating to exploit the topological surface states by transport techniques. This conclusion is supported by the observed collapse of the magnetoconductance data of an exfoliated BSTS nanoflake as a function of the perpendicular magnetic field component, further confirming 2D transport. The analysis within the HLN model for 2D weak antilocalization shows the fit parameter $\alpha \simeq -1$ as expected for conduction via a pair of topological surface states. Both this fact and our ARPES data recorded under band-bent conditions show a lack of Rashba-split non-topological surface states in our $Bi_{1.46}Sb_{0.54}Te_{1.7}Se_{1.3}$ crystals.

Chapter 5

Quantum oscillations of the topological surface states in low carrier concentration crystals of $Bi_{2-x}Sb_xTe_{3-y}Se_y$

We report a high-field magnetotransport study on selected low-carrier crystals of the topological insulator $Bi_{2-x}Sb_xTe_{3-y}Se_y$. Monochromatic Shubnikov - de Haas (SdH) oscillations are observed at 4.2 K and their two-dimensional nature is confirmed by tilting the magnetic field with respect to the sample surface. With help of Lifshitz-Kosevich theory, important transport parameters of the surface states are obtained, including the carrier density, cyclotron mass and mobility. For $(x, y) = (0.50, 1.3)$ the Landau level plot is analyzed in terms of a model based on a topological surface state in the presence of a non-ideal linear dispersion relation and a Zeeman term with $g_s = 70$ or -54. Input parameters were taken from the electronic dispersion relation measured directly by angle resolved photoemission spectroscopy on crystals from the same batch. The Hall resistivity of the same crystal (thickness of 40 μm) is analyzed in a two-band model, from which we conclude that the ratio of the surface conductance to the total conductance amounts to 32 %.

5.1 Introduction

Topological insulators (TIs) in three dimensions (3D) attract much attention as versatile platforms to study new forms of quantum matter [146]. TIs are bulk insulators with a non-trivial topology of the electronic bands that gives rise to metallic states at the surface [1, 3]. The gapless surface states host a wealth of new physics, because they have a Dirac-type energy dispersion and the spin is locked to the momentum. As a result, they are immune to backscattering due to disorder, provided that time reversal symmetry is preserved. This makes TIs promising materials for applications in fields like spintronics and magnetoelectronics [1, 3]. At the same time, TIs offer an almost unlimited source of test-case materials for new theoretical ideas and concepts, like the quantum spin Hall effect [147], Majorana physics [148] and quantum computation [129].

Probably the best studied TI family consists of the layered compounds Bi_2Te_3, Bi_2Se_3, Sb_2Te_3, etc. The prediction that these materials are 3D TIs with a single Dirac cone on the surface [16], was promptly verified in experiments by the surface sensitive technique of angle-resolved photoemission spectroscopy (ARPES) [17, 19, 130]. However, the interior (bulk) of these workhorse TI materials is in general not a genuine insulator, because of the presence of charge carriers induced by impurities and defect chemistry. This seriously hampers the study of topological surface states in transport experiments, as well as potential device applications based on spin and charge transport. In order to solve this problem several research directions have been pursued, among which charge carrier doping [99, 149], thin film engineering and electrostatic gating [131, 132]. Yet another route was promoted by Ren *et al.* [29], namely to approach the intrinsic topological insulator regime by optimizing the $Bi_{2-x}Sb_xTe_{3-y}Se_y$ (in short BSTS) composition. The composition around (x, y)=(0.50,1.3) was found to be the optimum for bulk insulating behavior, as evidenced by a resistivity of several Ωcm at liquid helium temperatures and a bulk carrier concentration of $\sim 2 \times 10^{16}$ cm^{-3}. The appealing topological properties of BSTS, notably a tunable Dirac cone, were furthermore demonstrated by ARPES [135], STM and STS [137] and THz Time Domain Spectroscopy [136]. We remark that recently also stoichiometric $BiSbTeSe_2$ has become an attractive material to investigate topological surface states [54, 150, 151].

Recently we reported an extensive magnetotransport study that aimed at the further investigation of the bulk-insulating properties of BSTS [152]. Single crystals with composition $Bi_{1.46}Sb_{0.54}Te_{1.7}Se_{1.3}$ produced the highest resistivity (12.6 Ωcm) and lowest bulk carrier density (0.2×10^{16} cm^{-3}) at low temperatures. The contribution from the bulk and surface channels to the total resistance can be disentangled by employing a parallel resistor model. For a sample with a typical thickness of 100 μm, the ratio of the surface conductance over the total conductance is about 27 %. Upon further reducing the sample thickness, this ratio increases and it can be as large as 97 % for a 1 μm thick sample [152].

The magnetoconductance of BSTS nanoflakes, prepared around the optimum composition, showed 2D weak antilocalization with an amplitude $\alpha \simeq -1$, as expected for transport dominated by topological surface states [152].

In this paper we report a high-magnetic field transport study on selected, optimized BSTS crystals, which enabled us to probe the surface states by quantum oscillations in the resistance, via the Shubnikov - de Haas (SdH) effect. The SdH effect is a powerful tool to discriminate between 2D and 3D Fermi surfaces [117]. At the same time, it may give direct access to the topological nature of the surface states via the geometric phase (Berry phase) [153, 154] of the quantum oscillations. Therefore, the SdH effect in TIs has received ample attention in the literature, notably through experiments carried out on bulk crystals of Bi_2Te_3, Bi_2Se_3 and Bi_2Te_2Se [27, 28, 99, 149, 155]. In addition, the SdH effect was reported for non-stochiometric BSTS (x, y)=(0.50,1.3) bulk crystals [30] and nanoflakes [114]. In most cases, the phase offset of the quantum oscillations obtained from a linear Landau level plot has been interpreted as a finite Berry phase. However, such an interpretation is not straight-forward because of the non-ideal Dirac dispersion and the sizeable Zeeman effect due to the large g_s-factor [153, 154]. Therefore, care should be taken when using the phase offset of the SdH oscillations as direct evidence for topological surface states.

Here we present SdH data for BSTS crystals with compositions $Bi_{1.5}Sb_{0.5}Te_{1.7}Se_{1.3}$ and $Bi_{1.46}Sb_{0.54}Te_{1.7}Se_{1.3}$. The SdH oscillations are monochromatic and their field-angular variation demonstrates their 2D nature. The standard analysis using Lifshitz-Kosevich theory gives a 2D carrier density of 1.5 and 0.8×10^{12} cm^{-2}, and a cyclotron mass of 0.18 and $0.10m_e$, respectively. For (x, y)=(0.50,1.3) the Landau level plot is analyzed in terms of a topological surface state with help of the non-linear dispersion relation measured directly by ARPES, and a Zeeman term with $g_s = 70$ or -54. In addition, we show that the Hall resistivity of the same crystal (of thickness 40 μm) can be analyzed successfully in a two-band model, from which a surface contribution to the total conductance of 32 % is arrived at.

5.2 Experimental

The BSTS single crystals used for the SdH measurements were taken from the same batch that was prepared for the magnetotransport study reported in Ref. [152]. Here we focus on crystals around the optimum composition, *i.e.* with $(x, y) = (0.50, 1.3)$ and $(x, y) = (0.54, 1.3)$, whereby the x- and y-values refer to nominal concentrations. For details of the single crystal growth procedure and characterization of the crystals by magnetotransport we refer to Ref. [152]. Flat rectangular samples were cut from the single-crystalline boule using a scalpel blade. Next the samples were cleaved in the ab-plane of the rhombohedral structure, at both top and bottom sides, using Scotch tape so as to

obtain a thickness of around 50 μm. The longitudinal, R_{xx}, and Hall resistance, R_{xy}, were measured in a six-probe configuration. Current and voltage contacts were made by attaching thin (40 μm) copper wires to the crystals with silver paste. The exposure time to air between cleaving and mounting the samples in the cryostat was kept to a minimum of about one hour.

High magnetic fields were produced with a Bitter magnet ($B_{max} = 33$ T) at the High Field Magnet Laboratory at the Radboud University in Nijmegen. The samples were mounted on the platform of a mechanical rotator that could be cooled down to 1.7 K. The resistance was measured using a low frequency ac-technique with a SR830 DSP lock-in amplifier. The excitation current, I, flows in an arbitrary direction in the ab-plane and was typically 10 μA. Measurements were conducted for two polarities of the magnetic field, after which the longitudinal and Hall resistance were extracted by symmetrization. The field-sweep rate amounted to 30 mT/s. By rotating the sample platform, the angular variation of the SdH oscillations was determined. The magnetoresistance was always measured in the transverse configuration ($B \perp I$), since the rotation axis coincides with the direction of I.

ARPES measurements were performed at the SIS-HRPES endstation of the Swiss Light Source using a ScientaR4000 hemispherical electron analyzer. The data presented in this work were acquired at 16 K using 27 eV photons with linear horizontal polarization. The samples were cleaved and measured at a pressure better than 5×10^{-11} mbar and the Fermi level position was determined using in-situ evaporated Au thin films that were in direct contact with the sample holder.

5.3 Results and Analysis

5.3.1 Shubnikov - de Haas effect

We have measured the magnetoresistance of 10 different BSTS crystals in magnetic fields up to 30 T, applied along the rhombohedral axis (c-axis) at 4.2 K. In **Figure** 5.1(a) we show the longitudinal resistance R_{xx} of BSTS crystals with $(x, y) = (0.50, 1.3)$ and $(x, y) = (0.54, 1.3)$ as a function of the magnetic field at $T = 4.2$ K and $\theta = 0°$. After the initial sharp rise connected to the suppression of the weak antilocalization (WAL) in low fields [152], the magnetoresistance increases in a quasi-linear manner without saturation. Selected crystals showed a clear SdH effect. These were further investigated to determine the temperature and angular variation of the SdH oscillations. While the magnetoresistance, $MR(B) = (R(B) - R(0))/R(0)$, typically has a magnitude of 100 % near 30 T, the amplitude of the SdH signal is small and amounts to only 1 % of the total resistance. After subtracting the smooth monotonic background contribution from R_{xx} we obtain the SdH signal shown in **Figure** 5.1(b) and (c). Here we trace ΔR_{xx} *versus* $1/B$,

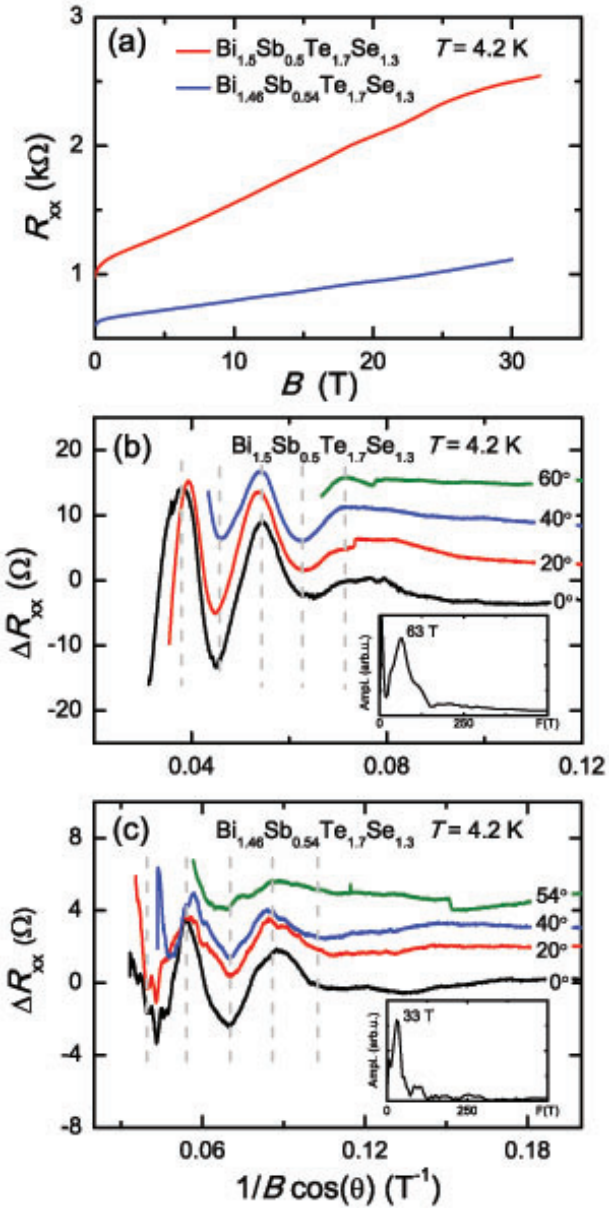

Figure 5.1: *Panel (a): Longitudinal resistance R_{xx} of BSTS crystals with $(x, y) = (0.50, 1.3)$ and $(x, y) = (0.54, 1.3)$ as a function of the magnetic field at $T = 4.2$ K and $\theta = 0°$. Panel (b) and (c): Oscillatory component of the longitudinal resistance ΔR_{xx} plotted versus $1/(B\cos\theta)$ for BSTS crystals with $(x, y) = (0.50, 1.3)$ and $(x, y) = (0.54, 1.3)$, respectively, at $T = 4.2$ K. Here θ is the angle between the field and the normal to the sample surface (c-axis) and $B\cos\theta$ is the perpendicular component of the applied magnetic field. Curves for $\theta \neq 0$ are offset for clarity. The positions of the minima and maxima of the SdH oscillations, marked by the vertical dashed lines, depend solely on $1/B\cos\theta$, which points to the 2D nature of the Fermi surface. The insets show the fast Fourier transform of the data at $\theta = 0°$.*

in order to reveal the characteristic quantum oscillation period, where ΔR_{xx} refers to the difference between the oscillatory resistance in field and the smooth background. The data with the field perpendicular to the sample surface ($B \parallel c$-axis, $\theta = 0°$) are given by the solid black lines. The angular variation of the SdH effect measured for angles $\theta \leq 60°$ provides strong evidence the oscillations can be attributed to a 2D Fermi surface, since the positions of the minima and maxima at different θ coincide in the plots of ΔR_{xx} versus $1/(B\cos\theta)$ as indicated by the vertical grey dashed lines in **Figure** 5.1(b),(c). Here θ is defined as the angle between the field direction and the crystallographic c-axis. We remark that, strictly speaking, a 3D spheroidal Fermi surface (*i.e.* an ellipsoid of revolution) with an aspect ratio such that the longer axis is along the reciprocal lattice vector $2\pi/c$ could also be in agreement with the angular variation of the SdH data. However, this possibility can safely be excluded since the calculated 3D carrier density, n_{3D}, is at variance with the measured Hall data (see below). The fast Fourier transforms of the data at $\theta = 0°$ give the SdH frequencies F of 63±3 T and 33±3 T for $(x, y) = (0.50, 1.3)$, and $(x, y) = (0.54, 1.3)$, respectively. See the insets in **Figure** 5.1(b) and (c). According to the Onsager relation, the extremal cross section of the Fermi surface, $A_k(E_F)$, is proportional to the frequency, F, via the relation $A_k(E_F) = (2\pi e/\hbar) \times F$, where $\hbar$ and e are Planck's constant divided by 2π and the electron charge, respectively. Assuming a circular cross section of the Fermi surface $A_k(E_F) = \pi k_F^2$ the corresponding values for the Fermi wave numbers can be calculated for the two crystals, and come out at k_F = 4.4 $\times 10^6$ cm^{-1} and 3.2 $\times 10^6$ cm^{-1}, respectively. Next the 2D carrier density n_{2D} can be calculated from the non-spin degenerate relation $n_{2D} = k_F^2/4\pi$ = 1.5 $\times 10^{12}$ cm^{-2} and 0.81 $\times 10^{12}$ cm^{-2}, respectively. For a spheroidal Fermi surface with an aspect ratio of 2 these values of k_F would result in a bulk carrier density $n_{3D} = (1/2) \times (2k_F)^3/(3\pi^2)$ of $\sim 10^{19}$ cm^{-3} assuming no spin degeneracy. This value exceeds the bulk carrier concentration calculated from the Hall data [152] by a factor of 1000.

In order to obtain important information about the transport parameters of the 2D carriers we have measured the temperature variation of the SdH effect for $(x, y) = (0.50, 1.3)$ and $(x, y) = (0.54, 1.3)$. See **Figure** 5.2(a) and (b), respectively. From the thermal damping of the SdH oscillations one can deduce the cyclotron mass, m_c, while the amplitude of the SdH oscillations as a function of B allows one to determine the Dingle scattering time, τ_D. The SdH oscillations are analyzed with the standard Lifshitz-Kosevich (LK) expression for 2D charge carriers [156]:

$$\Delta R_{xx} \propto R_T R_D \cos[2\pi(\frac{F}{B} - \gamma)], \tag{5.1}$$

where the thermal damping factor $R_T = \frac{\alpha T}{B}/\sinh(\frac{\alpha T}{B})$ with $\alpha = 2\pi^2 k_B m_c/\hbar e$ and the Dingle damping factor $R_D = \exp(-\alpha T_D/B)$ with the Dingle temperature $T_D = \hbar/2\pi k_B \tau_D$. Here k_B is Boltzmann's constant and γ is the phase factor. Fits of the measured thermal damping to the LK expression are shown in **Figure** 5.2(c) and (d).

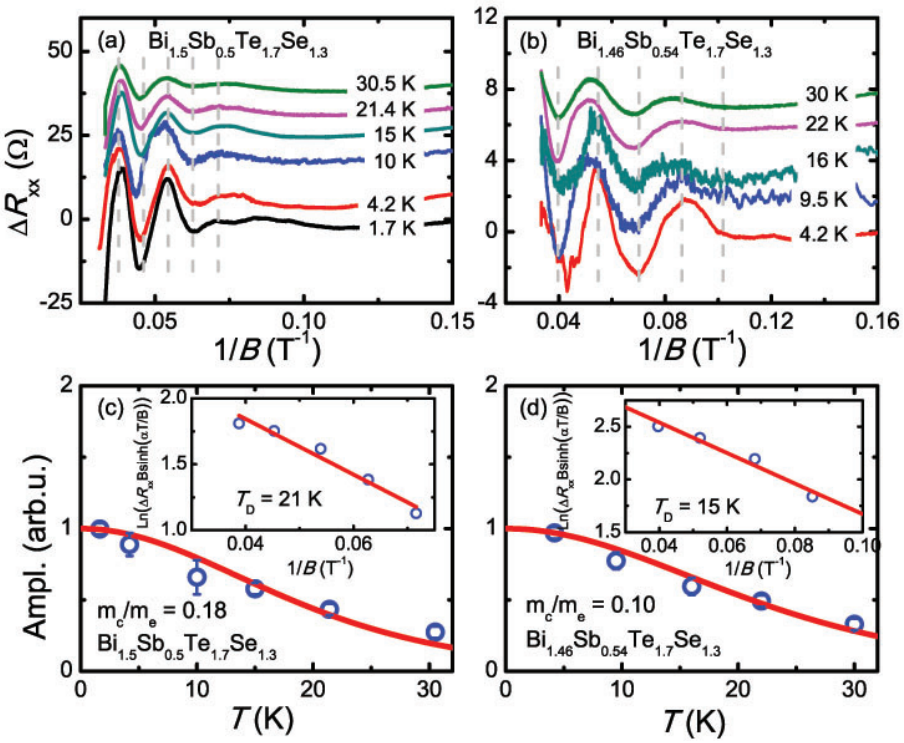

Figure 5.2: *Panel (a) and (b): Oscillatory component of the longitudinal resistance ΔR_{xx} plotted versus $1/B$ for BSTS crystals with $(x, y) = (0.50, 1.3)$, and $(x, y) = (0.54, 1.3)$, respectively, at temperatures in the range 1.7-30 K as indicated, and $\theta = 0°$. Curves are offset along the vertical axis for clarity. The vertical dashed lines mark the minima and maxima in ΔR_{xx}. Panel (c) and (d): Thermal damping of the SdH oscillations for $(x, y) = (0.50, 1.3)$ and $(x, y) = (0.54, 1.3)$, respectively. The cyclotron mass is $m_c = 0.18m_e$ and $0.10m_e$, respectively. The insets show the fit to the Dingle damping term at $T = 4.2$ K with the resulting Dingle temperature $T_D = 21$ K and 15 K, respectively.*

We extract a cyclotron mass m_c of $0.18m_e$ and $0.10m_e$ for $(x, y) = (0.50, 1.3)$ and $(x, y) = (0.54, 1.3)$, respectively, where m_e is the free electron mass. Combined with the values of k_F, derived above, the effective Fermi velocity $v_F^* \equiv \hbar k_F/m_c$ is calculated and equals 2.8 and 3.6×10^5 m/s, respectively. The analysis of the Dingle term is shown in the insets to **Figure** 5.2(c) and (d) and results in a T_D of 21 K and 15 K and a scattering time τ_D of 5.8×10^{-14} s and 8.4×10^{-14} s, for $(x, y) = (0.50, 1.3)$ and $(x, y) = (0.54, 1.3)$, respectively. By using these values of v_F^* and τ_D, the mean-free path of the surface carriers, ℓ_s^{SdH}, can be derived from the relation $\ell_s^{SdH} = v_F^*\tau_D$ and amounts to ∼16 nm and 30 nm, respectively. Finally, the corresponding surface mobility, $\mu_s^{SdH} = e\ell_s^{SdH}/\hbar k_F$ is calculated to be ∼560 and 1450 cm^2/Vs, respectively.

5.3.2 Landau level plot and Berry phase

Next, we extract and discuss the Berry phase of the quantum oscillations. The Berry phase $\phi_B = \pi(1 - 2\gamma)$ can be obtained from the phase factor γ in **Equation** 5.1 and

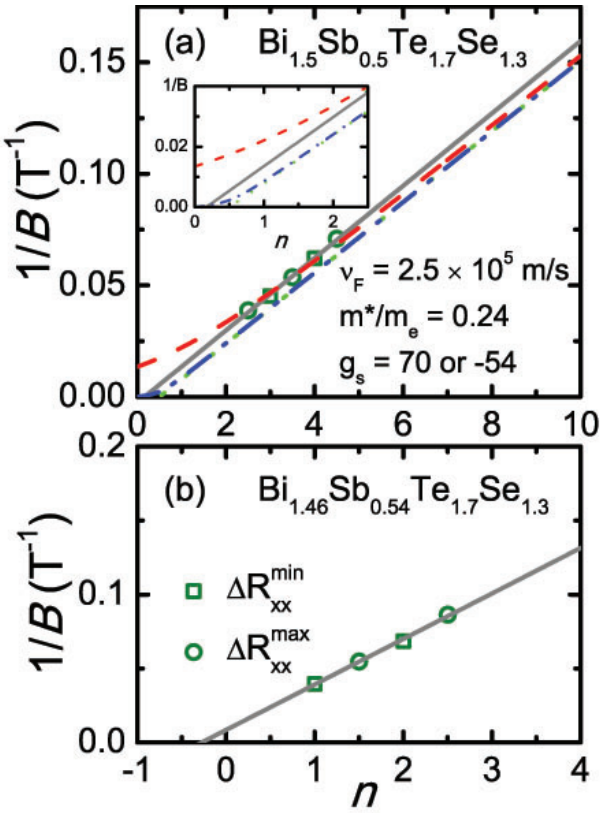

Figure 5.3: *Panel (a) and (b): Landau level plot of SdH oscillations in BSTS crystals with* $(x, y) = (0.50, 1.3)$*, and* $(x, y) = (0.54, 1.3)$*, respectively. Minima (green squares) and maxima (green circles) in* ΔR_{xx} *correspond to* n *and* $n + 1/2$*, respectively. In (a) and (b) the grey solid line represents a linear fit with* $n_x = 0.16$ *and* -0.28*, respectively. In (a) the blue dash-dotted line displays the case of a non-ideal linear dispersion with band parameters* $v_F = 2.5 \times 10^5$ *m/s and effective mass* $m^* = 0.24m_e$*; the red-dashed line includes the Zeeman term with* $g_s = 70$ *or* -54*; the green dotted-straight line shows the case of the ideal Dirac dispersion with* $F = 63$ *T. The inset presents a zoom of the LL plot near the origin. For* $(x, y) = (0.54, 1.3)$ *we did not make the full analysis based on* ***Equation*** *5.2, since we do not have access to precise values of* m^* *and* v_F*.*

is π for a linear energy dispersion ($\gamma = 0$) and zero for a parabolic energy dispersion ($\gamma = 1/2$) [157]. The standard procedure to extract the phase of the SdH oscillations makes use of a Landau level (LL) plot, in which the LL index n is plotted as a function of $1/B$. In the ideal case $n(1/B)$ is a linear function which extrapolates to $1/B = 0$ at the abscissa n_x, where $n_x = 1/2 - \gamma$. To construct the LL plot correctly, it is crucial to assign the index n to the correct position in $\Delta R_{xx}(B)$. In our case, for the surface states the Hall resistivity $\rho_{xy} > \rho_{xx}$, which means ΔR_{xx} has minima (maxima) at integer LL indices n ($n + 1/2$) [156]. The corresponding LL plots for $(x, y) = (0.50, 1.3)$ and $(x, y) = (0.54, 1.3)$ are shown in **Figure** 5.3(a) and (b), respectively. A linear least-squares fit (grey solid lines) yields $n_x = 0.16$ and $n_x = -0.28$, and a finite Berry phase $\phi_B = 0.32\pi$ and -0.56π, respectively. Clearly, these values differ from the value π expected for topological surface states.

A Berry phase extracted in this way that deviates from π has been reported frequently in other SdH studies on the 3D TI family $(Bi,Sb)_2(Te,Se)_3$ [27, 28, 99, 149, 158]. However, obtaining n_x by linear extrapolation is not justified in all cases. While it is appropriate for light-element materials, such as graphene [159], it is generally not suitable for 3D Bi-based TIs where deviations from the linear dispersion relation, $E(k)$, and the large Zeeman term should be taken into account [153, 154]. We first investigate the effect of a non-ideal-Dirac $E(k)$. The dispersion relation $E(k)$ for our $(x, y) = (0.50, 1.3)$ crystal was directly determined using ARPES. Data measured along the $\Gamma \rightarrow K$ and $\Gamma \rightarrow M$ high symmetry directions are shown in **Figure** 5.4. In order to fit the energy dispersion of the topological surface state as accurately as possible we need to maximize the number of data points in the occupied part of the energy spectrum. In this sense, the time-dependent energy shift to lower energies observed in BSTS [160, 161] and other Bi-based TIs [139, 162] is beneficial. We therefore chose to fit data acquired on a sample which has been maintained for 8 h in a background pressure in the mid 10^{-11} mbar range. The data are adequately described by the relation [30, 163]

$$E(k) = E_{DP} + v_F \hbar k + \frac{\hbar^2}{2m^*} k^2, \tag{5.2}$$

where v_F is the Fermi velocity at the Dirac point, m^* is the effective mass, and E_{DP} is the binding energy of the Dirac point. A least squares fit to **Equation** 5.2 gives $v_F = 2.0 \times 10^5$ m/s and $m^* = 0.24 m_e$ for $\Gamma \rightarrow K$ and $v_F = 3.0 \times 10^5$ m/s and $m^* = 0.25 m_e$ for $\Gamma \rightarrow M$. Since the anisotropy is small, we use in the analysis of the LL plot the average values $v_F = 2.5 \times 10^5$ m/s and $m^* = 0.24 m_e$. Following the procedure outlined in Ref. [153] these band parameters result in the calculated LL plot given by the dashed-dotted blue line in **Figure** 5.3(a). In the high-field regime a pronounced curvature towards $n_x = 0$ appears, and the LL plot deviates from the ideal linear dispersion relation (straight green dashed line) with $F = 63$ T. Clearly, adding the parabolic term in the energy dispersion cannot describe our data properly. Next we include the Zeeman term [153], *i.e.* the cyclotron energy $\frac{1}{2}\hbar\omega_c \rightarrow \frac{1}{2}\hbar\omega_c - \frac{1}{2} g_s \mu_B B$. With $g_s = 70$ or -54, the LL plot (dashed red line) fits our data well. Such large values of the g_s factor are in-line with those reported for other Bi-based TIs [153]. Our analysis shows that the linear extrapolation of $n(1/B)$ (solid grey line) does not yield a proper Berry phase. This is due to the large g_s factor and the non-ideal linear $E(k)$. We remark that for higher n-values the red and blue LL plots approach each other and coincide for $n > 10$. A linear extrapolation based on this section of the LL plot would yield the true Berry phase. However, to detect quantum oscillations in this regime would require mobilities as large as 2000 cm^2/Vs, which these heavily alloyed non-stoichiometric BSTS crystals prepared so far do not offer access to. We conclude that our analysis of the LL plot including the parabolic energy term and Zeeman term is in agreement with topological surface state. Although we did not make a similar full analysis of the LL plot for $(x, y) = (0.54, 1.3)$ starting from ARPES data, we note that

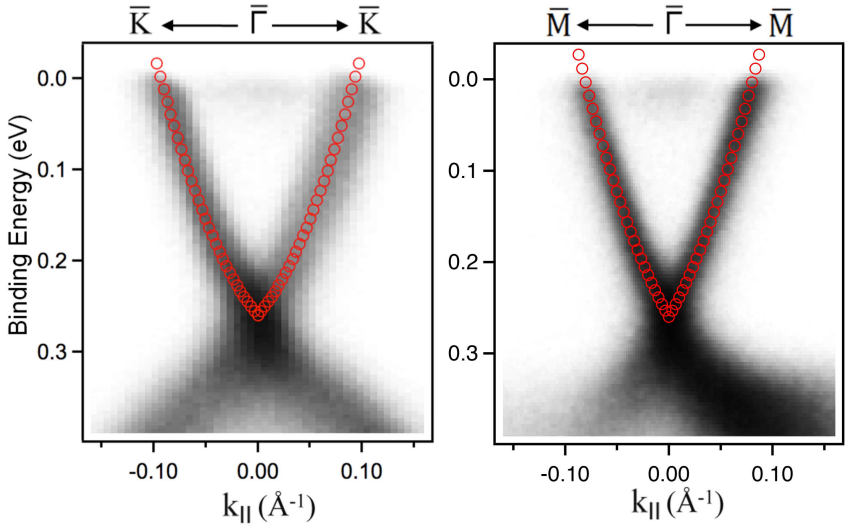

Figure 5.4: *Electronic band structure of a $Bi_{1.5}Sb_{0.5}Te_{1.7}Se_{1.3}$ sample acquired by ARPES. The fit using* ***Equation*** *5.2 (red open circles) is overlaid on the experimental data (grey-scale). The data are along the $\Gamma \rightarrow K$ (left panel) and $\Gamma \rightarrow M$ (right panel) high-symmetry directions and have been acquired using 27 eV photons and linear horizontal polarization. ARPES has been performed at 16 K.*

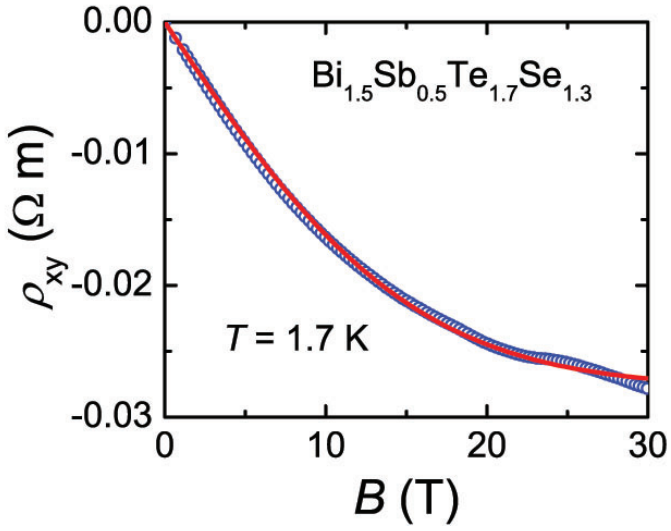

Figure 5.5: *Hall resistivity $\rho_{xy}(B)$ of a $Bi_{1.5}Sb_{0.5}Te_{1.7}Se_{1.3}$ crystal of thickness 40 μm (blue circles) measured at $T = 1.7$ K and $\theta = 0°$. The red line shows the fit based on the two-band model described in* ***Equation*** *5.3.*

minor changes in bulk stoichiometry do not affect the ARPES spectra of BSTS [160].

5.3.3 Hall resistance

A full determination of the transport parameters can be made by analyzing the Hall resistivity, ρ_{xy}. In **Figure** 5.5 we show ρ_{xy} for the BSTS crystal with $(x, y) = (0.50, 1.3)$ and thickness $t = 40$ μm measured up to 30 T at $T = 1.7$ K. Since the surface and

bulk-carriers contribute in-parallel to the Hall voltage, we use the standard two-band model [115] to fit the data

$$\rho_{xy}(B) = -\frac{B}{e}\frac{(n_b\mu_b^2 + n_s\mu_s^2/t) + B^2\mu_b^2\mu_s^2(n_b + n_s/t)}{(n_b\mu_b + n_s\mu_s/t)^2 + B^2\mu_b^2\mu_s^2(n_b + n_s/t)^2} \tag{5.3}$$

where n_b, μ_b, n_s, μ_s are the bulk carrier density, bulk carrier mobility, surface carrier density and surface carrier mobility, respectively. Here n_b and μ_b are fit parameters, while $n_s = 1.5 \times 10^{12}$ cm^{-2} and $\mu_s = 560$ cm^2 /Vs are taken from the analysis of the SdH oscillations. As shown in **Figure** 5.5, the $\rho_{xy}(B)$ curve (blue circles) is well fitted by the model (red line) and the fit yields $n_b = 2.9 \times 10^{16}$ cm^{-3} and bulk carrier mobility $\mu_b = 15$ cm^2/Vs. The surface, ρ_s, and bulk resistivity, ρ_b, are related via $\rho_s = \rho_{sheet}t = t/en_s\mu_s$ with ρ_{sheet} the surface sheet resistivity and $\rho_b = 1/en_b\mu_b$, which yields $\rho_s = 29\ \Omega$cm and $\rho_b = 14\ \Omega$cm. Therefore, the surface contribution accounts for 32 % of the total sample conductance according to the formula $\rho_s^{-1}/(\rho_s^{-1} + \rho_b^{-1})$, which is larger than that reported in Bi_2Te_3 [149], Bi_2Te_2Se [27] and $Bi_{1.5}Sb_{0.5}Te_{1.7}Se_{1.3}$ [30].

5.4 Summary

A magnetotransport study was carried out on low-carrier crystals of the topological insulator $Bi_{2-x}Sb_xTe_{3-y}Se_y$ with $(x, y) = (0.50, 1.3)$ and $(x, y) = (0.54, 1.3)$. In high magnetic fields Shubnikov - de Haas oscillations were observed originating from 2D surface states as demonstrated by the angular variation when tilting the sample surface with respect to the field. For $(x, y) = (0.50, 1.3)$ the Landau level plot was analyzed with a model incorporating a non-ideal Dirac dispersion that was measured directly using ARPES, and a Zeeman coupling-term with large g_s-factor. These effects lead to a shift in the apparent Berry phase extracted from the extrapolated x-axis crossing of the linear Landau level plot. Based on the band parameters deduced from ARPES measurements carried out on a sample prepared from the same single-crystalline batch, the SdH oscillations can be attributed to topological surface states with an electron spin g-factor $g_s = 70$ or -54 as fitting parameter in the LL plot model. By combining the carrier density and mobility for the topological surface states from the SdH data with a two-band (bulk + surface) model for the Hall resistivity, the surface contribution to the total electrical transport can be extracted and amounts to around 32 % in our $Bi_{1.5}Sb_{0.5}Te_{1.7}Se_{1.3}$ crystal with a thickness of 40 μm.

Chapter 6

Superconductivity and magnetic order in the non-centrosymmetric Half Heusler compound ErPdBi

We report superconductivity at $T_c = 1.22$ K and magnetic order at $T_N = 1.06$ K in the semi-metallic noncentrosymmetric Half Heusler compound ErPdBi. The upper critical field, B_{c2}, has an unusual quasi-linear temperature variation and reaches a value of 1.6 T for $T \to 0$. Magnetic order is found below T_c and is suppressed at $B_M \sim 2.5$ T for $T \to 0$. Since $T_c \simeq T_N$, the interaction of superconductivity and magnetism is expected to give rise to a complex ground state. Moreover, electronic structure calculations show ErPdBi has a topologically nontrivial band inversion and thus may serve as a new platform to study the interplay of topological states, superconductivity and magnetic order.

6.1 Introduction

The ternary compound ErPdBi belongs to the Rare Earth palladiumbismuthide (REPdBi) series, which is part of the large family of Half Heusler compounds that crystallize in a cubic structure with 1:1:1 composition. Half Heusler compounds attract ample attention as multifunctional materials in the fields of spintronics and thermoelectricity, but also as tunable laboratory tools to study a wide range of intriguing physical phenomena, such as half metallic magnetism, giant magnetoresistance and Kondo and heavy fermion physics [33]. More recently, a strong interest in Half Heusler compounds with significant spin-orbit coupling has been generated by first-principle calculations [34, 35, 164] that predict an inverted band order, which may give rise to topological quantum states because of the non-trivial Z_2 topology [1, 3]. Prominent candidate materials are the TPtBi and TPdBi series, where T is Y or Sc or a non-magnetic RE element. Interestingly, some of the platinumbismuthides that exhibit band inversion have been reported to superconduct, which makes them promising candidates for topological superconductivity: LaPtBi ($T_c = 0.9$ K [52]), YPtBi ($T_c = 0.77$ K [49, 51]) and LuPtBi ($T_c = 1.0$ K [53]). Moreover, since the crystal structure lacks inversion symmetry, unconventional Cooper pair states, notably mixed even and odd parity states, are predicted to make up the superconducting condensate [165]. This provides a strong motivation to search for similar phenomena in the palladiumbismuthides.

The REPdBi compounds crystallize, just like the REPtBi series, in the cubic structure with the non-centrosymmetric $F\bar{4}3m$ space group [166]. The magnetic and transport properties of the REPdBi series (RE= Er, Ho, Dy, Gd and Nd) were first reported in Refs. [167–169]. Susceptibility data, taken on arc-melted polycrystalline samples, showed antiferromagnetic order for the Ho, Dy, Gd and Nd compounds with Néel temperatures, T_N, of 2, 3.5, 13 and 4.2 K, respectively. ErPdBi did not show magnetic order down to the lowest temperature measured, $T = 1.7$ K. The susceptibility, $\chi(T)$, of ErPdBi follows the Curie-Weiss law with an effective moment $\mu_{eff} = 9.2\ \mu_B$, close to the Er^{3+} free ion value of 9.58 μ_B, and a paramagnetic Curie temperature $\Theta_P = -4.6$ K [167, 168]. Transport measurements revealed a semi-metallic-like behaviour with a carrier density $n(4\text{ K}) = 6.7 \times 10^{19}$ cm^{-3}. ErPdBi received furthermore interest because of its thermoelectric effects [170, 171].

Here we report electrical transport, ac-susceptibility and dc-magnetization measurements on ErPdBi single crystals that provide solid evidence for superconductivity at 1.22 K and magnetic order at 1.06 K. The combination of superconductivity and magnetic order is unusual. Moreover, electronic structure calculations show ErPdBi has an inverted band order and thus should harbor topological quantum states.

6.2 Experimental

A single crystalline batch of ErPdBi was prepared out of Bi flux. As starting materials served the elements Er, Pd and Bi with a purity of 3N5, 4N and 5N, respectively. An ingot of ErPdBi was prepared by arc-melting and placed in an alumina crucible with excess Bi flux. The crucible and contents were heated in a quartz tube under a pressure of 0.3 bar high-purity Argon gas to 1150 °C and kept at this temperature for 36 h. Then the tube was slowly cooled to 500 °C at a rate of 3 °C per hour to form the crystals. Scanning Electron Microscopy and Electron Probe Micro Analysis confirmed the main phase is ErPdBi with composition 1:1:1. Bi precipitates are found in the form of thin lines on the surface of the crystals. Powder X-ray diffraction confirmed the $F\bar{4}3m$ space group and the extracted lattice parameter, $a = 6.595$ Å, is in perfect accord with the literature [166]. The Bi precipitates give rise to additional tiny peaks in the diffraction patterns. From their intensity we estimate a Bi volume fraction of about 4%. Single crystals, with typical dimensions $3 \times 2 \times 0.3$ mm^3, were carefully cut from the ingot by spark erosion thereby avoiding the Bi precipitates. Their single-crystalline nature was checked by Laue backscattering. After cutting, the surface of the samples was cleaned by polishing. Magnetic characterization in the temperature interval 1.8-300 K was made in a Physical Property Measurements System (Quantum Design). The Curie-Weiss behaviour was confirmed and the values $\mu_{eff} = 9.54\ \mu_B$ and $\Theta_P = -3.5$ K are close to the ones reported in Refs. [167, 168]. The Hall effect and resistivity were measured using a MaglabExa system (Oxford Instruments) for $T = 4$ - 300 K. Resistance and ac-susceptibility measurements were made in a ^{3}He refrigerator (Heliox, Oxford Instruments) for $T = 0.24 - 10$ K using a low-frequency ($f \leq 313$ Hz) lock-in technique and low excitation currents ($I \leq 100\ \mu$A). Additional low-temperature dc-magnetization and ac-susceptibility measurements were made using a SQUID magnetometer, equipped with a miniature dilution refrigerator, developed at the Néel Institute.

6.3 Results

In **Figure** 6.1 we show the resistivity $\rho(T)$ of a flux grown single crystal of ErPdBi (sample #1). The overall behaviour is in good agreement with the data in the literature with a broad maximum centered at 50 K, rather than 140 K [169]. The hole carrier concentration, calculated from the low-field linear Hall resistance, equals $n_h = 7.4 \times 10^{18}$ cm^{-3} at $T = 4$ K (see inset), which is a factor 10 lower than reported in Ref. [169]. These transport parameters confirm semimetallic-like behaviour. At low temperatures the drop to resistance $R = 0$ signals the transition to the superconducting state.

In **Figure** 6.2 we show ac-susceptibility data taken on the same ErPdBi sample that reveal superconductivity occurs below $T_c = 1.22(2)$ K. The superconducting transition

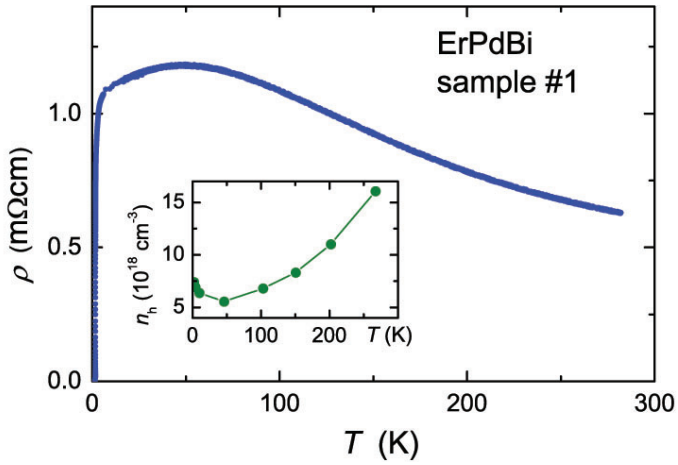

Figure 6.1: *Resistivity and carrier concentration (inset) versus temperature of ErPdBi sample #1.*

appears as a large diamagnetic contribution, which corresponds to a screening fraction of $\sim 92\%$ of the ideal value $\chi_M = -1/(1-N)$ (here $N \simeq 0.1$ is the demagnetization factor). χ_{ac} data taken on a second sample (#2) with $N \simeq 0.15$ in a different experimental set-up are reported in the lower inset of **Figure** 6.2. For this sample the screening fraction attains a value of $\sim 90\%$. It should be noted that in both experiments a decrease of the χ_{ac} signal becomes visible already at a higher temperature, $1.72(2)$ K (as indicated by the grey arrows in **Figure** 6.2). This signal we attribute to an impurity phase with a screening fraction of $\sim 8-10\%$. A large diamagnetic signal is normally a good indicator of bulk superconductivity. Solid proof may be obtained by the observation of flux expulsion. In the upper inset of **Figure** 6.2 we show the dc-magnetization measured in a field of 20 Oe after cooling in zero field. Upon warming, the signal is dominated by screening effects due to ErPdBi (up to 1.22 K) and the impurity phase (up to 1.72 K). Upon cooling in field, flux expulsion is predominantly found at $T_c = 1.22$ K. The change in magnetization corresponds to a Meissner fraction of ~ 15 %. This confirms the bulk origin of superconductivity in ErPdBi.

The nature of the impurity phase remains to be solved. Small amounts of Bi inclusions in the form of precipitates might be present in the crystals, but crystalline Bi does not superconduct. Amorphous Bi, *e.g.* prepared as thin film, superconducts at $T_c \sim 6$ K [172], a temperature much higher than observed here. Among the binary Bi-Pd alloys, the only likely candidate is α-Bi_2Pd, which is reported to superconduct at 1.7 K [172]. However, if present in our samples, the impurity amount is below the detection limit of the X-ray powder diffraction pattern (~ 2 %). We remark that in Refs. [169, 170] a pronounced drop in the resistivity of *arc-melted* ErPdBi samples was reported at 7 K, together with a field depression that mimics superconductivity. However, no corresponding diamagnetic signal was observed and bulk superconductivity at 7 K was discarded.

χ_{ac}-data taken upon cooling in applied magnetic fields show the diamagnetic screening

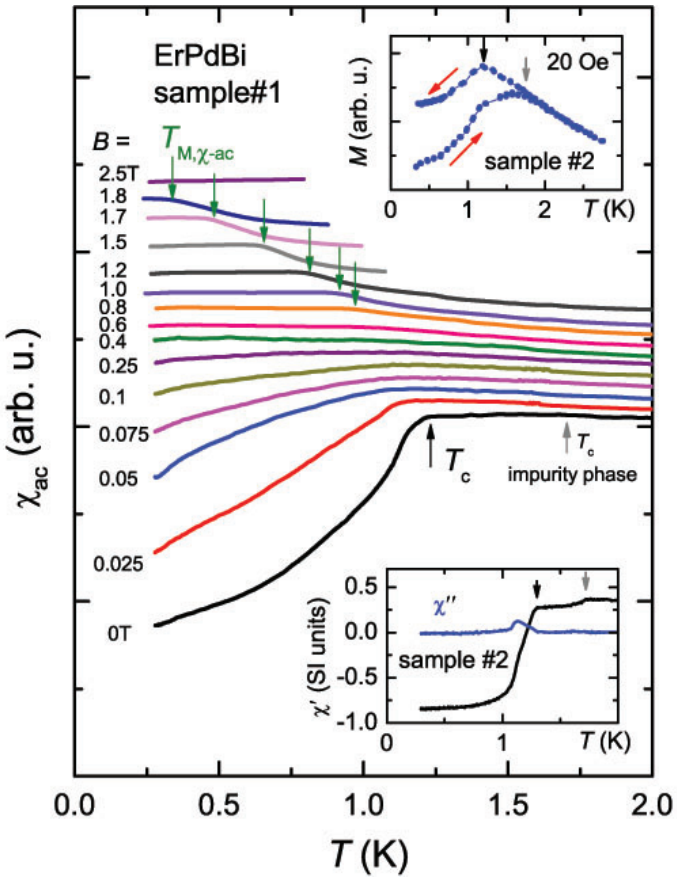

Figure 6.2: *AC susceptibility of ErPdBi (sample #1) in zero and magnetic fields up to 2.5 T as indicated. The data were taken while cooling in field. Curves are displaced vertically to prevent overlap. The driving field is 0.026 Oe for $B \leq 0.4$ T and 0.26 Oe for $B \geq 0.6$ T. The superconducting transition temperature of ErPdBi and the impurity phase are indicated by black and grey arrows. For $B \geq 0.6$ T the weak local maximum locates the magnetic transition at $T_{M,\chi_{ac}}$ (green arrows). Lower inset: χ' and χ'' of ErPdBi (sample #2) in a driving field of 0.027 Oe. Upper inset: Magnetization measured in a field of 20 Oe applied after cooling in zero field; data taken upon warming show screening effects, while data taken upon cooling show flux expulsion (see text).*

signal is rapidly lost (see **Figure** 6.2). Surprisingly, in the field range 0.6 T $\leq B <$ 2.5 T a pronounced structure appears in $\chi_{ac}(T)$ at temperatures labeled $T_{M,\chi_{ac}}$. Such a (relative) maximum, albeit weak, normally indicates the presence of a magnetic transition. This is corroborated by the field variation of $T_{M,\chi_{ac}}$, which we will discuss after presenting low-temperature resistivity data, $\rho(T)$.

The superconducting transition in $\rho(T)$ in zero and applied magnetic fields is reported in **Figure** 6.3. In zero field the superconducting transition is due to the impurity phase, where we remark that the transition temperature, $1.74(2)$ K, determined by the midpoint, nicely coincides with the onset temperature, $1.72(2)$ K, in the χ_{ac}-data. In a magnetic field superconductivity of the impurity phase is depressed at the fast rate $dT_c/dB = -4.4$ K/T (see **Figure** 6.4). Consequently, for $B \geq 0.1$ T and $T \lesssim 1.2$ K the superconducting

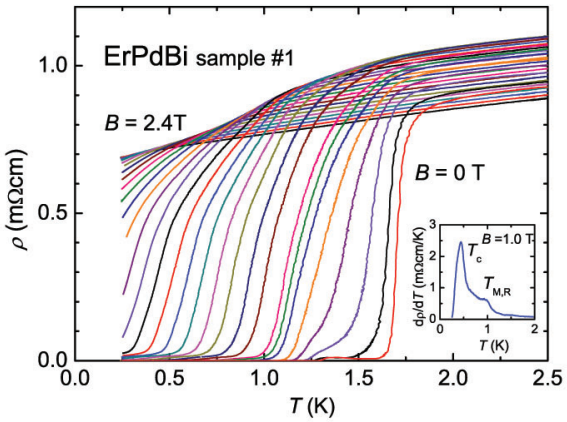

Figure 6.3: *Resistivity of ErPdBi in zero and applied magnetic fields, from right to left: 0, 0.025, 0.05, 0.075, 0.10, 0.13, 0.16, 0.2 T and then up to 2.4 T in steps of 0.1 T. Inset: $d\rho/dT$ versus T in $B = 1.0$ T. The extrema locate T_c and $T_{M,R}$.*

transition in $\rho(T)$ is due to ErPdBi. At the same time, $\rho(T)$ obtains an unusual round shape around T_c. We have determined the upper critical field B_{c2} (or $T_c(B)$) by locating the maximum in $d\rho/dT$ measured at fixed magnetic field, as shown for example for $B = 1.0$ T in the inset of **Figure** 6.3. The results are traced in the phase diagram **Figure** 6.4. $B_{c2}(T)$ of ErPdBi displays an unusual quasi-linear temperature variation, which extrapolates to $T_c = 1.24(2)$ K in zero field, close to the onset temperature $T_c = 1.22(2)$ K extracted from χ_{ac}.

The magnetic transition is also detected in the resistance by the local maximum in $d\rho/dT$, as shown in the inset of **Figure** 6.3 (temperature labeled $T_{M,R}$). We have traced $T_{M,R}(B)$ and $T_{M,\chi_{ac}}(B)$ in the phase diagram **Figure** 6.4. Both temperatures track the same phase boundary. The location of weak maxima (see **Figure** 6.4) observed in the dc-magnetization (data not shown) for sample #2 confirm this.

The magnetic transition is almost certainly to an antiferromagnetic (AFM) state with Néel temperature T_N. For $T_N = T_{M,R}$ the phase boundary obeys the phenomenological order parameter function $B_M(T) = B_M(0)(1 - (T/T_N)^\alpha)^\beta$ with $T_N = 1.06$ K, $B_M(0) = 2.5$ T, $\alpha = 2$ and $\beta = 0.4$. The latter value is close to the value $\beta = 0.38$ expected for the 3D Heisenberg antiferromagnet [173]. The phase boundaries located by the transport and magnetic data are closely linked, since they all extrapolate to $T_N = 1.06$ K for $B \to 0$. Local moment AFM order is widely present in the REPdBi series [167, 168]. Strong support for an antiferromagnetic groundstate in ErPdBi is furthermore found in the De Gennes scaling for the heavy rare earth palladium bismuthides (see inset **Figure** 6.4): $T_N \propto (g_J - 1)^2 J(J + 1)$ with g_J the Landé factor (see *e.g.* [174]. Neutron diffraction and/or NMR experiments would be most welcome to investigate the nature of the magnetic order on the microscopic scale.

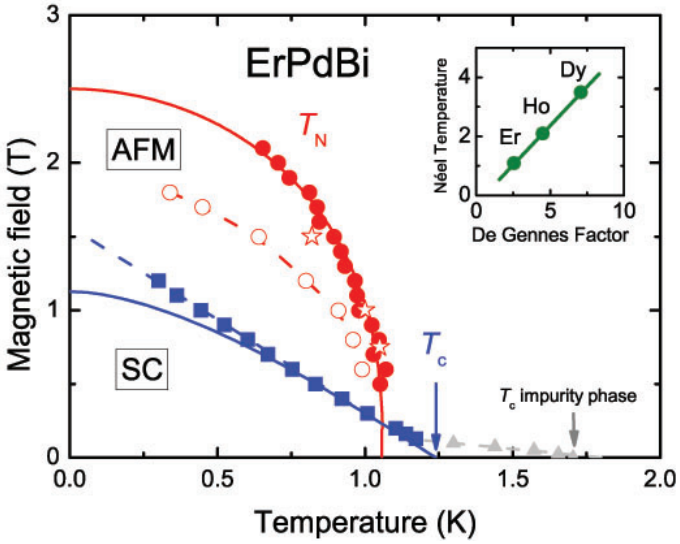

Figure 6.4: *Superconducting (SC) and magnetic (AFM) phase diagram of ErPdBi. Closed blue squares: superconducting transition temperature, T_c, determined by extrema in $d\rho/dT$; solid blue line: $B_{c2}(T)$ WHH model curve (see text) with $B_{c2}^{orb}(0) = 1.13$ T. Grey triangles and dashed grey line: $T_c(B)$ of the impurity phase. Closed circles: $T_N = T_{M,R}$ determined by extrema in $d\rho/dT$; open circles and stars: $(T, B)-$location of weak maximum in $\chi_{ac}(T)$ ($T_{M,\chi_{ac}}$) and dc-magnetization (sample #2); solid red line: magnetic order parameter fit with $T_N = 1.06$ K at $B = 0$ T (see text). Inset: De Gennes scaling plot for Er, Ho and DyPdBi (see text).*

6.4 Discussion

The combination of local-moment antiferromagnetism and superconductivity is unusual. In general local-moment AFM order and superconductivity tend to compete for the ground state. However, in ErPdBi $T_N \simeq T_c$, which tells us both phenomena have similar energy scales. Given the lack of inversion symmetry and the expected unconventional Cooper-pair state [175], this could give rise to an interesting interplay of superconductivity and magnetism, and a complex ground state. Experimental signatures for this are the unusual rounded shape of the superconducting transition in $\rho(T)$ and the rapid loss of the diamagnetic screening signal in field. Possibly AFM order and superconductivity occupy different sample regions. In order to answer these important questions muon spin relaxation experiments would be very helpful, since these permit one to probe the different volume fractions.

Several other Erbium based antiferromagnetic superconductors have been reported in the literature. In the Chevrel phases $ErMo_6S_8$ and $ErMo_6Se_8$ [176] AFM order and superconductivity compete, while in the borocarbide $ErNi_2B_2C$ [177] and the Heusler phase $ErPd_2Sn$ [178] AFM order and superconductivity coexist. Coexistence of superconductivity and AFM order is also found in a number of non-centrosymmetric materials [175]. A prominent example is $CePt_3Si$ with $T_c = 0.75$ K and $T_N =$ 2.2 K [179]. Interestingly,

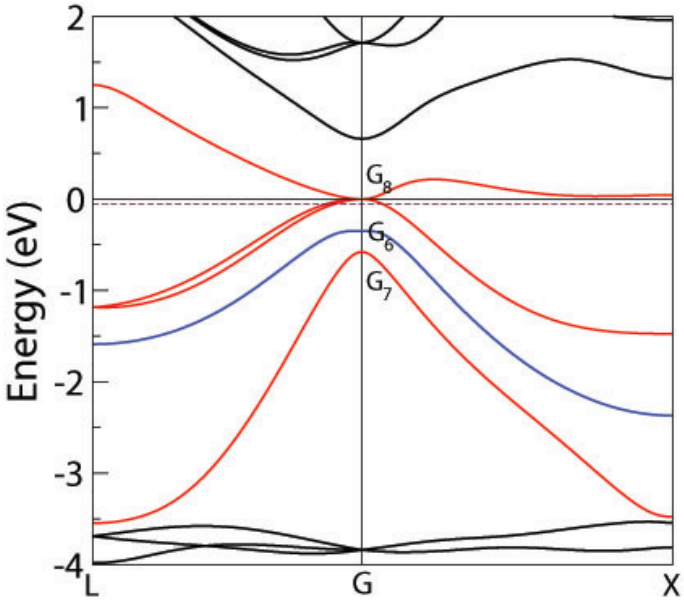

Figure 6.5: *Bulk band structure of half Heusler ErPdBi in the fcc Brillouin zone. The red bands are Γ_8 and Γ_7 states and blue is the Γ_6 state. The Fermi energy is shifted to zero (solid horizontal line). The dashed-horizontal line illustrates the experimental Fermi level with a small hole-pocket at the Γ point. Er-$4f$ states were treated as core electrons.*

CePdBi, which has the same crystal structure as ErPdBi, also undergoes a magnetic ($T_M = 2$ K) and superconducting transition ($T_c = 1.4$ K) [180]. However, the experiments were carried out on arc-melted polycrystals and the weak diamagnetic screening (8 % of the sample volume) was hitherto associated with a disordered phase.

The upper critical field of ErPdBi, reported in **Figure** 6.4, shows an unusual linear temperature variation just like for YPtBi [49], where it was taken as evidence for an odd-parity component in the superconducting order parameter. For ErPdBi, the rounded transitions in $\rho(T)$ and the presence of AFM order, make the determination of $B_{c2}(T)$ difficult. In the limit $T \to 0$ B_{c2} extrapolates to 1.6 T. Using this value and with help of the relation $B_{c2} = \Phi_0/2\pi\xi^2$, where Φ_0 is the flux quantum, we calculate a superconducting coherence length $\xi = 14$ nm. Preliminary magnetization measurements show the lower critical field B_{c1} is very small, and a conservative upperbound is 0.0002 T, which allows an estimation of the Ginzburg-Landau parameter $\kappa = \lambda/\xi$ via the relation $B_{c2}/B_{c1} = 2\kappa^2/ln\kappa$, where λ is the penetration depth. For $T \to 0$, we obtain $\kappa \geq 140$ and $\lambda \geq 448$ nm. In **Figure** 6.4 we also compare the measured $B_{c2}(T)$-values with the model curve for a weak-coupling spin-singlet superconductor in the clean limit with orbital limiting field (Werthamer-Helfand-Hohenberg [WHH] model [181]). The zero temperature orbital critical field is given by $B_{c2}^{orb} = 0.72 \times T_c \left|dB_{c2}/dT\right|_{T_c}$ and amounts to 1.13 T. Clearly, the $B_{c2}(T)$-values determined from the resistance data exceed the model curve values when $T/T_c \lesssim 0.5$. This is in line with an unconventional Cooper pair state [49].

6.5 Electronic structure

In order to understand the electronic properties of ErPdBi, we performed *ab initio* band structure calculations based on the density-functional theory within the generalized gradient approximation [182]. We adopted the Half Heusler structure as determined by experiments. The magnetic susceptibility that follows a Curie-Weiss law [167, 168] reveals the Er-$4f$ electrons are well localized and hardly hybridize with Pd and Bi states [183]. As a consequence, the Er-$4f$ states are not relevant to the low energy states near the Fermi energy (E_F). Therefore, we placed the Er-$4f$ electrons inside the core and represented all the core electrons by the projector-augmented-wave potential [184, 185]. Spin-orbit coupling was included in all calculations.

The calculated bulk band structure of ErPdBi is shown in **Figure** 6.5. The lowest conduction and highest valence bands with Γ_8 symmetry ($j = 3/2$) are degenerate at E_F at the Γ point due to the cubic symmetry, resulting in a zero-gap semimetal. This semimetallic feature is consistent with the magnetotransport measurements (see Fig. 1). The spin-orbit coupling split-off Γ_7 state ($j = 1/2$) is below the Γ_6 state. One can clearly see a band inversion between the Γ_8 and Γ_6 bands, where the Γ_8 bands are mainly contributed by Pd-$4d$ and Bi-$6p$ orbitals, while Γ_6 by Pd-$5s$ and Bi-$6s$ orbitals. Regardless of magnetic moments from the Er-$4f$ states, this band inversion means that (undoped) ErPdBi is a topological insulator, similar to HgTe and other Half Heusler topological insulators [34, 35, 164]. Robust topological states are expected to exist on the surface. More interestingly, the magnetism from Er-$4f$ states can interplay with these topological surface states and generate exotic magnetoelectric effects [186]. Since the ErPdBi crystals are slightly p-doped as concluded from the Hall data (**Figure** 6.1), the real E_F is expected to lie marginally below the Γ_8 degenerate point with a small hole-pocket, as illustrated in **Figure** 6.5. The bulk superconductivity can be attributed to these heavy-hole Γ_8 states.

6.6 Summary

Electrical transport, ac-susceptibility and dc-magnetization measurements provide solid evidence for superconductivity at 1.22 K and antiferromagnetic order at 1.06 K in the non-centrosymmetric Half Heusler compound ErPdBi. The combination of superconductivity and AFM order is unusual. Possibly, the ordering phenomena occur in different electron subsystems: superconductivity in the low-carrier hole band and local moment magnetism due to Er $4f$-moments. However, since $T_N \simeq T_c$, and ErPdBi lacks inversion symmetry, the interplay of superconductivity and magnetism might give rise to a complex ground state. Electronic structure calculations show ErPdBi has an inverted band order and thus may harbor topological quantum states. We conclude the Half Heusler REPdBi series provides a unique opportunity to investigate the interplay of antiferromagnetic order,

superconductivity and topological quantum states.

6.7 Further developments

After the work above was published, two other papers appeared that also reported the transport and magnetic properties of ErPdBi [46, 187]. Nakajima *et al.* [46] found superconductivity in ErPdBi with T_c around 1.2 K, by means of electric resistance and AC susceptibility measurements, and antiferromagnetic order with T_N = 1.0 K by means of specific heat and magnetization measurements. These results confirm our work. In Ref. [187], antiferromagnetic order with a somewhat higher T_N = 1.2 K was found and an onset for superconductivity at T_c = 1.6 K using AC susceptibility. Also, magnetoresistance measurements in high magnetic fields up to 33 T revealed Shubnikov-de Haas (SdH) oscillations, with a frequency of 21 T. This points to a low carrier concentration.

In 2014 superconductivity was reported for the nonmagnetic rare-earth palladiumbismuthide (*RE*PdBi) LuPdBi with T_c in the range 1.6 - 1.9 K [46, 54, 55]. A still unexplained result is that only Xu *et al.* [54] report the observation of a sizeable transition at T_c = 1.45 K in the specific heat, whereas the other groups did not [46, 55]. Xu *et al.* [54] and Pavlosiuk *et al.* [55] also analyzed magnetoresistivity data with the weak antilocalization effect (WAL), from which they claimed the presence of topological surface states. However, the prefactor α of the Hikami-Larkin-Nagaoka formula (see **section** 3.3) for the WAL in both papers is around 10^5 larger than that expected for a topological surface state. This puts serious doubts on this interpretation.

In 2015 we discovered superconductivity in the antiferromagnet (T_N = 2.0 K) HoPdBi [44]. AC susceptibility measurements provides solid evidence for bulk superconductivity below T_c = 0.75 K. Electronic structure calculations classified HoPdBi as a new topological semimetal, with a non-trivial band inversion of 0.25 eV. Superconductivity and antiferromagnetic order were confirmed in subsequent papers by Nakajima *et al.* and Pavlosiuk *et al.* [45, 46]. Apparently, ErPdBi and HoPdBi are both highly interesting laboratory tools to study the interplay of antiferromagnetic order, superconductivity and topological quantum states.

Finally, Nakajima *et al.* [46] showed that the coexistence of superconductivity and magnetism is a general feature of the *RE*PdBi (*RE* = Sm, Gd, Tb, Dy, Ho, Er, Tm) compounds (with the exception of *RE* = Gd). For the compounds with a lattice parameter smaller than 6.62 Å the band structure is inverted near the Γ point, and consequently *RE*PdBi (*RE* = Ho, Er, Tm, and Lu) are predicted to harbor topological surface states. Superconductivity is ascribed to the conduction electrons due to the Bi $6p$ band and Pd $4d$ band. On the other hand, the effective moments deduced from the magnetic susceptibility are all close to the free ion value, which strongly suggests the magnetism is due to local moments. The magnetic structure was investigated by neutron diffraction for DyPdBi [46]

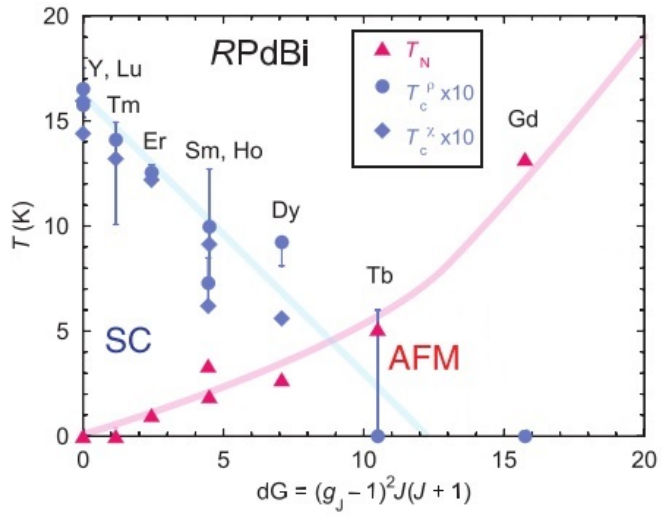

Figure 6.6: *Superconducting transition temperature T_c and antiferromagnetic transition temperature T_N plotted as a function of de Gennes factor for* RE*PdBi (*RE = *Y, Sm, Gd, Tb, Dy, Ho, Er, Tm, and Lu). T_c^ρ (blue circles), T_c^χ (blue diamonds) and T_N (red triangles) were determined from electric resistivity, AC susceptibility, and DC magnetic susceptibility, respectively. Figure taken from Ref. [46]*

and HoPdBi [45]. The structure is type II antiferromagnet with a propagation vector of [1/2, 1/2, 1/2] doubling all three crystallographic axes. To illustrate the relationship between superconductivity and antiferromagnetism, T_c and T_N were plotted as a function of the de Gennes factor (See **Figure** 6.6). As the Néel temperature T_N increases with the de Gennes factor, the superconducting transition temperature T_c decreases, which indicates that the superconductivity and antiferromagnetism compete with each other.

Chapter 7

Rotational symmetry breaking in the topological superconductor $Sr_xBi_2Se_3$ probed by upper-critical field experiments

Recently it was demonstrated that Sr intercalation provides a new route to induce superconductivity in the topological insulator Bi_2Se_3. Topological superconductors are predicted to be unconventional with an odd parity pairing symmetry. An adequate probe to test for unconventional superconductivity is the upper critical field, B_{c2}. For a standard BCS layered superconductor B_{c2} shows an anisotropy when the magnetic field is applied parallel and perpendicular to the layers, but is isotropic when the field is rotated in the plane of the layers. Here we report measurements of the upper critical field of superconducting $Sr_xBi_2Se_3$ crystals ($T_c = 3.0$ K). Surprisingly, field-angle dependent magnetotransport measurements reveal a large anisotropy of B_{c2} when the magnet field is rotated in the basal plane. The large two-fold anisotropy, while six-fold is anticipated, cannot be explained with the Ginzburg-Landau anisotropic effective mass model or flux flow induced by the Lorentz force. The rotational symmetry breaking of B_{c2} indicates unconventional superconductivity with an odd-parity spin-triplet Cooper pair state (Δ_4-pairing) recently proposed for rhombohedral topological superconductors, or might have a structural nature, such as self-organized stripe ordering of Sr atoms.

7.1 Introduction

Currently, topological insulators (TIs) are at the focus of condensed matter research, because they offer unprecedented possibilities to study novel quantum states [72, 188, 189]. 3D TIs are bulk insulators with a non-trivial topology of the electron bands that gives rise to surface states at the edge of the material. The gapless surface states have a Dirac-type energy dispersion with the spin locked to the momentum and are protected by symmetry. This makes TIs promising materials for applications in fields like spintronics and magnetoelectrics [188,189]. The concept of a TI can also be applied to superconductors (SCs), where the superconducting gap corresponds to the gap of the band insulator [57,190]. Topological superconductors are predicted to be unconventional, with a mixed even and odd parity Cooper pair state [191, 192]. Much research efforts are devoted to 1D and 2D SCs, where Majorana zero modes exist as protected states at the edge of the SC [148, 193]. Majorana zero modes with their non-Abelian statistics offer a unique platform for future topological quantum computation devices [129]. Prominent candidates for 3D topological SC are the Cu intercalated TI Bi_2Se_3 [59, 60], the doped topological crystalline insulator $Sn_{1-x}In_xTe$ [194] and selected topological half-Heusler compounds [46, 51, 195].

Among the 3D topological superconductors, $Cu_xBi_2Se_3$, which has a SC transition temperature $T_c = 3$ K for $x = 0.3$ [59, 60], is the most intensively studied material. ARPES (Angle Resolved PhotoEmission Spectroscopy) experiments conducted to study the bulk and surface states reveal that the topological character is preserved when Bi_2Se_3 is intercalated with Cu [196]. By evaluating the topological invariants of the Fermi surface, $Cu_xBi_2Se_3$ is expected to be a time-reversal invariant fully-gapped odd-parity topological SC [191, 192]. This was put on a firmer footing by a two-orbital pairing potential model where odd-parity SC is favoured by strong spin-orbit coupling [197]. Several experiments have been interpreted in line with topological SC. The specific heat shows a full SC gap [60]. The upper critical field exceeds the Pauli limit and has a temperature variation that points to spin-triplet SC [49]. Much excitement was generated by the observation of a zero-bias conductance peak in point contact spectroscopy, that was attributed to a Majorana surface state [198]. However, STS (Scanning Tunneling Spectroscopy) showed that the density of states at the Fermi level is fully gapped without any in-gap states [199]. On the other hand, the superconducting state shows a large inhomogeneity [199] and the superconducting volume fraction depends on quenching conditions [200]. Consequently, the issue of topological SC in $Cu_xBi_2Se_3$ has not been settled and further experiments are required, as well as new materials.

Very recently it has been demonstrated that Sr intercalation provides a new route to induce superconductivity in Bi_2Se_3 [61]. Resistivity and magnetization measurements on $Sr_xBi_2Se_3$ single crystals with $x = 0.06$ show $T_c = 2.5$ K. The SC volume fraction amounts to 90 % which confirms bulk SC. By optimizing the Sr content a maximum T_c of

2.9 K was found for $x = 0.10$ [201]. The topological character of Bi_2Se_3 is preserved upon Sr intercalation. ARPES showed a topological surface state well separated from the bulk conduction band [202, 203]. Based on the first measurements of the electronic parameters in the normal and SC states, and the close analogy to $Cu_xBi_2Se_3$, it has been advocated that $Sr_xBi_2Se_3$ is a new laboratory tool to investigate topological SC [61, 201].

Here we report a study of unusual basal-plane anisotropy effects in the upper critical field, B_{c2}, of $Sr_xBi_2Se_3$. Bi_2Se_3 crystallizes in a rhombohedral structure with space group $R\bar{3}m$. It is a layered material and Sr is intercalated in the Van der Waals gaps between the quintuple Bi_2Se_3 layers [61]. For a standard BCS (Bardeen, Cooper, Schrieffer) layered SC the anisotropy of B_{c2} is expressed by the parameter $\gamma^{an} = B_{c2}^{\parallel}/B_{c2}^{\perp}$, where $B_{c2}^{\parallel}$ and $B_{c2}^{\perp}$ are measured with the B-field parallel and perpendicular to the layers, respectively [204]. Whereas $B_{c2}^{\parallel}$ is normally isotropic, $Sr_xBi_2Se_3$ presents a unique exception. Field-angle-dependent magnetotransport experiments demonstrate a large two-fold basal-plane anisotropy of B_{c2}, with $B_{c2}^{a} = 7.4$ T and $B_{c2}^{a^*} = 2.3$ T for $x = 0.15$ at $T/T_c = 0.1$ ($T_c = 3.0$ K), where a and a^* are orthogonal directions in the basal plane. This large effect cannot be explained with the anisotropic effective mass model [204, 205] or the variation of B_{c2} caused by flux flow [206]. The rotational symmetry breaking of B_{c2} indicates unconventional superconductivity [125, 207], or might have a structural nature, such as preferential ordering of Sr atoms.

7.2 Experimental

Single crystals $Sr_xBi_2Se_3$ with $x = 0.10$ and $x = 0.15$ were prepared by melting high-purity elements at 850 °C in sealed evacuated quartz tubes, followed by slowly cooling till 650 °C at the rate of 3 °C/hour. Powder X-ray diffraction confirms the $R\bar{3}m$ space group (see **Section** 2.2). Laue back-scattering diffraction confirmed the single-crystallinity and served to identify the crystal axes a and a^*. Thin bar-like samples with typical dimensions $0.3 \times 1.5 \times 3$ mm^3 were cut from the bulk crystal for the transport measurements. Magnetotransport experiments were carried out in a PPMS-Dynacool (Quantum Design) in the temperature range from 2 K to 300 K and magnetic fields up to 9 T and in a 3-Helium cryostat (Heliox, Oxford Instruments) down to 0.3 K and fields up to 12 T. The resistance was measured with a low-frequency ac-technique in a 4-point configuration with small excitation currents, I, to prevent Joule heating (I = 0.5-1 mA in the PPMS and 100 μA in the Heliox experiments). The current was applied in the basal plane along the long direction of the sample. For in-situ measurements of the angular magnetoresistance the crystals were mounted on a mechanical rotator in the PPMS and a piezocrystal-based rotator (Attocube) in the Heliox. The samples were mounted such that the rotation angle $\theta \simeq 0°$ corresponds to $B \perp I$. Care was taken to align the a-axis with the current direction, but a misorientation of several degrees can not be excluded.

7.3 Results

The resistivity, $\rho(T)$, of our $Sr_xBi_2Se_3$ crystals with $x = 0.10$ and $x = 0.15$ shows a metallic temperature variation with superconducting transition temperatures T_c of 2.8 K and 3.0 K, respectively, see **Figure** A.1 in **Appendix** A. The SC volume fractions of the crystals measured by ac-susceptibility amount to 40 % and 80 %, respectively. In **Figure** 7.1 we show the angular variation of the resistance, $R(\theta)$, measured in a fixed field $B = 0.4$ T directed in the basal plane (aa^*-plane), in the temperature range 2-3 K around T_c ($T_c = 2.8$ K at $B = 0$ T), for $x = 0.10$. Rather than attaining a constant value, the curves show a pronounced angular variation which demonstrates that $B_{c2}(T)$ (or $T_c(B)$) is field-angle dependent. For instance, at 2.5 K and 0.4 T (violet symbols) the sample is in the normal state at $\theta = 3°$ and superconducts ($R = 0$) at $93°$. By raising the temperature from 2 K to 3 K SC is smoothly depressed for all field directions. The data show a striking two-fold symmetry, which is most clearly demonstrated in a polar plot (**Figure** 7.2). We remark, the same two-fold anisotropy is observed in crystals with $x = 0.15$. In the top panel of **Figure** 7.1 we show $R(\theta)$ in the normal state measured in 8 T for $x = 0.10$. The data have been symmetrized after measuring $R(\theta)$ for opposite field polarities to eliminate a small Hall component. $R(\theta)$ in the normal state shows the same two-fold symmetry as in **Figure** 7.1(a). The variation in $R(\theta)$ is small and amounts to 3 % in 8 T. The data follow a $\sin\theta$ dependence, which tells us the variation is due to the classical magnetoresistance related to the Lorentz force $F_L = BI\sin\theta$, where I is the transport current that flows in the basal plane. $R(\theta)$ is minimum in the longitudinal case ($B \parallel I$) and maximum in the transverse case ($B \perp I$).

In **Figure** 7.3 we report $B_{c2}(T)$ for two single crystals measured with the B-field along the orthogonal directions in the hexagonal unit cell. The data points are obtained by measuring the superconducting transition in $R(T)$ in fixed fields, where T_c is identified by the 50 % drop of R with respect to its value in the normal state (see **Appendix** A). In determining the values of B_{c2} we did not correct for demagnetization effects, since the demagnetization factors calculated for our crystals are small (see **Appendix** A). As expected from the data in **Figure**. 7.1, we observe a large difference between B^a_{c2} and $B^{a^*}_{c2}$, with an in-plane anisotropy parameter $\gamma^{an}_{aa^*} = B^a_{c2}/B^{a^*}_{c2}$ of 6.8 (at 1.9 K) and 2.6 (at 0.3 K) for $x = 0.10$ and $x = 0.15$, respectively. For both crystals $B^{a^*}_{c2} \approx B^c_{c2}$. Obviously, the B_{c2} ratio γ^{an} for the field $\parallel$ and $\perp$ to the layers depends on the field angle and ranges from 1.2 to 3.2 for $x = 0.15$. In Ref. [201] a value for γ^{an} of 1.5 is reported, whereas from the data in Ref. [61] we infer a value of 1. In the top panels of **Figure** 7.3 we show $\rho(B)$ measured along the a, a^* and c axis at $T = 2.0$ K and $T = 0.3$ K for $x = 0.10$ and $x = 0.15$, respectively. The $B_{c2}(T)$ values are determined by the midpoints of the transitions to the normal state, and are indicated by open symbols in the lower panels. The agreement between both methods (field sweeps and temperature sweeps) is excellent. For

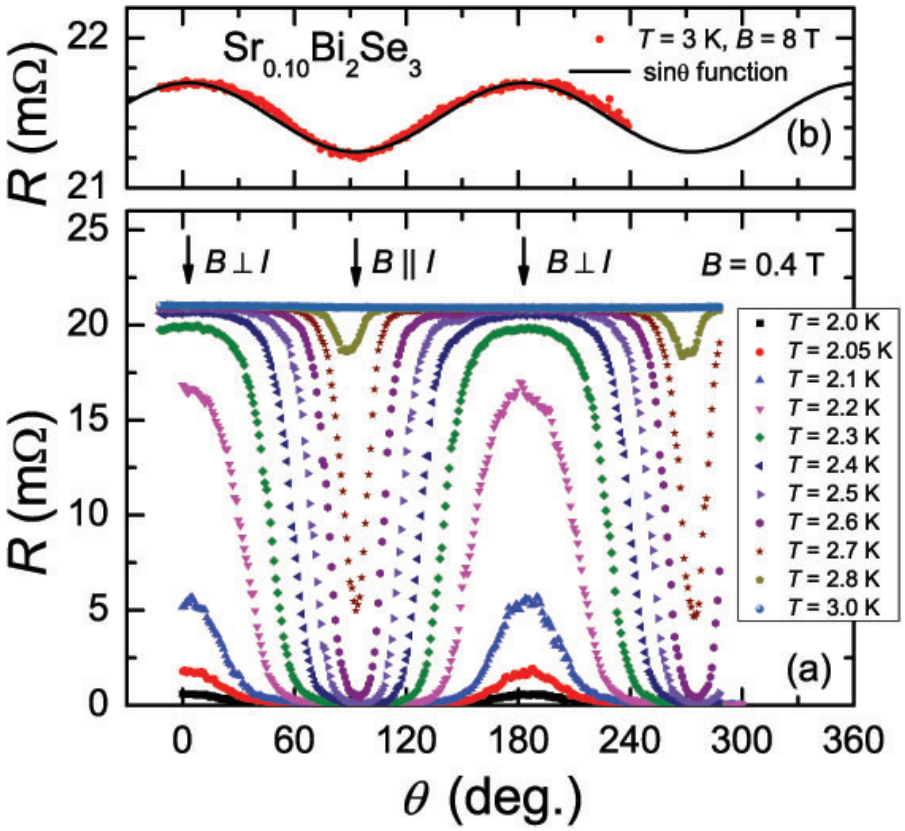

Figure 7.1: *Angular variation of the resistance of $Sr_{0.10}Bi_2Se_3$. Lower panel: Resistance of $Sr_{0.10}Bi_2Se_3$ as a function of angle θ at $B = 0.4$ T and temperatures between 2.0 K (bottom) and 3.0 K (top). The angle $\theta = 3°$ corresponds to $B \perp I$ and $\theta = 93°$ to $B \parallel I$ as indicated by arrows. The current direction is along the a-axis, with a precision of several degrees. The data are measured with increasing angle, and reproduce when the rotation direction is reversed, apart from a small backlash in the rotator of $2°$. Upper panel: $R(\theta)$ in the normal state at $T = 3.0$ K and $B = 8$ T. The solid line shows $R(\theta)$ can be described by a $\sin\theta$ function.*

the $x = 0.15$ sample we see a remarkable broadening for $B \parallel a$. The initial small increase of $\rho(B)$ between 4 and 6 T is most likely related to a sample inhomogeneity, because a similar tail is also observed in the $R(T)$ data (see **Appendix** A).

In **Figure** 7.4 we show the angular variation of the upper critical field, $B_{c2}(\theta)$. For this experiment the crystals are placed on the rotator and the field is oriented in the basal plane. The data points are obtained as the midpoints of the transitions to the normal state of the $R(B)$ curves measured at temperatures of 2 K for $x = 0.10$ and of 0.3 K and 2 K for $x = 0.15$ (see **Figure** A.4 in **Appendix** A). All data sets show the pronounced two-fold basal-plane anisotropy of B_{c2}, already inferred from **Figures** 7.1 and 7.2.

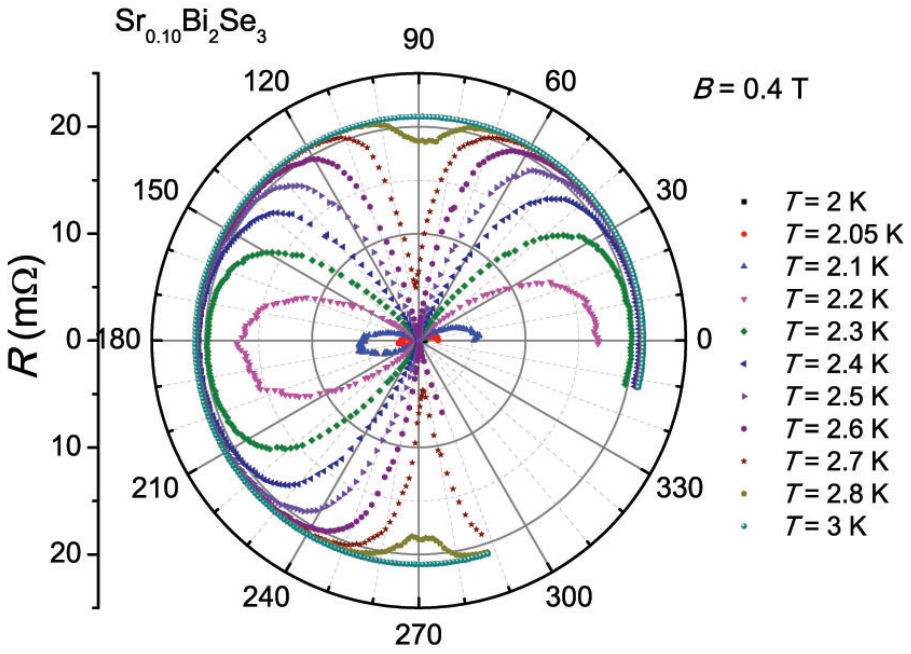

Figure 7.2: *Polar plot of the resistance of $Sr_{0.10}Bi_2Se_3$. Resistance of $Sr_{0.10}Bi_2Se_3$ as a function of angle θ in a magnetic field of 0.4 T and temperatures ranging from 2.0 K to 3.0 K presented in a polar plot. The angle $\theta = 3°$ corresponds to $B \parallel a^* \perp I$, while $\theta = 93°$ corresponds to $B \parallel a \parallel I$.*

7.4 Discussion

Having conclusively established the two-fold anisotropy of B_{c2} in the basal plane, we now turn to possible explanations. A first explanation could be a lowering of the symmetry caused by a crystallographic phase transition below room temperature. However, the powder X-ray diffraction patterns measured at room temperature and $T = 10$ K are identical (see **Figure** 2.5 in **Section** 2.2). Moreover, the resistivity traces ($T = 2 - 300$ K, **Figure** A.1) and the specific heat ($T = 2 - 200$ K, **Figures** A.5) all show a smooth variation with temperature and do not show any sign of a structural phase transition (see **Appendix** A). We therefore argue our crystals keep the $R\overline{3}m$ space group at low temperatures.

A second explanation for breaking the symmetry in the basal plane could be the measuring current itself. Since the current flows in the basal plane it naturally breaks the symmetry when we rotate the field in the basal-plane. Indeed B_{c2} is largest for $B \parallel I$ and smallest for $B \perp I$. In the latter geometry, and for large current densities, the Lorentz force may cause flux lines to detach from the pinning centers, which will lead to a finite resistance, a broadened $R(B)$-curve and a lower value of B_{c2} [206]. This effect has been observed for instance in the hexagonal superconductor MgB_2 by rotating B with respect to I in the basal plane [208]. For a current density 30 A/cm^2, the two-fold anisotropy obtained just below $T_c = 36$ K is small, ~ 8 % [208]. In our transport experiments the current densities are ≤ 0.4 A/cm^2 and we did not detect a significant effect on the

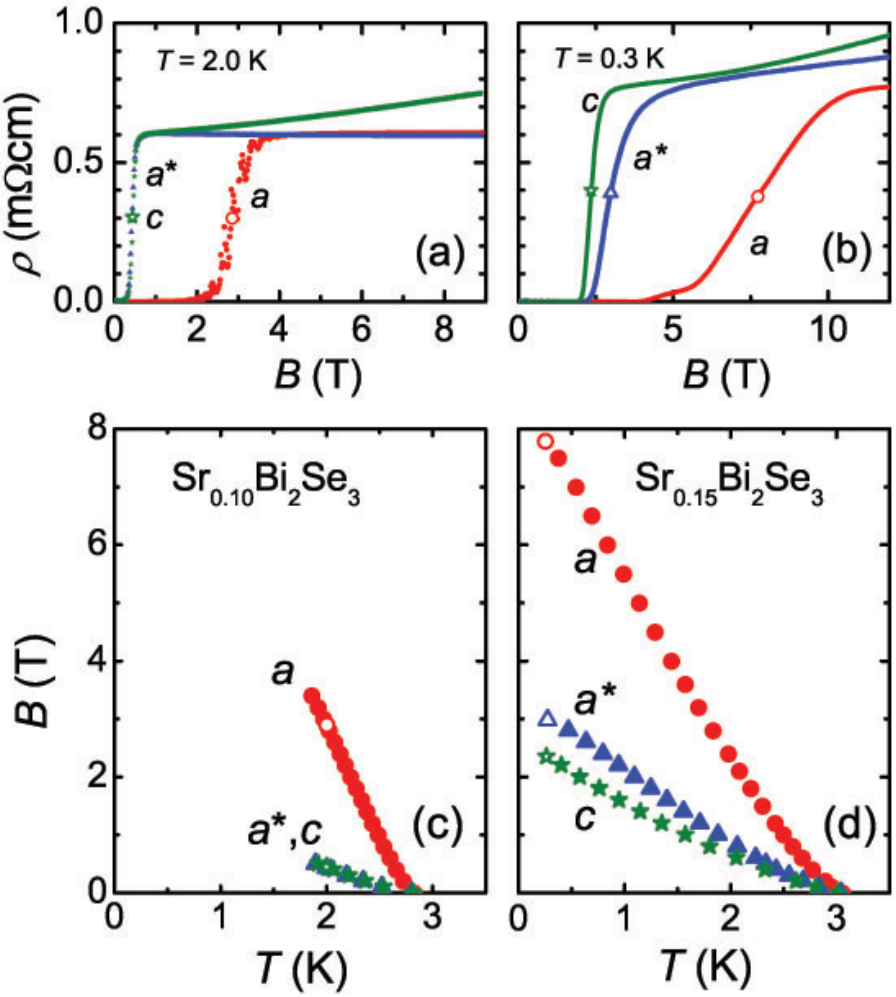

Figure 7.3: *Upper critical field of $Sr_xBi_2Se_3$. Panel (a) and (b): Resistance of $Sr_xBi_2Se_3$ as a function of $B \parallel a$, a^* and c, for $x = 0.10$ and 0.15, respectively. The open symbols indicate the midpoints of the transitions to the normal state. Panel (c) and (d): B_{c2} obtained for $B \parallel a$, a^* and c, for $x = 0.10$ and 0.15, respectively. Solid symbols from midpoints of $R(T)$-curves in fixed B. Open symbols from $\rho(B)$ at fixed T. In the experiments for $x = 0.15$ the crystal was not mounted on the rotator but oriented by eye, which adds some inaccuracy as regards field alignment. The current direction was always along the a-axis, with a precision of several degrees.*

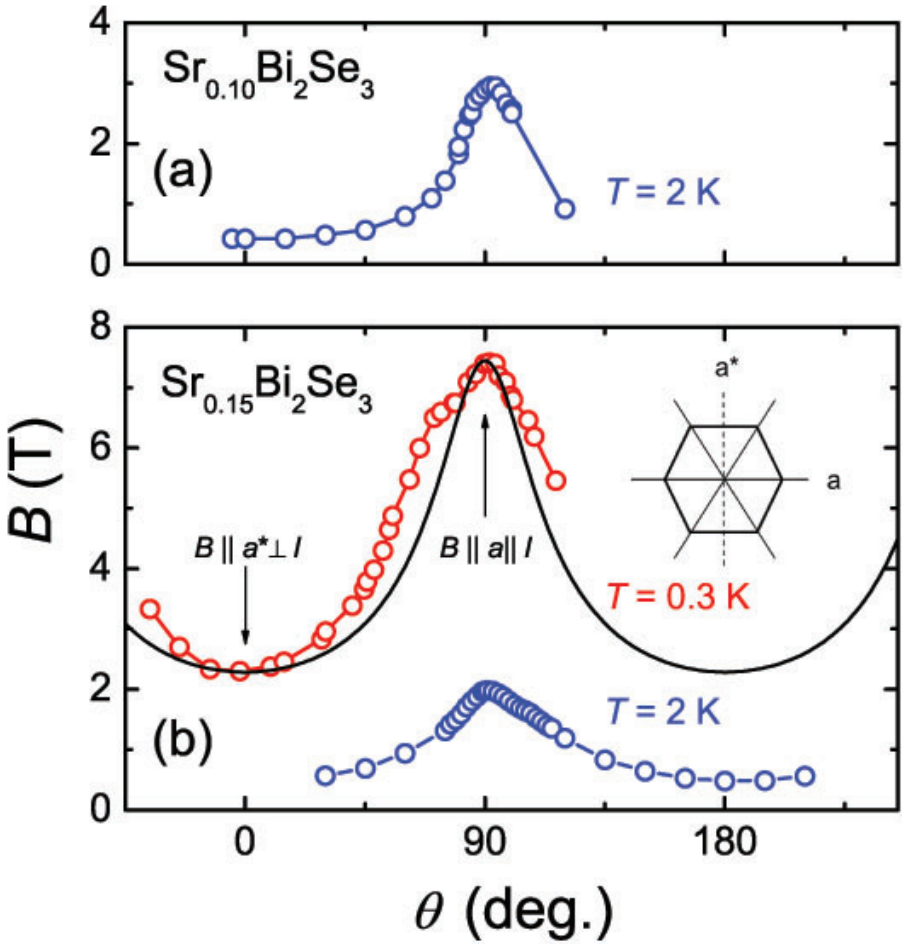

Figure 7.4: *Angular variation of B_{c2} of $Sr_xBi_2Se_3$ in the basal plane. Panel (a) and (b): Angular variation of B_{c2} in the basal plane (aa^*-plane) for $x = 0.10$ and 0.15, respectively, at temperatures as indicated. The data are obtained from $R(B)$ measurements at fixed T. The angle $\theta = 0°$ corresponds to $B \parallel a^* \perp I$ and $\theta = 90°$ to $B \parallel a \parallel I$. The solid black line in panel (b) represents $B_{c2}(\theta)$ for an anisotropic effective mass model with two-fold symmetry and $\gamma = 3.2$ (see text). The a and a^* directions in the hexagonal basal plane are defined as in the figure in the upper right corner of panel (b).*

resistance when the current density was varied close to T_c (see **Figure** A.6 in **Appendix** A). Also, when flux flow has a significant contribution, one expects the $R(B)$-curves for $B \perp I$ to be broader than the curves for $B \parallel I$. However, we observe the reverse (see **Figures** 7.3(a),(b)). Moreover, the anisotropy is still present at $T/T_c = 0.1$ and is much larger (of the order of 300 %, see **Figure** 7.4) than can be expected on the basis of flux flow. In order to further rule out the influence of the current direction we have investigated $B_{c2}(\theta)$ in the basal plane with the transport current perpendicular to the layers ($I \parallel c$) and thus keeping $B \perp I$ (see **Figure**. A.8 in **Appendix** A). The angular variation of the resistance, measured in this geometry using a two-probe method, is similar to that reported in **Figure** 7.1. Thus the two-fold anisotropy in B_{c2} is also present for the B-field in the aa^*-plane and the current along the c-axis.

Next we address whether the variation of B_{c2} in the basal plane can be attributed to the anisotropy of the effective mass. Within the Ginzburg-Landau model [204, 209] the anisotropy of B_{c2} is attributed to the anisotropy of the SC coherence length, ξ, which in turn relates to the anisotropy of the effective mass. For a layered superconductor the anisotropy ratio $\gamma^{an} = B_{c2}^{\parallel}/B_{c2}^{\perp} = \sqrt{M/m}$ [205]. Here m and M are the effective masses $\parallel$ and $\perp$ to the layers. In the rhombohedral structure $m = m_a = m_{a^*}$ and $M = m_c$, where the subscripts a, a^* and c refer to the effective masses for the energy dispersion along the main orthogonal crystal axes (*i.e.* in the hexagonal unit cell). For a field rotation in the aa^*-plane $B_{c2}^{\parallel}$ is in general isotropic, since $m_a \approx m_{a^*} (< m_c)$. For a 3D anisotropic superconductor the angular variation $B_{c2}(\theta)$ in a principal crystal plane can be expressed as $B_{c2}(\theta) = B_{c2}(0^\circ)/(\cos^2\theta + \gamma^{-2}\sin^2\theta)^{1/2}$, where $\gamma = B_{c2}(90^\circ)/B_{c2}(0^\circ)$. To provide an estimate of γ for $Sr_{0.15}Bi_2Se_3$, we compare in **Figure** 7.4(b) the measured $B_{c2}(\theta)$ with the angular variation in the anisotropic effective mass model (solid line). We obtain $B_{c2}(0^\circ) = 2.3$ T, $B_{c2}(90^\circ) = 7.4$ T and $\gamma = 3.2$. The effective mass ratio $m_{a^*}/m_a = \gamma^2$ [209] would then attain the large value of 10.2. As we show below, this is not compatible with the experimental Fermi-surface determination.

The Fermi surface of n-doped Bi_2Se_3, with a typical carrier concentration $n \sim 2 \times 10^{19}$ cm^{-3} representative for the SC $Sr_xBi_2Se_3$ crystals [61, 201], has been investigated by the Shubnikov - de Haas effect [61, 210, 211]. It can be approximated by an ellipsoid of revolution with the longer axis along the k_c-axis. A trigonal warping of the Fermi surface due to the rhombohedral symmetry has been detected, but the effect is small: the variation of the effective mass in the basal plane amounts to a few % only [210]. This also explains why $R(\theta)$ in the normal state (**Figure** 7.1(a)), does not show a $2\pi/3$ periodicity superimposed on the two-fold symmetry induced by the current. Clearly, the two-fold symmetry (**Figure** 7.4), while three fold is expected, and the calculated large ratio m_{a^*}/m_a using the Ginzburg-Landau model are at variance with the experimental Fermi-surface determination [210] and we discard this scenario.

We remark that the overall temperature variation $B_{c2}(T)$ reported in **Figure** 7.3(d) is at variance with the standard BCS behaviour for a weak-coupling spin-singlet SC [181]. All the curves show an upward curvature below T_c, followed by a quasi-linear behaviour down to the lowest temperatures. Furthermore, for $B \parallel a$, $B_{c2}(T \to 0)$ largely exceeds the Pauli limit $B^P(T \to 0) = 1.86 \times T_c \approx 5.6$ T for a spin-singlet SC [212]. This may point to an odd-parity component in the SC order parameter. Nagai (Ref. [207]) and Fu (Ref. [125]) recently proposed a model for odd parity polarized spin-triplet SC developed in the context of $Cu_xBi_2Se_3$, and investigated the experimental consequences of Δ_4 pairing in the two-orbital model [197]. Here, SC is described by an odd-parity two-dimensional representation, E_u, where the attractive potential pairs two electrons in the unit cell to form a spin triplet, *i.e.* a linear combination of $c_{1\uparrow}c_{2\uparrow}$ and $c_{1\downarrow}c_{2\downarrow}$. The indices 1,2 refer to the two orbitals and the arrows to the spin. The Δ_4 state has zero-total

spin along an in-plane direction $\mathbf{n} = (n_x, n_y)$ that is regarded as a nematic director and breaks rotational symmetry. By taking into account the full crystalline anisotropy in the Ginzburg-Landau model, it can be shown that $\mathbf{n}$ is pinned to a direction in the basal plane. For $\mathbf{n} = \hat{\mathbf{x}}$, point nodes in the SC gap are found along $\hat{\mathbf{y}}$, whereas for $\mathbf{n} = \hat{\mathbf{y}}$ two gap minima occur at $\pm k_F\hat{\mathbf{x}}$ [125]. Our B_{c2}-data can be interpreted as reflecting a strongly anisotropic SC gap function. The SC coherence length, ξ, along the main axes can be evaluated from the Ginzburg-Landau relations $B^a_{c2} = \Phi_0/(2\pi\xi_{a^*}\xi_c)$, $B^{a^*}_{c2} = \Phi_0/(2\pi\xi_a\xi_c)$ and $B^c_{c2} = \Phi_0/(2\pi\xi_a\xi_{a^*})$. Here Φ_0 is the flux quantum. With the experimental B_{c2}-values, taken at $T/T_c = 0.1$ in **Figure** 7.3(d) for $x = 0.15$, we calculate $\xi_a = 19.6$ nm, $\xi_{a^*} = 7.6$ nm and $\xi_c = 5.4$ nm. Interpreting ξ as the Cooper-pair size, this implies that the pairing interaction is strongest along the a^* and c-axis, and weakest along the a-axis. The observation that $\xi_a > \xi_{a^*} \approx \xi_c$, is in agreement with a gap structure with $\mathbf{n} = \hat{\mathbf{y}}$. On the other hand, in the Δ_4 pairing model rotational symmetry breaking due to nematic order is a property of the SC state, while B_{c2} probes the transition to the normal state and therefore should retain the hexagonal symmetry of the crystal lattice [213, 214]. This indicates a more intricate scenario. We remark that rotational symmetry breaking in the spin system has been observed by Nuclear Magnetic Resonance (NMR) in the related superconductor $Cu_xBi_2Se_3$, which is considered to provide solid evidence for a spin-triplet state [126].

Yet another interesting possibility is a self-organized structural stripiness in the optimum for superconductivity due to ordering of Sr atoms in the Van der Waals gaps. This could naturally lead to an anisotropy of B_{c2} when measured for a current in the basal plane, because of an effective reduced dimensionality. The higher B_{c2}-values will then be found for $B \parallel I$ along the stripes. On the other hand, for I perpendicular to the layers the basal-plane anisotropy of B_{c2} is found as well (see **Appendix** A). This calls for a detailed compositional and structural characterization of $Sr_xBi_2Se_3$ by techniques such as Electron Probe Microprobe Analysis (EPMA) or Transmission Electron Microscopy (TEM). Notice that in $Cu_xBi_2Se_3$ crystals EPMA has revealed that the Cu concentration shows variations on the sub-mm scale, which gives rise to SC islands [215]. Moreover, a STM study reports an oscillatory behaviour of the Cu pair distribution function due to screened Coulomb repulsion of the intercalant atoms [216].

In conclusion, we have investigated the angular variation of the upper critical field of superconducting crystals of $Sr_xBi_2Se_3$. The measurements reveal a striking two-fold anisotropy of the basal-plane B_{c2}. The large anisotropy cannot be explained with the anisotropic effective mass model or the variation of B_{c2} caused by flux flow. We have addressed two alternative explanations: (i) unconventional superconductivity, with an odd-parity triplet Cooper-pair state (Δ_4 pairing), and (ii) self-organized striped superconductivity due to preferential ordering of Sr atoms. The present experiments and results provide an important benchmark for further unravelling the superconducting properties of the new candidate topological superconductor $Sr_xBi_2Se_3$.

Appendix A

Appendix: Rotational symmetry breaking in $Sr_xBi_2Se_3$

A.1 Sample shape and demagnetization factor

The basal-plane transport experiments were performed on thin-bar shaped samples with the current along the long axis. The dimensions of the $Sr_{0.10}Bi_2Se_3$ crystal are $1.3 \times 5.5 \times 0.32$ mm^3 and of the $Sr_{0.15}Bi_2Se_3$ crystal $1.3 \times 2.3 \times 0.35$ mm^3. We have estimated the demagnetization factor N for the field along and perpendicular to the long axis (see Ref. [217]). For $Sr_{0.10}Bi_2Se_3$ we estimate $N_{\|} = 0.05$ and $N_{\perp} = 0.213$, and for $Sr_{0.15}Bi_2Se_3$ $N_{\|} = 0.12$ and $N_{\perp} = 0.20$. For a Type II superconductor a demagnetization factor $N \neq 0$ gives rise to a correction of the internal field $H_{in} = (B_{app}/\mu_0)/(1 + \chi N)$. We conclude these corrections are relatively small for our crystals and we neglect demagnetization effects. Neglecting the effect of N does not have a significant effect on the derived values of the large basal-plane anisotropy of the upper critical field B_{c2}.

A.2 Sample characterization: resistance and ac-susceptibility

The temperature variation of the resistivity, $\rho(T)$, of several $Sr_xBi_2Se_3$ crystals has been measured with a standard 4-probe low-frequency ac-technique in the PPMS. Typical resistivity traces, taken in the temperature range 2-300 K, are shown in **Figure** A.1. The resistance shows a metallic behavior. The $\rho(T)$-values at low temperature amount to 0.60 and 0.75 mΩcm for x = 0.10 and 0.15, respectively, and are in good agreement with the values reported previously (See Refs. [61, 201]). The superconducting transition temperatures as determined by the midpoints of the transitions are 2.84 K and 2.95 K for x = 0.10 and 0.15, respectively. The ac-susceptibility,χ_{AC}, was measured in a driving field

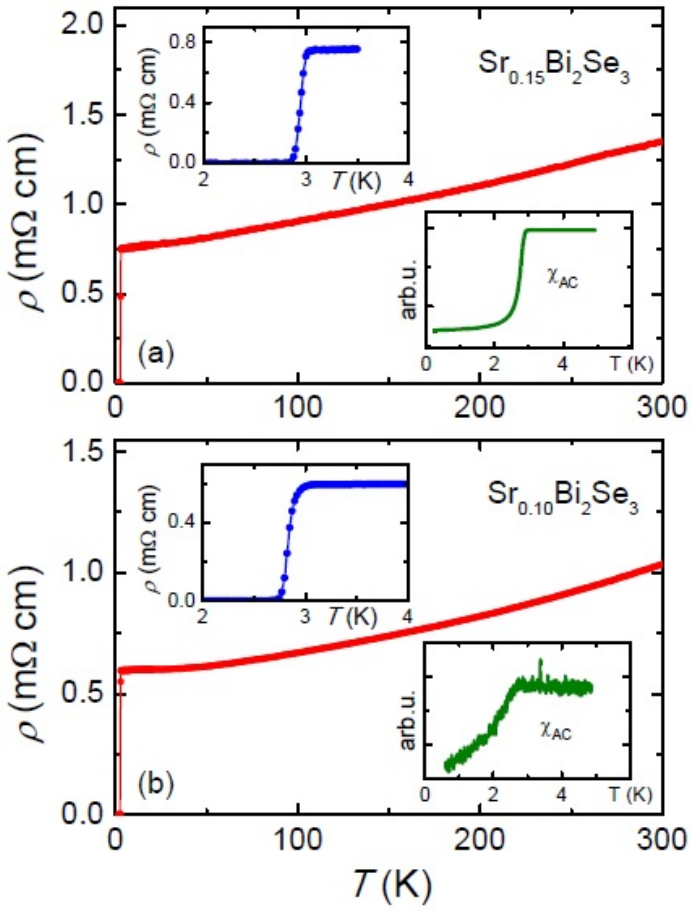

Figure A.1: *Panel (a) and (b): Resistivity of $Sr_xBi_2Se_3$ single crystals with x = 0.15 and 0.10, respectively. Upper insets: zoom of the superconducting transition. Lower insets: ac-susceptibility around the superconducting transition.*

of 0.026 mT in the 3-Helium cryostat for several crystals with different sizes. The χ_{AC} data yield superconducting volume fractions of 5-40 % for x = 0.10 and 80 % for 0.15, respectively.

A.3 Superconducting transition of $Sr_{0.10}Bi_2Se_3$ in magnetic field

The suppression of the superconducting state by a magnetic field was measured by the resistance as a function of temperature in fixed magnetic fields. The data for $Sr_{0.10}Bi_2Se_3$ taken in the PPMS down to a temperature of 2 K are shown in **Figure** A.2. The superconducting transition temperatures are determined by the midpoints of the transitions.

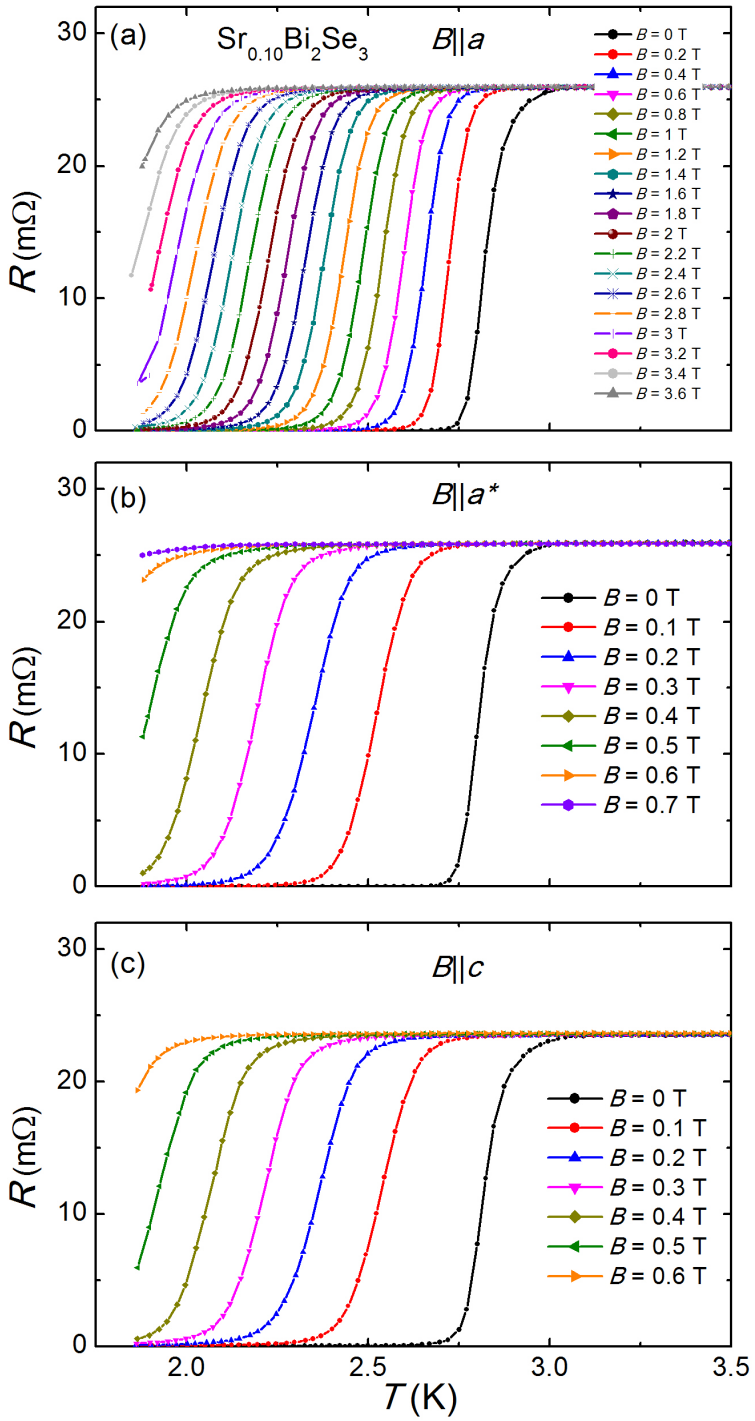

Figure A.2: *Superconducting transition of $Sr_{0.10}Bi_2Se_3$ measured in fixed magnetic fields as indicated. In panel (a), (b) and (c) the B-field is applied along the a, a^* and c-axis, respectively.*

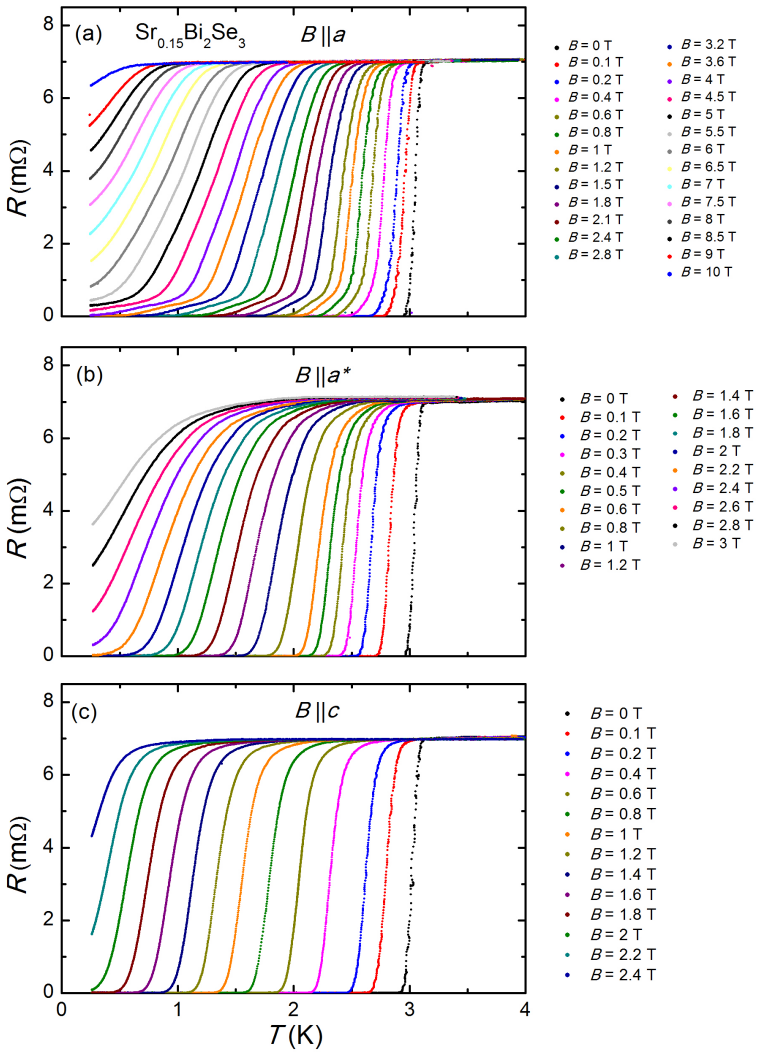

Figure A.3: *Superconducting transition of $Sr_{0.15}Bi_2Se_3$ measured in fixed magnetic fields as indicated. In panel (a), (b) and (c) the B-field is applied along the a, a^* and c-axis, respectively.*

A.4 Superconducting transition of $Sr_{0.15}Bi_2Se_3$ in magnetic field

The suppression of the superconducting state by a magnetic field was measured by the resistance as a function of temperature in fixed magnetic fields. The data for $Sr_{0.15}Bi_2Se_3$ taken in the 3-Helium cryostat down to 0.3 K are shown in **Figure** A.3. The superconducting transition temperatures are determined by the midpoints of the transitions. For $B\|a$ the resistance develops a small tail towards $R = 0$, which is attributed to a sample inhomogeneity.

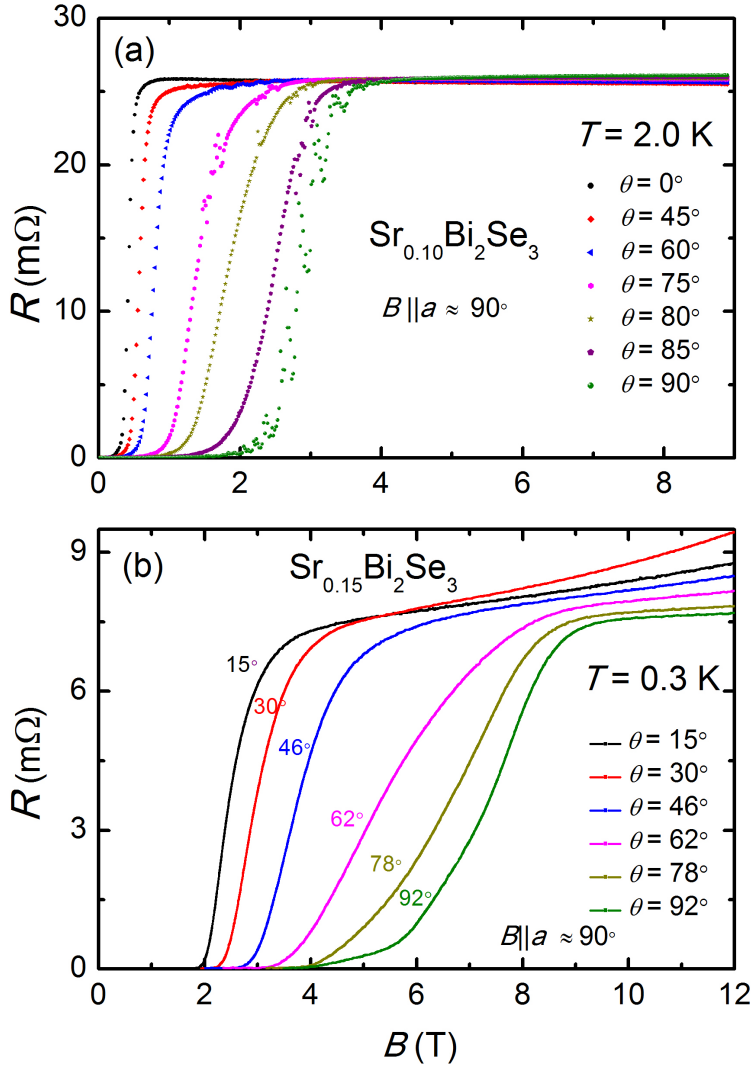

Figure A.4: *Panel (a) and (b): Angular variation of the magnetoresistance of $Sr_{0.10}Bi_2Se_3$ at 2.0 K and of $Sr_{0.15}Bi_2Se_3$ at 0.3 K, respectively. The angle $\theta = 0°$ corresponds to $B \perp I$. The angle $\theta = 90°$ corresponds to $B \| I$, which is also close to $B \| a$.*

A.5 Angular variation of the resistance as a function of magnetic field

The angular variation of $R(B)$ of the $Sr_{0.10}Bi_2Se_3$ crystal was measured in the PPMS at $T = 2.0$ K, whereas data for $Sr_{0.15}Bi_2Se_3$ were taken at $T = 2.0$ K in the PPMS and at $T = 0.3$ K in the 3-Helium cryostat. Selected $R(B)$ curves are shown in **Figure** A.4. The midpoints of the transitions to the normal state determine $T_c(B)$ and have been used to construct **Figure** 7.4 in **Chapter** 7.

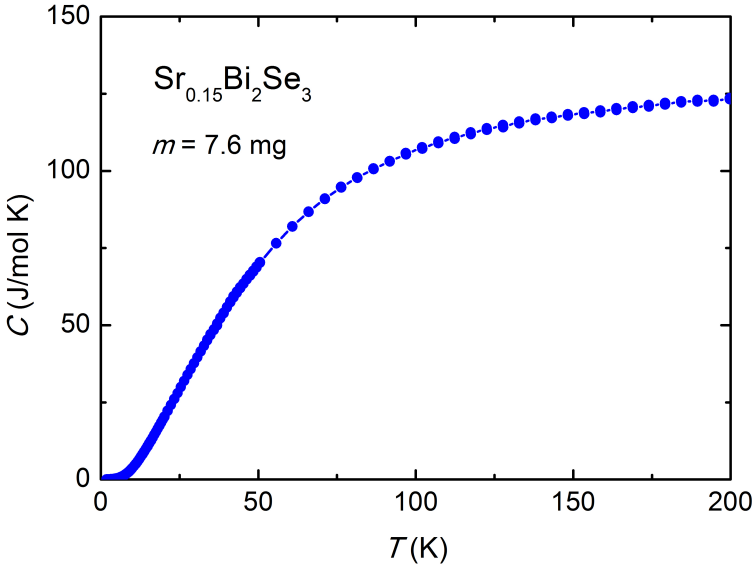

Figure A.5: *Specific heat of $Sr_{0.15}Bi_2Se_3$ as a function of temperature*

A.6 Specific heat

The specific heat of a $Sr_{0.15}Bi_2Se_3$ crystal with mass 7.6 mg was measured by the relaxation method using the Heat Capacity Option in the PPMS in the temperature range 2-300 K. In **Figure** A.5 the data from 2 to 200 K are shown. No sign of a structural transition is found in this temperature range. The data between 200 and 300 K (not shown) show some irregularities that can be attributed to the Apiezon N grease that was used to fix the sample to the specific heat platform.

A.7 Current dependence of $R(\theta)$

The angular variation $R(\theta)$ of the $Sr_{0.10}Bi_2Se_3$ crystal was investigated for currents ranging from 0.1 to 2 mA at $T = 2$ K and $B = 1$ T. No significant changes are observed for currents $I \leq 1$ mA as shown in **Figure** A.6. The small increase in resistance for the largest current $I = 2$ mA is attributed to Joule heating.

A.8 Transport measurements with the current along the c-axis

The angular variation $R(\theta)$ in the basal plane was measured with the current along the c-axis for $Sr_{0.15}Bi_2Se_3$. In this geometry the B-field is always perpendicular to the measuring current. Two circular gold electrodes (diameter 60 μm) were evaporated exactly opposite to each other on the basal-plane surfaces of a thin $Sr_{0.15}Bi_2Se_3$ single crystal (label #2) with dimensions $6 \times 3 \times 0.5$ mm^3. Four copper wires (25 μm) that served as current

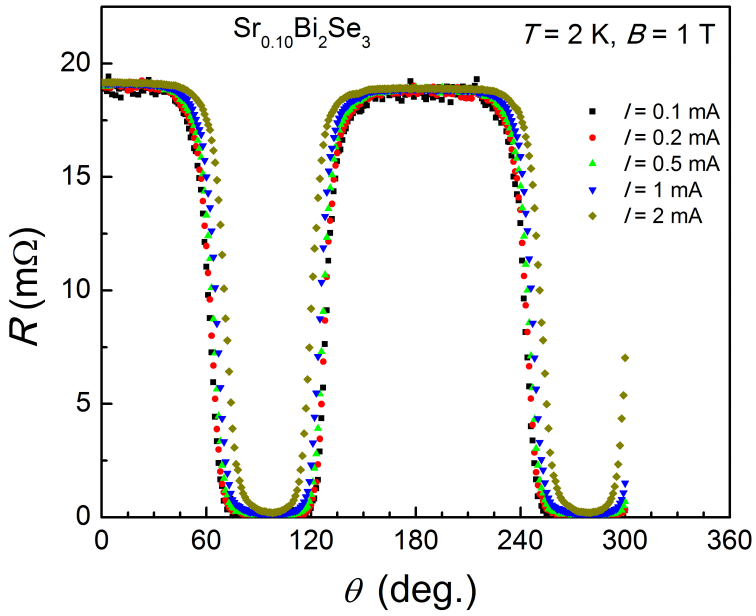

Figure A.6: *Angular variation $R(\theta)$ of $Sr_{0.10}Bi_2Se_3$ measured at $T = 2$ K and $B = 1$ T for currents ranging from 0.1-2 mA as indicated.*

and voltage leads were attached to the electrodes with silver paste, but effectively the resistance was measured in a two-point configuration. Data were taken in the PPMS in the temperature range 2-200 K with a current $I = 1$ mA, see **Figure** A.7. Superconductivity results in a drop of 12% of the resistance. In this measurement configuration the transition is relatively broad, The onset temperature for superconductivity for this crystal is 2.75 K. The angular variation for $B = 0.5$ T in the basal plane is shown in **Figure** A.8 in the T-range 2.0-3.5 K. The two-fold anisotropy is the same as in the measurements with the current in the basal plane for $x = 0.10$ (**Figure** 7.1 in the **Chapter** 7). For $B \perp I \| c$ the lowest resistance values and the largest values for B_{c2} are found for the B-field along the long direction of the sample. After the measurements gold electrodes were evaporated at a different place opposite to each other on the basal plane surfaces and the experiment was repeated with essentially the same results and conclusions.

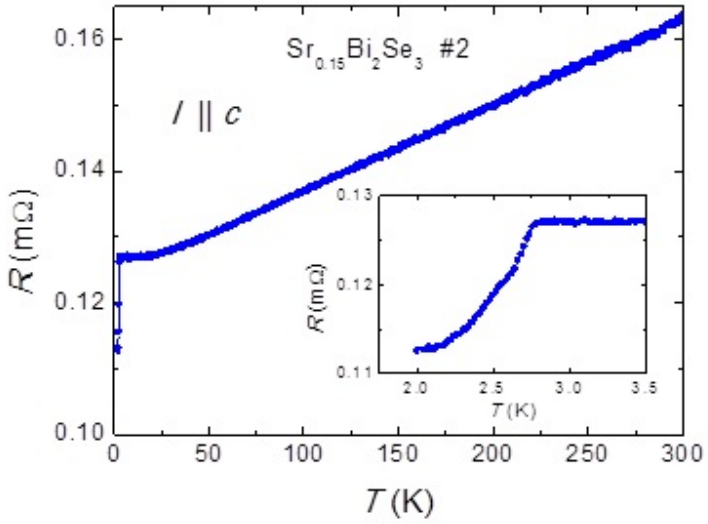

Figure A.7: *Resistance of $Sr_{0.15}Bi_2Se_3$ for $I \| c$-axis, measured in a two-point configuration. Superconductivity results in a drop of 12% of the resistance. The residual resistance of 0.112 mΩ at 2.0 K is due to the silver paste and the copper wires.*

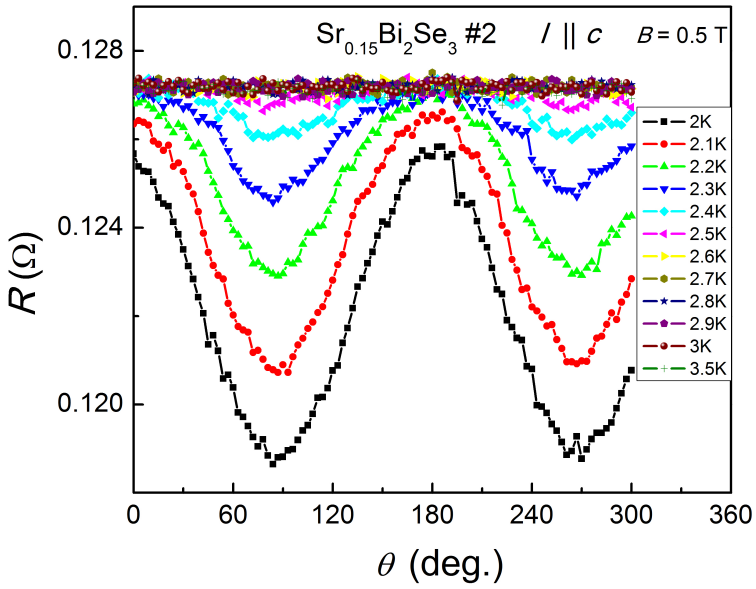

Figure A.8: *Angular variation $R(\theta)$ in the basal plane for $I \| c$-axis for $B = 0.5$ T at temperatures as indicated. The lowest curve (black symbols) is at 2.0 K. The anisotropy is two-fold. The lowest resistance values and thus the largest values for B_{c2} are found for the B-field along the long direction of the sample.*

Summary

Topological insulators have sparked ample interest in the condensed matter physics research community in recent years due to their theoretical research value for novel quantum phenomena and potential practical applications, like in spintronics. However, a long-standing problem in the branch of the transport research field is that the bulk conductivity overwhelms the charge transport and therefore hinders the access to the topological surface states in most current topological insulator materials. The first main topic of this thesis is therefore to reduce the contribution of the bulk conductivity in the prototypical topological insulator material $Bi_{2-x}Sb_xTe_{3-y}Se_y$ (BSTS), then detect the topological surface states and investigate their transport properties. As the notion of topological insulators extends to topological superconductors, topological superconductors have become a hot topic as well, notably because they could harbor Majorana zero modes at the surface. Majorana zero modes are predicted to provide a new route to fault tolerant quantum computation. Therefore, the search for topological superconductors and the determination of their intrinsic properties is an important research topic. The second main topic of this thesis is to study two candidate topological superconductors ErPdBi and $Sr_xBi_2Se_3$.

In Chapter 2, we present the preparation and characterization of the crystals studied in this thesis, i.e. BSTS (Chapter 4, 5), ErPdBi (Chapter 6) and $Sr_xBi_2Se_3$ (Chapter 7). The BSTS and $Sr_xBi_2Se_3$ crystals were grown by the Bridgman technique, while ErPdBi was prepared by the flux method. The phase homogeneity was investigated by X-ray diffraction and Electron Probe Micro Analysis. The single crystallinity was verified by back-scattering Laue diffraction. Besides we describe the experimental facilities used for investigation of the transport and magnetic properties of these crystals, especially, the Physical Property Measurement System (PPMS) Dynacool. Special attention is given to the Resistivity option, Horizontal Rotator option, VSM option and ACMS II option.

In Chapter 3, we present the general theoretical background relevant to the thesis research. Topological insulators are distinguished by their $\mathbb{Z}_2$ topological invariant, which in centrosymmetric materials can be calculated from the parity of the occupied valence bands at the time-reversal invariant points in k space. Band inversion originating from strong

spin-orbit coupling is the root-cause in topological insulators and gives rise to topological edge or surface states with unique properties such as spin-momentum locking and a π Berry phase. To examine their intrinsic insulating behavior in terms of electrical transport, simple criteria given by Mott and Ioffe-Regel with a critical value of the carrier density $N_{BD} = 3 \times 10^{14}$ cm^{-3} and $k_F\ell \sim 1$, respectively, are introduced. Also, band bending effects which affect the transport properties are briefly discussed. Next the theoretical background of the weak anti-localization effect (WAL) and the Shubnikov de Haas effect (SdH) are presented. WAL and SdH are used to characterize the topological surface states in BSTS. Finally, the criterion for identification of time-reversal invariant topological superconductors with inversion symmetry is presented, that is, (i) the superconducting pair wave function has odd-parity symmetry and the superconducting gap is fully gapped; (ii) the Fermi surface encloses an odd number of time reversal invariant momenta.

In Chapter 4, an extensive investigation of the bulk-insulating properties of BSTS single crystals is presented. In order to obtain intrinsic bulk-insulating transport behavior, numerous $Bi_{2-x}Sb_xTe_{3-y}Se_y$ single crystals have been grown around $x = 0.5$ and $y = 1.3$ with composition steps in x of 0.02 and in y of 0.1. Through measurements of resistance and Hall effect, we show that the composition $Bi_{1.46}Sb_{0.54}Te_{1.7}Se_{1.3}$ has a record-high resistivity and a low carrier density. Since the bulk and surface channels connect in parallel, the surface transport can be enhanced by reducing the sample thickness. We performed resistivity measurements for crystals with different thicknesses and analyzed the measured resistivity at low temperature using a parallel resistor model. The analysis shows that when the sample thickness is reduced to 1 μm the surface contribution to the electrical transport amounts to 97 %. Therefore, devices fabricated with submicrometer thickness are sufficiently bulk insulating to exploit the topological surface states by transport techniques. This is further examined by magnetoresistance measurements on an exfoliated BSTS nanoflake that show the weak antilocalization effect. The 2D nature of the weak antilocalization is confirmed by the collapse of the magnetoconductance data as a function of the perpendicular magnetic field component. The 2D weak antilocalization is analyzed within the Hikami-Larkin-Nagaoka model that gives the fit parameter $\alpha \simeq -1$ as expected for conduction via a pair of topological surface states. No Rashba-split non-topological surface states appear in our $Bi_{1.46}Sb_{0.54}Te_{1.7}Se_{1.3}$ crystals, which is in agreement with ARPES data recorded under band-bent conditions.

In Chapter 5, we present a magnetotransport study on low-carrier concentration crystals of the topological insulator $Bi_{2-x}Sb_xTe_{3-y}Se_y$ with $(x, y) = (0.50, 1.3)$ and $(x, y) = (0.54, 1.3)$. Shubnikov - de Haas oscillations with a frequency of 63 T and 33 T for $(x, y) = (0.50, 1.3)$ and $(x, y) = (0.54, 1.3)$ respectively are observed in high magnetic fields. When tilting the sample with respect to the field, the oscillations collapse as a function of the perpendicular magnetic field component, which confirms their 2D origin. The oscillations are analyzed within the framework of the Lifshitz-Kosevich theory and

important transport parameters, such as the cyclotron mass, the mean free path and the mobility are deduced. The Landau level plots are obtained and the resulting phase factors are extracted from the extrapolated x-axis crossing of the linear Landau level plot. The resulting phase factors deviate from the ideal value 0.5 as expected for topological surface states. The deviation is analyzed with a model incorporating a non-ideal Dirac dispersion, that was measured directly using ARPES, and a Zeeman coupling-term with large g_s-factor for $(x, y) = (0.50, 1.3)$. Based on the band parameters deduced from ARPES measurements carried out on a sample prepared from the same single-crystalline batch, the SdH oscillations can be attributed to topological surface states with an electron spin g-factor $g_s = 70$ or -54 as fitting parameter in the LL plot model. To estimate the surface contribution, the Hall resistivity for $(x, y) = (0.50, 1.3)$ is fitted within a two-band (bulk + surface) model by combining the carrier density and mobility for the topological surface states from the SdH data. It shows that the surface contribution to the total electrical transport amounts to around 32 % in our $Bi_{1.5}Sb_{0.5}Te_{1.7}Se_{1.3}$ crystal with a thickness of 40 μm.

In Chapter 6, we present the discovery of superconductivity at T_c = 1.22 K and antiferromagnetic order at T_N = 1.06 K in the non-centrosymmetric half Heusler compound ErPdBi, based on electrical transport, ac-susceptibility and dc-magnetization measurements. Bulk superconductivity is inferred from a diamagnetic screening volume fraction of around 90%. The upper critical field, B_{c2}, has an unusual quasi-linear temperature variation which reaches a value of 1.6 T for $T \to 0$. Antiferromagnetic order sets in below T_c and is suppressed by a magnetic field at $B_M \sim 2.5$ T for $T \to 0$. The combination of superconductivity and AFM order is unusual. Possibly, the ordering phenomena occur in different electron subsystems: superconductivity in the low-carrier hole band and local moment magnetism due to Er $4f$-moments. However, since $T_N \simeq T_c$, and ErPdBi lacks inversion symmetry, the interplay of superconductivity and magnetism might give rise to a complex ground state. Moreover, ErPdBi has an inverted band order indicating its non-trivial topological nature according to electronic structure calculations. Together with the possibility of even and odd parity mixed superconducting states it is a promising candidate for topological superconductivity.

In Chapter 7, we present the discovery of nematic superconductivity in $Sr_xBi_2Se_3$ crystals. We present the investigation of the upper critical field of superconducting $Sr_xBi_2Se_3$ crystals with T_c = 3 K. When the magnet field is rotated in the basal plane, the angular dependent magnetoresistance curves and the upper critical field B_{c2} both reveal a striking two-fold anisotropy. For $Sr_{0.15}Bi_2Se_3$, the upper critical fields B_{c2} along the two orthogonal directions in the basal plane (a and a^*) are 7.4 T and 2.3 T, respectively, at T = 0.25 K. The effect of flux flow caused by the Lorentz force and the anisotropic effective mass Ginzburg-Landau model both fail to explain the large anisotropy. However, the two-fold anisotropy is in agreement with a recently published theoretical model for nematic super-

conductivity, i.e. unconventional superconductivity with an odd-parity triplet Cooper-pair state (Δ_4 pairing). However, a structural origin such as a self-organized striped superconductivity due to preferential ordering of Sr atoms cannot be excluded at the moment. The present experiments and results provide an important benchmark for further unraveling the superconducting properties of the new topological superconductor $Sr_xBi_2Se_3$.

Samenvatting

Sinds een aantal jaren vormen topologische isolatoren een belangrijk onderzoeksthema in het gebied van de natuurkunde van de gecondenseerde materie, enerzijds vanwege hun waarde voor het theoretisch onderzoek aan nieuwe vormen van quantum materie en anderzijds door toekomstige toepassingen in bijvoorbeeld spintronica. Een zeer actueel probleem in het transportonderzoek aan de huidige topologische materialen is echter dat de geleiding van de bulk overheerst, wat het onderzoek naar transport van lading en spin in de topologische toestanden aan het oppervlak belemmert. Een eerste hoofdonderwerp in dit proefschrift is daarom het verminderen van de bulkgeleiding in de archetypische topologische isolator $Bi_{2-x}Sb_xTe_{3-y}Se_y$ (BSTS), het detecteren van de oppervlakte toestanden en het meten van hun transporteigenschappen. Aangezien het concept topologische isolator uitgebreid kan worden naar supergeleiding, staan ook topologische supergeleiders sterk in de belangstelling, in het bijzonder omdat de supergeleidende toestand aan het oppervlak Majorano zero-modes kan herbergen. Van Majorano zero-modes is voorspeld dat het gebruik er van als quantum bit een belangrijke nieuwe route oplevert voor berekeningen in quantum computers. Het zoeken naar nieuwe topologische supergeleiders en het meten van hun eigenschappen is een prominent onderzoeksonderwerp. Het tweede hoofdonderwerp van dit proefschrif is derhalve het onderzoek naar de kandidaat topologische supergeleiders ErPdBi en $Sr_xBi_2Se_3$.

In hoofdstuk 2 presenteren we de bereidingswijze en karakterisatie van de éénkristallen bestudeerd in dit proefschrift: BSTS (Hoofdstuk 4 en 5), ErPdBi (Hoofdstuk 6) en $Sr_xBi_2Se_3$ (Hoofdstuk 7). De BSTS en $Sr_xBi_2Se_3$ kristallen zijn gegroeid met de Bridgman methode, terwijl ErPdBi is bereid met de flux methode. De fasehomogeniteit is onderzocht door middel van Röntgendiffractie en Electron Probe Micro Analysis. Laue diffractie is gebruikt om de éénkristallijne kwaliteit te controleren. Daarnaast beschrijven we de experimentele opstellingen gebruikt om de transport en magnetische eigenschappen van de kristallen te meten, met name de Physical Property Measurement System (PPMS) Dynacool. Speciale aandacht gaat uit naar de Weerstand optie, de Horizontale Rotator optie, de VSM optie en de ACMS II optie.

In Hoofdstuk 3 presenteren we de algemene theoretische achtergrond die relevant is voor het onderzoek beschreven in dit proefschrift. Topologische isolatoren worden gekenmerkt door hun $\mathbb{Z}_2$ topologische invariant, die in centrosymmetrische materialen berekend kan worden uit de pariteit van de bezette valentiebanden bij de tijdomkeerinvariante punten in de k-ruimte. Bandinversie veroorzaakt door sterke spin-baan koppeling ligt ten grondslag aan topologische isolatoren en de topologische rand of oppervlakte toestanden met unieke eigenschappen, zoals spin-momentum koppeling en de π Berry fase. Om de intrinsieke isolator eigenschappen in transport termen te bepalen, worden de criteria van Mott en Ioffe-Regel met een kritieke waarde voor de dichtheid van de ladingdragers $N_{BD} = 3 \times 10^{14}$ cm^{-3} en $k_F\ell \sim 1$, respectievelijk, geintroduceerd. Ook band-buigingseffecten die van invloed zijn op de transporteigenschappen worden kort bediscussieerd. Vervolgens wordt de theoretische achtergrond van het zwakke anti-localisatie effect (WAL) en het Shubnikov - de Haas effect (SdH) besproken. WAL en SdH worden gebruikt om de topologische oppervlakte toestanden van BSTS te karakteriseren. Als laatste wordt het identificatie criterium voor tijdomkeerinvariante topologische supergeleiders met inversie symmetrie gepresenteerd: (i) de supergeleidende paargolffunctie heeft een oneven pariteit en de supergeleidende energiekloof is overal open, en (ii) het Fermi oppervlak omsluit een oneven aantal tijdomkeerinvariante punten in de k-ruimte.

In Hoofdstuk 4 wordt een omvangrijke studie van de bulk-isolerende eigenschappen van BSTS éénkristallen gepresenteerd. Om intrinsiek bulk-isolerend transport te bereiken zijn een groot aantal $Bi_{2-x}Sb_xTe_{3-y}Se_y$ éénkristallen gegroeid, met samenstelling rond $x = 0.5$ en $y = 1.3$ met stappen in x van 0.02 en in y van 0.1. Uit weerstand- en Halleffectmetingen volgt dat de compositie $Bi_{1.46}Sb_{0.54}Te_{1.7}Se_{1.3}$ een record-hoge soortelijke weerstand heeft en tegelijkertijd een lage ladingdragersdichtheid. Aangezien het inwendige van het kristal (de bulk) en het oppervlak twee parallelle weerstandskanalen vormen, kan de transportcomponent van het oppervlak relatief versterkt worden door de dikte van het kristal te verminderen. Om dit te onderzoeken hebben we weerstandsmetingen uitgevoerd aan kristallen met verschillende diktes en de gemeten weerstand ganalyseerd met het parallelle-weerstanden model. De analyse laat zien dat als de dikte van het kristal gereduceerd is tot 1 μm, de bijdrage van het oppervlak aan de totale electrische geleiding 97 % bedraagt. Dus devices gefabriceerd met een submicrometer dikte zijn voldoende bulk isolerend om de topologische oppervlakte toestanden te benutten met gebruik van transport technieken. Dit is verder bestudeerd aan de hand van magnetoweerstandsexperimenten aan een geëxfolieerde BSTS nanoflake, waarin zwakke localisatie wordt waargenomen. Het 2D karakter van de zwakke loklaisatie wordt bevestigd door de universele magnetogeleidingscurves als functie van de loodrechte component van het mageteetveld. De 2D zwakke localisatie is geanalyseerd met het Hikami-Larkin-Nagaoka model dat een fit parameter $\alpha \simeq -1$ geeft, zoals verwacht voor geleiding ten gevolge van één paar topologische oppervlakte toestanden. Triviale Rashba-split oppervlakte toestanden zijn afwezig in onze

$Bi_{1.46}Sb_{0.54}Te_{1.7}Se_{1.3}$ kristallen, hetgeen in overeenstemming is met ARPES metingen onder band-buigingscondities.

In Hoofdstuk 5 presenteren we een hoog-veld magnetotransport studie van kristallen van de topologische isolator $Bi_{2-x}Sb_xTe_{3-y}Se_y$ met $(x, y) = (0.50, 1.3)$ en $(x, y) = (0.54, 1.3)$, met een lage ladingdragersconcentratie. Shubnikov - de Haas oscillaties zijn waargenomen in hoge magneetvelden met een frequentie van 63 T en 33 T voor $(x, y) = (0.50, 1.3)$ en $(x, y) = (0.54, 1.3)$, respectievelijk. Hoekafhankelijke metingen laten zien dat de oscillaties samenvallen als functie van de loodrechte component van het magneetveld. Dit bevestigt de 2D oorsprong van de oscillaties. De SdH oscillaties zijn geanalyseerd met de Lifshitz-Kosevich theorie en belangrijke transportparameters, zoals de cyclotron massa, de gemiddelde vrije weglengte en de mobiliteit zijn bepaald. Landau-niveau grafieken zijn verkregen en de fasefactoren zijn bepaald uit de lineaire extrapolatie naar de afsnijde met de x-as. De aldus verkregen fasefactoren wijken af van de waarde van 0.5 voorspeld voor een topologische oppervlakte toestand. De afwijking is voor $(x, y) = (0.50, 1.3)$ geanalyseerd met een Landau-niveau model met een niet ideale Dirac dispersie en een Zeeman term met een aanzienlijke electron-spin g-factor, g_s. Gebruikmakend van de electronband parameters verkregen uit ARPES metingen aan een deel van hetzelfde $(x, y) = (0.50, 1.3)$ kristal kunnen de SdH oscillaties toegeschreven worden aan topologische oppervlakte toestanden met g_s = 70 of -54 als fitparameter in het Landau-niveau model. Om de transportcomponent van de oppervlakte toestanden af te schatten, is de Hall weerstand voor $(x, y) = (0.50, 1, 3)$ geanalyseerd met een twee-banden (bulk + oppervlak) model door het combineren van de ladingdragersdichtheid en mobiliteit van de topologische oppervlakte toestanden uit de SdH data. De berekening geeft een bijdrage van het oppervlak aan de totale electrische geleiding van 32 % in het $Bi_{1.5}Sb_{0.5}Te_{1.7}Se_{1.3}$ kristal met een dikte van 40 μm.

In Hoofdstuk 6 presenteren we ontdekking van supergeleiding bij T_c = 1.22 K en anti-ferromagnetische ordening bij T_N = 1.06 K in de noncentrosymmetrische halve-Heusler verbinding ErPdBi, gebaseerd op metingen van de electrische weerstand, ac-susceptibiliteit en dc-magnetizatie. Uit het diamagnetische signaal kan geconcludeerd worden dat een volume fractie van 90 % van het kristal supergeleidend is. Het bovenste kritische veld, B_{c2}, heeft een ongebruikelijke quasi-lineaire temperatuurafhankelijkheid en bereikt een waarde van 1.6 T voor $T \to 0$. Antiferromagnetische ordening treedt in net beneden T_c en wordt onderdrukt met een magneetveld van $B_M \sim 2.5$ T voor $T \to 0$. Dat supergeleiding èn antiferromagnetisme tegelijkertijd bestaan is ongebruikelijk. Mogelijkerwijs worden beide ordeningsverschijnselen verorzaakt door verschillende electronsubsystemen: supergeleiding in de gaten geleidingsband met een lage ladingdragersconcentratie en lokaal-moment magnetisme door de magnetische $4f$ momenten van de Er atomen. Aangezien $T_N \simeq T_c$ en ErPdBi geen inversiesymmetrie heeft zou de wisselwerking tussen supergeleiding en magnetisme aanleiding kunnen geven tot een complexe grondtoestand. Daarnaast laten

berekeningen van de electronenstructuur zien dat ErPdBi een band-inversie heeft en dus een topologisch karakter. Dit, in combinatie met de mogelijkheid voor een even/oneven gemengde supergeleidende toestand, maakt ErPdBi tot een veelbelovende kandidaat voor topologische supergeleiding.

In Hoofdstuk 7 presenteren we de ontdekking van nematische supergeleiding in $Sr_xBi_2Se_3$. We beschrijven een experimentele studie van het bovenste kritische veld, B_{c2}, van supergeleidende $Sr_xBi_2Se_3$ kristallen met T_c = 3 K. Wanneer het magneetveld gedraaid wordt in het basisvlak blijken de hoekafhankelijke magnetoweerstandscurves en B_{c2} beide een opvallende tweevoudige anisotropie te vertonen. Voor een kristal met samenstelling $Sr_{0.15}Bi_2Se_3$ bereikt B_{c2} voor een magneetveld langs de twee orthogonale hoofdrichtingen in het basisvlak (a and a^*) een waarde van 7.4 T en 2.3 T, respectievelijk, bij T = 0.25 K. De effecten van flux flow op B_{c2} veroorzaakt door de Lorentzkracht en het Ginzburg-Landau model voor een anisotrope effectieve massa kunnen de gemeten anisotropie niet verklaren. Echter, een recent gepubliceerd model voor nematische supergeleiding, opgesteld voor de topologische supergeleider $Cu_xBi_2Se_3$, kan de metingen wel verklaren. Dit model betreft onconventionale supergeleiding met exotische triplet Cooper-paar toestanden (Δ_4 paring). Een structurele oorsprong van de tweevoudige anisotropie in B_{c2}, nl. een zelf-georganiseerde striped supergeleiding door een voorkeursordening van Sr atomen, kan echter niet uitgesloten worden. De huidige experimentele resultaten bieden een belangrijk referentiekader om de supergeleidende eigenschappen van deze nieuwe topologische supergeleider verder te ontrafelen.

Bibliography

[1] M. Z. Hasan and C. L. Kane. Colloquium: Topological insulators. *Rev. Mod. Phys.*, 82:3045–3067, 2010.

[2] J. E. Moore. The birth of topological insulators. *Nature*, 464:194–198, 2010.

[3] Xiao-Liang Qi and Shou-Cheng Zhang. Topological insulators and superconductors. *Rev. Mod. Phys.*, 83:1057–1110, 2011.

[4] K. V. Klitzing, G. Dorda, and M. Pepper. New method for high-accuracy determination of the fine-structure constant based on quantized hall resistance. *Phys. Rev. Lett.*, 45:494–497, 1980.

[5] D. J. Thouless, M. Kohmoto, M. P. Nightingale, and M. Den Nijs. Quantized hall conductance in a two-Dimensional periodic potential. *Phys. Rev. Lett.*, 49:405–408, 1982.

[6] C. L. Kane and E. J. Mele. Quantum Spin hall effect in graphene. *Phys. Rev. Lett.*, 95:226801, 2005.

[7] B. A. Bernevig and S. C. Zhang. Quantum Spin Hall Effect. *Phys. Rev. Lett.*, 96:106802, 2006.

[8] B. Andrei Bernevig, Taylor L. Hughes, and Shou-Cheng Zhang. Quantum spin hall effect and topological phase transition in hgte quantum wells. *Science*, 314:1757–1761, 2006.

[9] Markus König, Steffen Wiedmann, Christoph Brüne, Andreas Roth, Hartmut Buhmann, Laurens W Molenkamp, Xiao-liang Qi, and Shou-cheng Zhang. Quantum Spin Hall Insulator State in HgTe Quantum Wells. *Science*, 318:766–770, 2007.

[10] C. L. Kane and E. J. Mele. $\mathbb{Z}_2$ topological order and the quantum spin hall effect. *Phys. Rev. Lett.*, 95:146802, 2005.

[11] J. E. Moore and L. Balents. Topological invariants of time-reversal-invariant band structures. *Phys. Rev. B*, 75:121306(R), 2007.

[12] Liang Fu, C. L. Kane, and E. J. Mele. Topological insulators in three dimensions. *Phys. Rev. Lett.*, 98:106803, 2007.

[13] Rahul Roy. Topological phases and the quantum spin Hall effect in three dimensions. *Phys. Rev. B*, 79:195322, 2009.

[14] Liang Fu and C. L. Kane. Topological insulators with inversion symmetry. *Phys. Rev. B*, 76:045302, 2007.

[15] D. Hsieh, D. Qian, L. Wray, Y. Xia, Y.S. Hor, R.J. Cava, and M.Z. Hasan. A topological Dirac insulator in a quantum spin Hall phase. *Nature*, 452:970, 2008.

[16] Haijun Zhang, Chao-Xing Liu, Xiao-Liang Qi, Xi Dai, Zhong Fang, and Shou-Cheng Zhang. Topological insulators in Bi_2Se_3, Bi_2Te_3 and Sb_2Te_3 with a single Dirac cone on the surface. *Nat. Phys.*, 5:438–442, 2009.

[17] Y. Xia, D. Qian, D. Hsieh, L. Wray, A. Pal, H. Lin, A. Bansil, D. Grauer, Y. S. Hor, R. J. Cava, and M. Z. Hasan. Observation of a large-gap topological-insulator class with a single Dirac cone on the surface. *Nat. Phys.*, 5:398–402, 2009.

[18] D. Hsieh, Y. Xia, D. Qian, L. Wray, J.H. Dil, F. Meier, J. Osterwalder, L. Patthey, J.G. Checkelsky, N.P. Ong, A.V. Fedorov, H. Lin, A. Bansil, D. Grauer, Y.S. Hor, R.J. Cava, and M.Z. Hasan. A tunable topological insulator in the spin helical Dirac transport regime. *Nature*, 460:1101, 2009.

[19] D. Hsieh, Y. Xia, L. Wray, D. Qian, A. Pal, J.H. Dil, J. Osterwalder, F. Meier, G. Bihlmayer, C.L. Kane, Y.S. Hor, R.J. Cava, and M.Z. Hasan. Observation of unconventional quantum spin textures in topological insulators. *Science*, 323:919, 2009.

[20] J.-H. Chu Z. K. Liu S.-K. Mo X. L. Qi H. J. Zhang D. H. Lu X. Dai Z. Fang S. C. Zhang I. R. Fisher Z. Hussain Y. L. Chen, J. G. Analytis and Z.-X. Shen. Experimental Realization of a Three-Dimensional Topological Insulator Bi_2Te_3. *Science*, 325:178–181, 2009.

[21] Zhanybek Alpichshev, J. G. Analytis, J.-H. Chu, I. R. Fisher, Y. L. Chen, Z. X. Shen, A. Fang, and A. Kapitulnik. STM Imaging of Electronic Waves on the Surface of Bi_2Te_3: Topologically Protected Surface States and Hexagonal Warping Effects. *Phys. Rev. Lett.*, 104:016401, 2010.

[22] Pedram Roushan, Jungpil Seo, Colin V Parker, Y S Hor, D Hsieh, Dong Qian, Anthony Richardella, M Z Hasan, R J Cava, and Ali Yazdani. Topological surface states protected from backscattering by chiral spin texture. *Nature*, 460:1106, 2009.

[23] J. G. Checkelsky, Y. S. Hor, M. H. Liu, D. X. Qu, R. J. Cava, and N. P. Ong. Quantum interference in macroscopic crystals of nonmetallic Bi_2Se_3. *Phys. Rev. Lett.*, 103:246601, 2009.

[24] D.-X. Qu, Y. S. Hor, J. Xiong, R. J. Cava, and N. P. Ong. Quantum oscillations and Hall anomaly of surface states in the topological insulator Bi_2Te_3. *Science*, 329:821, 2010.

[25] N. P. Butch, K. Kirshenbaum, P. Syers, A. B. Sushkov, G. S. Jenkins, H. D. Drew and J. Paglione. Strong surface scattering in ultrahigh-mobility Bi_2Se_3 topological insulator crystals. *Phys. Rev. B*, 82:125120, 2010.

[26] S. Jia, H. Ji, E. Climent-Pascual, M. K. Fuccillo, M. E. Charles, J. Xiong, N. P. Ong, and R. J. Cava. Low-carrier-concentration crystals of the topological insulator Bi_2Te_2Se. *Phys. Rev. B*, 84:235206, 2011.

[27] Z. Ren, A. A. Taskin, S. Sasaki, K. Segawa, and Y. Ando. Large bulk resistivity and surface quantum oscillations in the topological insulator Bi_2Te_2Se. *Phys. Rev. B*, 82:241306(R), 2010.

[28] J. Xiong, Y. Luo, Y. H. Khoo, S. Jia, R. J. Cava, and N. P. Ong. High-field Shubnikov de Haas oscillations in the topological insulator Bi_2Te_2Se. *Phys. Rev. B*, 86:045314, 2012.

[29] Z. Ren, A. A. Taskin, S. Sasaki, K. Segawa, and Y. Ando. Optimizing $Bi_{2-x}Sb_xTe_{3-y}Se_y$ solid solutions to approach the intrinsic topological insulator regime. *Phys. Rev. B*, 84:165311, 2011.

[30] A. A. Taskin, Z. Ren, S. Sasaki, K. Segawa, and Y. Ando. Observation of Dirac Holes and Electrons in a Topological Insulator. *Phys. Rev. Lett.*, 107:016801, 2011.

[31] I. Teramoto and S. Takayanagi. Relations between the electronic properties and the chemical bonding of $Sb_xBi_{2-x}Te_{3-y}Se_y$ system. *J. Phys. Chem. Sol.*, 19:124–129, 1961.

[32] F. Heusler, W. Starck, and E. Haupt. Observation of Dirac Holes and Electrons in a Topological Insulator. *Verh. DPG*, 5:220, 1903.

[33] T. Graf, C. Felser, and S. S. P. Parkin. Simple rules for the understanding of Heusler compounds. *Progress Sol. State Chem.*, 39:1, 2011.

[34] S. Chadov, X.-L. Qi, J. Kübler, G. H. Fecher, C. Felser, and S.-C. Zhang. Tunable multifunctional topological insulators in ternary Heusler compounds. *Nat. Mat.*, 9:541, 2010.

[35] H. Lin, L. A. Wray, Y. Xia, S. Xu, S. Jia, R. J. Cava, A. Bansil, and M. Z. Hasan. Half-Heusler ternary compounds as new multifunctional experimental platforms for topological quantum phenomena. *Nat. Mat.*, 9:546–549, 2010.

[36] Marcel Franz. Topological insulators: Starting a new family. *Nat. Mat.*, 9:536–537, 2010.

[37] H. C. Kandpal, C. Felser, and R. Seshadri. Covalent bonding and the nature of band gaps in some half-Heusler compounds. *J. Phys. D: Appl. Phys.*, 39:776–785, 2006.

[38] F. Casper, T. Graf, S. Chadov, B. Balke, and C. Felser. Half-Heusler compounds: novel materials for energy and spintronic applications. *Semicond. Sci. and Tech.*, 27:063001, 2012.

[39] Di Xiao, Yugui Yao, Wanxiang Feng, Jun Wen, Wenguang Zhu, Xing Qiu Chen, G. Malcolm Stocks, and Zhenyu Zhang. Half-Heusler compounds as a new class of three-dimensional topological insulators. *Phys. Rev. Lett.*, 105:096404, 2010.

[40] Z.K. Liu, L.X. Yang, S.C. Wu, C. Shekhar, J. Jiang, H.F. Yang, and Y. Zhang. Observation of Unusual Topological Surface States in Half-Heusler Compounds LnPtBi (Ln = Lu , Y). arXiv:1602.05633, 2016.

[41] P. C. Canfield, J. D. Thompson, W. P. Beyermann, A. Lacerda, M. F. Hundley, E. Peterson, Z. Fisk, and H. R. Ott. Magnetism and heavy Fermion-like behavior in the RBiPt series. *J. Appl. Phys.*, 70:5800–5802, 1991.

[42] R. A. Müller, N. R. Lee-Hone, L. Lapointe, D. H. Ryan, T. Pereg-Barnea, A. D. Bianchi, Y. Mozharivskyj, and R. Flacau. Magnetic structure of GdBiPt: A candidate antiferromagnetic topological insulator. *Phys. Rev. B*, 90:041109(R), 2014.

[43] Y. Pan, A. M. Nikitin, T. V. Bay, Y. K. Huang, C. Paulsen, B. H. Yan, and A. de Visser. Superconductivity and magnetic order in the noncentrosymmetric half-Heusler compound ErPdBi. *Europhys. Lett.*, 104:27001, 2013.

[44] A. M. Nikitin, Y. Pan, X. Mao, R. Jehee, G. K. Araizi, Y. K. Huang, C. Paulsen, S. C. Wu, B. H. Yan, and A de Visser. Magnetic and superconducting phase diagram of the half-Heusler topological semimetal HoPdBi. *J. Phys.: Cond. Matt.*, 27:275701, 2015.

[45] Orest Pavlosiuk, Dariusz Kaczorowski, Xavier Fabreges, Arsen Gukasov, and Piotr Wiśniewski. Antiferromagnetism and superconductivity in the half-Heusler semimetal HoPdBi. *Sci. Rep.*, 6:18797, 2016.

[46] Yasuyuki Nakajima, Rongwei Hu, Kevin Kirshenbaum, Alex Hughes, Paul Syers, X. Wang, K. Wang, Renxiong Wang, S. R. Saha, Daniel Pratt, Jeffrey W. Lynn, and Johnpierre Paglione. Topological RPdBi half-Heusler semimetals: A new family of noncentrosymmetric magnetic superconductors. *Sci. Adv.*, 1:e1500242, 2015.

[47] Z. Fisk, P. C. Canfield, W. P. Beyermann, J. D. Thompson, M. F. Hundley, H. R. Ott, E. Felder, M. B. Maple, M. A. Lopez De La Torre, P. Visani, and C. L. Seaman. Massive electron state in YbBiPt. *Phys. Rev. Lett.*, 67:3310–3313, 1991.

[48] T. V. Bay, M. Jackson, C. Paulsen, C. Baines, A. Amato, T. Orvis, M. C. Aronson, Y. K. Huang, and A. de Visser. Low field magnetic response of the noncentrosymmetric superconductor YPtBi. *Sol. State Commun.*, 183:13–17, 2014.

[49] T. V. Bay, T. Naka, Y. K. Huang, and A. de Visser. Superconductivity in noncentrosymmetric YPtBi under pressure. *Phys. Rev. B*, 86:064515, 2012.

[50] Markus Meinert. Unconventional superconductivity in YPtBi and related topological semimetals. *Phys. Rev. Lett.*, 116:137001, 2016.

[51] N. P. Butch, P. Syers, K. Kirshenbaum, A. P. Hope, and J. Paglione. Superconductivity in the topological semimetal YPtBi. *Phys. Rev. B*, 84:220504(R), 2011.

[52] G. Goll, M. Marz, A. Hamann, T. Tomanic, K. Grube, T. Yoshino, and T. Takabatake. Thermodynamic and transport properties of the non-centrosymmetric superconductor LaBiPt. *Physica B*, 403:1065, 2008.

[53] F. F. Tafti, T. Fujii, A. Juneau-Fecteau, S. René de Cotret, N. Doiron-Leyraud, A. Asamitsu, and L. Taillefer. Superconductivity in the noncentrosymmetric half-Heusler compound LuPtBi: A candidate for topological superconductivity. *Phys. Rev. B*, 87:184504, 2013.

[54] Guizhou Xu, Wenhong Wang, Xiaoming Zhang, Yin Du, Enke Liu, Shouguo Wang, Guangheng Wu, Zhongyuan Liu, and Xi Xiang Zhang. Weak Antilocalization Effect and Noncentrosymmetric Superconductivity in a Topologically Nontrivial Semimetal LuPdBi. *Sci. Rep.*, 4:5709, 2014.

[55] Orest Pavlosiuk, Dariusz Kaczorowski, and Piotr Wiśniewski. Shubnikov - de Haas oscillations, weak antilocalization effect and large linear magnetoresistance in the putative topological superconductor LuPdBi. *Sci. Rep.*, 5:9158, 2015.

[56] Andreas P. Schnyder, Shinsei Ryu, Akira Furusaki, and Andreas W W Ludwig. Classification of topological insulators and superconductors. *Phys. Rev. B*, 78:195125, 2008.

[57] Alexei Kitaev. Periodic table for topological insulators and superconductors. *AIP Conf. Proc.*, 1134:22–30, 2009.

[58] A. Yu Kitaev. Fault-tolerant quantum computation by anyons. *Ann. Phys.*, 303:2–30, 2003.

[59] Y. S. Hor, A. J. Williams, J. G. Checkelsky, P. Roushan, J. Seo, Q. Xu, H. W. Zandbergen, A. Yazdani, N. P. Ong, and R. J. Cava. Superconductivity in $Cu_xBi_2Se_3$ and its implications for pairing in the undoped topological insulator. *Phys. Rev. Lett.*, 104:057001, 2010.

[60] M. Kriener, K. Segawa, Z. Ren, S. Sasaki, and Y. Ando. Bulk superconducting phase with a full energy gap in the doped topological insulator $Cu_xBi_2Se_3$. *Phys. Rev. Lett.*, 106:127004, 2011.

[61] Z. Liu, X. Yao, J. Shao, M. Zuo, L. Pi, S. Tan, C. Zhang, and Y. Zhang. Superconductivity with topological surface state in $Sr_xBi_2Se_3$. *J. Am. Chem. Soc.*, 137:10512, 2015.

[62] Satoshi Sasaki and Takeshi Mizushima. Superconducting doped topological materials. *Physica C*, 514:206–217, 2015.

[63] G. Hardy. Materials search for topological superconductors. 2013.

[64] Joran Angeraare. The weak antilocalization effect due to topological surface states of a $Bi_{1.46}Sb_{0.54}Te_{1.7}Se_{1.3}$ nanoflake. Bachelor thesis, University of Amsterdam, 2014. unpublished.

[65] Tran Van Bay. *Experimental investigation of potential topological and p-wave superconductors*. PhD thesis, University of Amsterdam, 2014. unpublished.

[66] Heliox XL Oxford Instruments. http://www.oxford-instruments.com/products/cryogenic-environments/3he-inserts/helium-3-refrigerator-with-sorption-pump-helioxvl.

[67] http://www.ru.nl/hfml/facility/experimental/magnets/.

[68] Quantum Design. *Physical Property Measurment System, DynaCool User's Mannual*.

[69] http://www.qdusa.com/products/dynacool.html.

[70] Quantum Design. Vibrating Sample Magnetometer (VSM) Option User ' s Manual. (1096).

[71] Quantum Design. Physical Property Measurement System AC Transport Option User ' s Manual. (1584), 2003.

[72] Y. Ando. Topological Insulator Materials. *J. Phys. Soc. Jpn*, 82:102001, 2013.

[73] Xiao-Liang Qi and Shou-Cheng Zhang. The quantum spin Hall effect and topological insulators. *Physics Today*, 63:33, 2010.

[74] M. V. Berry. Quantal phase factors accompanying adiabatic changes. *Proceedings of the Royal Society of London A: Mathematical, Physical and Engineering Sciences*, 392:45–57, 1984.

[75] Tsuneya Ando, Takeshi Nakanishi, and Riichiro Saito. Berry's Phase and Absence of Back Scattering in Carbon Nanotubes. *J. Phys. Soc. Jpn*, 67:2857–2862, 1998.

[76] Markus König, Hartmut Buhmann, Laurens W. Molenkamp, Taylor Hughes, Chao X-ing Liu, Xiao Liang Qi, and Shou Cheng Zhang. The quantum spin Hall effect: Theory and experiment. *J. Phys. Soc. Jpn*, 77:031007, 2008.

[77] Bin Zhou, Hai-Zhou Lu, Rui-Lin Chu, Shun-Qing Shen, and Qian Niu. Finite size effects on helical edge states in a quantum spin-Hall system. *Phys. Rev. Lett.*, 101(24):246807, 2008.

[78] Jacob Linder, Takehito Yokoyama, and Asle Sudbo. Quasiparticle interference on the surface of the topological insulator Bi_2Te_3. *Phys. Rev. B*, 80:245439, 2009.

[79] Hai Zhou Lu, Wen Yu Shan, Wang Yao, Qian Niu, and Shun Qing Shen. Massive Dirac fermions and spin physics in an ultrathin film of topological insulator. *Phys. Rev. B*, 81:115407, 2010.

[80] Binghai Yan, Martin Jansen, and Claudia Felser. A large-energy-gap oxide topological insulator based on the superconductor $BaBiO_3$. *Nat. Phys.*, 9:709, 2013.

[81] Binghai Yan, Lukas Müchler, and Claudia Felser. Prediction of weak topological insulators in layered semiconductors. *Phys. Rev. Lett.*, 109:116406, 2012.

[82] E. Mooser and W. B. Pearson. New semiconducting compounds. *Phys. Rev.*, 101:492–493, 1956.

[83] J. Black, E.M. Conwell, L. Seigle, and C.W. Spencer. Electrical and optical properties of some $M_2^{V-B}N_3^{VI-B}$ semiconductors. *J. Phys. Chem. Sol.*, 2:240 – 251, 1957.

[84] Matthew Brahlek, Nikesh Koirala, Namrata Bansal, and Seongshik Oh. Transport properties of topological insulators: Band bending, bulk metal-to-insulator transition, and weak anti-localization. *Sol. State Commun.*, 215:54–62, 2014.

[85] N. P. Butch, K. Kirshenbaum, P. Syers, A. B. Sushkov, G. S. Jenkins, H. D. Drew and J. Paglione. Strong surface scattering in ultrahigh-mobility Bi_2Se_3 topological insulator crystals. *Phys. Rev. B*, 82:125120, 2010.

[86] Peter P. Edwards and M. J. Sienko. The transition to the metallic state. *Acc. Chem. Res.*, 15(3):87–93, 1982.

[87] Alexander Pergament, Genrikh Stefanovich, and Nadezhda Markova. The mott criterion: So simple and yet so complex. arXiv:1411.4372, 2014.

[88] P. P. Edwards, T. V. Ramakrishnan, and C. N. R. Rao. The metal-nonmetal transition: A global perspective. *J. Phys. Chem.*, 99:5228–5239, 1995.

[89] V. Zelezny, J. Petzelt, V.V. Kaminski, M.V. Romanova, and A.V. Golubkov. Far infrared conductivity and dielectric response of semiconducting sms. *Sol. State Commun.*, 72:43 – 47, 1989.

[90] V.V. Kaminski, L.N. Vasil, M.V. Romanova, and S.M. Solov. The Mechanism of the Appearance of an Electromotive Force on Heating of SmS Single Crystals. *Phys. Sol. State*, 43:1030–1032, 2001.

[91] Alexander Pergament. Metal-insulator transition: the Mott criterion and. *J. Phys.: Condens. Matt.*, 15:3217–3223, 2003.

[92] Alexander L. Pergament and Genrikh B. Stefanovich. Insulator-to-metal transition in vanadium sesquioxide: does the Mott criterion work in this case? *Phase Transitions*, 85:185–194, 2012.

[93] Regel A.R. Ioffe, A.F. Non-crystalline, amorphous, and liquid electronic semiconductors. *Prog. Semicond.*, 4:237–291, 1960.

[94] Davis E.A. Mott, N.F. *Electronic process in non-crystalline materials*. Clarendon Press, Oxford, second ed. edition, 1979.

[95] Z. Ren, A. A. Taskin, S. Sasaki, K. Segawa, and Y. Ando. Fermi level tuning and a large activation gap achieved in the topological insulator Bi_2Te_2Se by Sn doping. *Phys. Rev. B*, 85:155301, 2012.

[96] Y. S. Hor, A. Richardella, P. Roushan, Y. Xia, J. G. Checkelsky, A. Yazdani, M. Z. Hasan, N. P. Ong, and R. J. Cava. p-type Bi_2Se_3 for topological insulator and low-temperature thermoelectric applications. *Phys. Rev. B*, 79:195208, 2009.

[97] Jian Wang, Ashley M. Dasilva, Cui Zu Chang, Ke He, J. K. Jain, Nitin Samarth, Xu Cun Ma, Qi Kun Xue, and Moses H W Chan. Evidence for electron-electron interaction in topological insulator thin films. *Phys. Rev. B*, 83:245438, 2011.

[98] H. Steinberg, D. R. Gardner, Y. S. Lee, and P. Jarillo-Herrero. Surface State Transport and Ambipolar Electric Field Effect in Bi_2Se_3 Nanodevices. *Nano. Lett.*, 10:5032, 2010.

[99] J. G. Analytis, R. D. McDonald, S. C. Riggs, J.-H. Chu, G. S. Boebinger, and I. R. Fisher. Two-dimensional surface state in the quantum limit of a topological insulator. *Nat. Phys.*, 6:960–964, 2010.

[100] J. G. Analytis, J.-H. Chu, Y. Chen, F. Corredor, R. D. McDonald, Z. X. Shen, and I. R. Fisher. Bulk Fermi surface coexistence with Dirac surface state in Bi_2Se_3: A comparison of photoemission and Shubnikov-de Haas measurements. *Phys. Rev. B*, 81:205407, 2010.

[101] Seung Sae Hong, Judy J. Cha, Desheng Kong, and Yi Cui. Ultra-low carrier concentration and surface-dominant transport in antimony-doped Bi_2Se_3 topological insulator nanoribbons. *Nat. Commun.*, 3:757, 2012.

[102] Namrata Bansal, Yong Seung Kim, Matthew Brahlek, Eliav Edrey, and Seongshik Oh. Thickness-independent transport channels in topological insulator Bi_2Se_3 thin films. *Phys. Rev. Lett.*, 109:116804, 2012.

[103] Jun Xiong, Yuehaw Khoo, Shuang Jia, R. J. Cava, and N. P. Ong. Tuning the quantum oscillations of surface Dirac electrons in the topological insulator Bi_2Te_2Se by liquid gating. *Phy. Rev. B*, 88:035128, 2013.

[104] M. Bianchi, D. Guan, S. Bao, J. Mi, B. B. Iversen, P. D. C. King, and Ph. Hofmann. Coexistence of the topological state and a two-dimensional electron gas on the surface of Bi_2Se_3. *Nat. Commun.*, 1:128, 2010.

[105] Matthew Brahlek, Nikesh Koirala, Maryam Salehi, Namrata Bansal, and Seongshik Oh. Emergence of decoupled surface transport channels in bulk insulating Bi_2Se_3 thin films. *Phys. Rev. Lett.*, 113:026801, 2014.

[106] Matthew Brahlek, Yong Seung Kim, Namrata Bansal, Eliav Edrey, and Seongshik Oh. Surface versus bulk state in topological insulator Bi_2Se_3 under environmental disorder. *Appl. Phys. Lett.*, 99:10–13, 2011.

[107] H.-Z. Lu and S.-Q. Shen. Weak localization of bulk channels in topological insulator thin films. *Phys. Rev. B*, 84:125138, 2011.

[108] Hai-Zhou Lu and Shun-Qing Shen. Weak localization and weak anti-localization in topological insulators. 2014.

[109] S. Hikami, A. I. Larkin, and Y. Nagaoka. Spin-Orbit Interaction and Magnetoresistance in the Two-Dimensional Random System. *Prog. Theor. Phys. Rev.*, 63:707–710, 1980.

[110] D. J. Thouless. Maximum metallic resistance in thin wires. *Phys. Rev. Lett.*, 39:1167–1169, 1977.

[111] Patrick A. Lee and T. V. Ramakrishnan. Disordered electronic systems. *Rev. Mod. Phys.*, 57:287–337, 1985.

[112] Minhao Liu, Cui Zu Chang, Zuocheng Zhang, Yi Zhang, Wei Ruan, Ke He, Li Li Wang, Xi Chen, Jin Feng Jia, Shou Cheng Zhang, Qi Kun Xue, Xucun Ma, and Yayu Wang. Electron interaction-driven insulating ground state in Bi_2Se_3 topological insulators in the two-dimensional limit. *Phys. Rev. B*, 83:165440, 2011.

[113] J. Chen, X. Y. He, K. H. Wu, Z. Q. Ji, L. Lu, J. R. Shi, J. H. Smet, and Y. Q. Li. Tunable surface conductivity in Bi_2Se_3 revealed in diffusive electron transport. *Phys. Rev. B*, 83:241304(R), 2011.

[114] T.-C. Hsiung, D.-Y. Chen, L. Zhao, Y.-H. Lin, C.-Y. Mou, T.-K. Lee, M.-K. Wu, and Y.-Y. Chen. Enhanced surface mobility and quantum oscillations in topological insulator $Bi_{1.5}Sb_{0.5}Te_{1.7}Se_{1.3}$ nanoflakes. *Appl. Phys. Lett.*, 103:163111, 2013.

[115] B. Xia, P. Ren, A. Sulaev, P. Liu, S.-Q. Shen, and L. Wang. Indications of surface-dominated transport in single crystalline nanoflake devices of topological insulator $Bi_{1.5}Sb_{0.5}Te_{1.8}Se_{1.2}$. *Phys. Rev. B*, 87:085442, 2013.

[116] Duan Feng and Guojun Jin. *Introduction to condensed matter physics*, volume 1. World Scientific Publishing, Singapore, 2005.

[117] D. Shoenberg. *Magnetic Oscillations in Metals*. Cambridge University Press, Cambridge, 1984.

[118] http://www.referatele.com/referate/fizica/online4/HALL-EFFECT—Explanation-of-the-Quantum-Hall-Effect-referatele-com.php.

[119] E.M. Lifshits and A.M. Kosevich. Theory of the Shubnikov-de Haas effect. *J. Phys. Chem. Sol.*, 4:1–10, 1958.

[120] Liang Fu and C. L. Kane. Superconducting proximity effect and majorana fermions at the surface of a topological insulator. *Phys. Rev. Lett.*, 100:096407, 2008.

[121] Liang Fu and Erez Berg. Odd-parity topological superconductors: Theory and application to $Cu_xBi_2Se_3$. *Phys. Rev. Lett.*, 105:097001, 2010.

[122] T. Tsuneto. *Superconductivity and Superfluidity*. Cambridge University Press, 2005.

[123] Xiao Liang Qi, Taylor L. Hughes, S. Raghu, and Shou Cheng Zhang. Time-reversal-invariant topological superconductors and superfluids in two and three dimensions. *Phys. Rev. Lett.*, 102:187001, 2009.

[124] M. Kriener, Kouji Segawa, Zhi Ren, Satoshi Sasaki, and Yoichi Ando. Bulk superconducting phase with a full energy gap in the doped topological insulator $Cu_xBi_2Se_3$. *Phys. Rev. Lett.*, 106:127004, 2011.

[125] Liang Fu. Odd-parity topological superconductor with nematic order: Application to $Cu_xBi_2Se_3$. *Phys. Rev. B*, 90:100509, 2014.

[126] K. Matano, M. Kriener, K. Segawa, Y. Ando, and Guo-qing Zheng. Spin-Rotation Symmetry Breaking in the Superconducting State of $Cu_xBi_2Se_3$. arXiv:1512.07086, 2015.

[127] Tatsuki Hashimoto, Keiji Yada, Ai Yamakage, Masatoshi Sato, and Yukio Tanaka. Bulk Electronic State of Superconducting Topological Insulator. *J. Phys. Soc. Jpn.*, 82:044704, 2013.

[128] I. Žutić, Jaroslav Fabian, and S.D. Sarma. Spintronics: Fundamentals and applications. *Rev. Mod. Phys.*, 76:323, 2004.

[129] C. Nayak, A. Stern, M. Freedman, and S. Das Sarma. Non-Abelian anyons and topological quantum computation. *Rev. Mod. Phys.*, 80:1083–1159, 2008.

[130] Y. L. Chen, J. G. Analytis, J.-H. Chu, Z. K. Liu, S.-K. Mo, X. L. Qi, H. J. Zhang, D. H. Lu, X. Dai, Z. Fang, S. C. Zhang, I. R. Fisher, Z. Hussain, and Z.-X. Shen. Experimental Realization of a Three-Dimensional Topological Insulator, Bi_2Te_3. *Science*, 325:178–181, 2009.

[131] J. Chen, H. J. Qin, F. Yang, J. Liu, T. Guan, F. M. Qu, G. H. Zhang, J. R. Shi, X. C. Xie, C. L. Yang, K. H. Wu, Y. Q. Li, and L. Lu. Gate-Voltage Control of Chemical Potential and Weak Antilocalization in Bi_2Se_3. *Phys. Rev. Lett.*, 105:176602, 2010.

[132] J. G. Checkelsky, Y. S. Hor, R. J. Cava, and N. P. Ong. Bulk Band Gap and Surface State Conduction Observed in Voltage-Tuned Crystals of the Topological Insulator Bi_2Se_3. *Phys. Rev. Lett.*, 106:196801, 2011.

[133] S. Jia, H. Beidenkopf, I. Drozdov, M. K. Fuccillo, J. Seo, J. Xiong, N. P. Ong, A. Yazdani, and R. J. Cava. Defects and high bulk resistivities in the Bi-rich tetradymite topological insulator $Bi_{2+x}Te_{2-x}Se$. *Phys. Rev. B*, 86:165119, 2012.

[134] M.K. Fuccillo, S. Jia, M.E. Charles, and R.J. Cava. Thermoelectric Properties of Bi_2Te_2Se Compensated by Native Defects and Sn Doping. *J. Electr. Mater.*, 42:1246, 2013.

[135] T. Arakane, T. Sato, S. Souma, K. Kosaka, N. Nakyama, M. Komatsu, T. Takahashi, Z. Ren, K. Segawa, and Y. Ando. Tunable Dirac cone in the topological insulator $Bi_{2-x}Sb_xTe_{3-y}Se_y$. *Nat. Commun.*, 3:636, 2012.

[136] C. S. Tang, B. Xia, X. Zou, S. Chen, H.-W. Ou, L. Wang, A. Rusydi, J.-X. Zhu, and E.E.M. Chia. Terahertz conductivity of topological surface states in $Bi_{1.5}Sb_{0.5}Te_{1.8}Se_{1.2}$. *Sci. Rep.*, 3:3513, 2013.

[137] W. Ko, I. Jeon, H. W. Kim, H. Kwon, S.-J. Kahng, J. Park, J. S. Kim, S. W. Hwang, and H. Suh. Atomic and electronic structure of an alloyed topological insulator, $Bi_{1.5}Sb_{0.5}Te_{1.7}Se_{1.3}$. *Sci. Rep.*, 3:2656, 2013.

[138] S. Kim, S. Yoshizawa, Y. Ishida, K. Eto, K. Segawa, Y. Ando, S. Shin, and F. Komori. Robust protection from backscattering in the topological insulator $Bi_{1.5}Sb_{0.5}Te_{1.7}Se_{1.3}$. *Phys. Rev. Lett.*, 112:136802, 2014.

[139] P. D.C. King, R. C. Hatch, M. Bianchi, R. Ovsyannikov, C. Lupulescu, G. Landolt, B. Slomski, J. H. Dil, D. Guan, J. L. Mi, E. D L Rienks, J. Fink, a. Lindblad, S. Svensson, S. Bao, G. Balakrishnan, B. B. Iversen, J. Osterwalder, W. Eberhardt, F. Baumberger, and Ph Hofmann. Large Tunable Rashba Spin Splitting of a Two-Dimensional Electron Gas in Bi_2Se_3. *Phys. Rev. Lett.*, 107:096802, 2011.

[140] M. S. Bahramy, P. D. C. King, A. de la Torre, J. Chang, M. Shi, L. Patthey, G. Balakrishnan, Ph. Hofmann, R. Arita, N. Nagaosa, and F. Baumberger. Emergent quantum confinement at topological insulator surfaces. *Nat. Commun.*, 3:1159, 2012.

[141] D.J. Kim, J. Xia, and Z. Fisk. Topological surface state in the Kondo insulator samarium hexaboride. *Nat. Mater.*, 13:466, 2014.

[142] Paul Syers, Dohun Kim, Michael S. Fuhrer, and Johnpierre Paglione. Tuning Bulk and Surface Conduction in the Proposed Topological Kondo Insulator SmB_6. *Phys. Rev. Lett.*, 114:096601, 2015.

[143] D. Culcer. Transport in three-dimensional topological insulators: Theory and experiment. *Physica E*, 44:860–884, 2012.

[144] H.-Z. Lu and S.-Q. Shen. Finite-Temperature Conductivity and Magnetoconductivity of Topological Insulators. *Phys. Rev. Lett.*, 112:146601, 2014.

[145] J. Lee, J. Park, J.-H. Lee, J. S. Kim, and H.-J. Lee. Gate-tuned differentiation of surface-conducting states in $Bi_{1.5}Sb_{0.5}Te_{1.7}Se_{1.3}$ topological-insulator thin crystals. *Phys. Rev. B*, 86:245321, 2012.

[146] M. Z. Hasan and J. E. Moore. Three-Dimensional Topological Insulators. *Annu. Rev. Condens. Matter Phys.*, 2:55, 2011.

[147] J. Maciejko, T. L. Hughes, and S.-C. Zhang. The Quantum Spin Hall Effect. *Annu. Rev. Condens. Matter Phys.*, 2:31–53, 2011.

[148] C. W. J. Beenakker. Search for Majorana Fermions in Superconductors. *Annu. Rev. Condens. Matter Phys.*, 4:113–136, 2013.

[149] D.-X. Qu, Y. S. Hor, R. J. Cava, and N. P. Ong. Quantum oscillations and hall anomaly of surface states in the topological insulator Bi_2Te_3. *Science*, 329:821, 2010.

[150] Kouji Segawa, Zhi Ren, Satoshi Sasaki, Tetsuya Tsuda, Susumu Kuwabata, and Yoichi Ando. Ambipolar transport in bulk crystals of a topological insulator by gating with ionic liquid. *Phys. Rev. B*, 86:075306, 2012.

[151] Azat Sulaev, Minggang Zeng, Shun-Qing Shen, Soon Khuen Cho, Wei Guang Zhu, Yuan Ping Feng, Sergey V. Eremeev, Yoshiyuki Kawazoe, Lei Shen, and Lan Wang. Electrically Tunable In-Plane Anisotropic Magnetoresistance in Topological Insulator $BiSbTeSe_2$ Nanodevices. *Nano. Lett.*, 15:2061, 2015.

[152] Y. Pan, D. Wu, J. R. Angevaare, H. Luigjes, E. Frantzeskakis, N. de Jong, E. van Heumen, T. V. Bay, B. Zwartsenberg, Y. K. Huang, M. Snelder, A. Brinkman, M. S. Golden, and A. de Visser. Low carrier concentration crystals of the topological insulator $Bi_{2-x}Sb_xTe_{3-y}Se_y$: a magnetotransport study. *New J. Phys.*, 16:123035, 2014.

[153] A. A. Taskin and Y. Ando. Berry phase of nonideal Dirac fermions in topological insulators. *Phys. Rev. B*, 84:035301, 2011.

[154] A. R. Wright and R. H. McKenzie. Quantum oscillations and Berry's phase in topological insulator surface states with broken particle-hole symmetry. *Phys. Rev. B*, 87:085411, 2013.

[155] M. Petrushevsky, E. Lahoud, A. Ron, E. Maniv, I. Diamant, I. Neder, S. Wiedmann, V. K. Guduru, F. Chiappini, U. Zeitler, J. C. Maan, K. Chashka, A. Kanigel, and Y. Dagan. Probing the surface states in Bi_2Se_3 using the Shubnikov-de Haas effect. *Phys. Rev. B*, 86:045131, 2012.

[156] A. Ishihara and L. Smrčka. Density and magnetic field dependences of the conductivity of two-dimensional electron systems. *J. Phys. C: Solid State Phys.*, 19:6777–6789, 1986.

[157] G. P. Mikitik and Yu. V. Sharlai. Manifestation of Berry's Phase in Metal Physics. *Phys. Rev. Lett.*, 82:2147–2150, 1999.

[158] B. Sacepe, J. B. Oostinga, J. Li, A. Ubaldini, N.J.G. Couto, E. Giannini, and A. F. Morpurgo. Gate-tuned normal and superconducting transport at the surface of a topological insulator. *Nat. Commun.*, 2:575, 2011.

[159] Y. Zhang, Y.-W. Tan, H. L. Stormer, and P. Kim. Experimental observation of the quantum Hall effect and Berry's phase in graphene. *Nature*, 438:201–204, 2005.

[160] E. Frantzeskakis, N. de Jong, B. Zwartsenberg, T. V. Bay, Y. K. Huang, S. V. Ramankutty, A. Tytarenko, D. Wu, Y. Pan, S. Hollanders, M. Radovic, N. C. Plumb, N. Xu, M. Shi, C. Lupulescu, T. Arion, R. Ovsyannikov, A. Varykhalov, W. Eberhardt, A. de Visser, E. van Heumen, and M. S. Golden. Dirac states with knobs on: Interplay of external parameters and the surface electronic properties of three-dimensional topological insulators. *Phys. Rev. B*, 91:205134, 2015.

[161] E. Frantzeskakis, N. de Jong, B. Zwartsenberg, Y.K. Huang, T.V. Bay, P. Pronk, E. van Heumen, D. Wu, Y. Pan, M. Radovic, N.C. Plumb, N. Xu, M. Shi, A. de Visser, and M.S. Golden. Micro-metric electronic patterning of a topological band structure using a photon beam. *Sci. Rep.*, 5:16309, 2015.

[162] Z. H. Zhu, G. Levy, B. Ludbrook, C. N. Veenstra, J. A. Rosen, R. Comin, D. Wong, P. Dosanjh, A. Ubaldini, P. Syers, N. P. Butch, J. Paglione, I. S. Elfimov, and A. Damascelli. Rashba spin-splitting control at the surface of the topological insulator Bi_2Se_3. *Phys. Rev. Lett.*, 107:186405, 2011.

[163] D. Culcer, E. H. Hwang, T. D. Stanescu, and S. Das Sarma. Two-dimensional surface charge transport in topological insulators. *Phys. Rev. B*, 82:155457, 2010.

[164] W. Feng, D. Xiao, Y. Zhang, and Y. Yao. Half-Heusler topological insulators: A first-principles study with the Tran-Blaha modified Becke-Johnson density functional. *Phys. Rev. B*, 82:235121, 2010.

[165] P. A. Frigeri, D. F. Agterberg, A. Koga, and M. Sigrist. Superconductivity without inversion symmetry: MnSi versus $CePt_3Si$. *Phys. Rev. Lett.*, 92:097001, 2004.

[166] M. G. Haase, T. Schmidt, C. G. Richter, H. Block, and W. Jeitschko. Equiatomic Rare Earth (Ln) Transition Metal Antimonides LnTSb (T=Rh, lr) and Bismuthides LnTBi (T=Rh, Ni, Pd, Pt). *J. Solid State Chem.*, 168:18, 2002.

[167] T. M. Riedemann. Heat capacities, magnetic properties and resistivity of ternary RPdBi alloys where R = La, Nd, Gd, Dy, Er, Lu. Master's thesis, Iowa State University, 1996.

[168] K. Gofryk, D. Kaczorowski, T. Plackowski, A. Leithe-Jasper, and Yu. Grin. Magnetic and transport properties of the rare-earth-based Heusler phases RPdZ and RPd_2Z (Z=Sb,Bi). *Phys. Rev. B*, 72:094409, 2005.

[169] K. Gofryk, D. Kaczorowski, T. Plackowski, A. Leithe-Jasper, and Yu. Grin. Magnetic and transport properties of rare-earth-based half-Heusler phases RPdBi: Prospective systems for topological quantum phenomena. *Phys. Rev. B*, 84:035208, 2011.

[170] D. Kaczorowski, K. Gofryk, T. Plackowski, A. Leithe-Jasper, and Yu. Grin. Unusual features of erbium-based Heusler phases. *J. Magn. Magn. Mat.*, 290-291:573, 2005.

[171] T. Sekimoto, K. Kurosaki, H. Muta, and S. Yamanaka. Thermoelectric and thermophysical properties of ErPdX (X=Sb and Bi) half-Heusler compounds. *J. Appl. Phys.*, 99:103701, 2006.

[172] B. R. Matthias, T. H. Geballe, and V. B. Comton. Superconductivity. *Rev. Mod. Phys.*, 35:1, 1963.

[173] C. Domb. *The Critical Point*. Taylor and Francis, London, 1996.

[174] J. Jensen and A. R. Mackintosh. *Rare Earth Magnetism*. Clarendon Press, Oxford, 1991.

[175] E. Bauer and M. Sigrist, editors. *Non Centrosymmetric Superconductors*, volume 847 of *Lecture Notes in Physics*. Springer, Berlin, 2012.

[176] R. N. Shelton. Coexistence of long-range magnetic order and superconductivity: An overview of ternary rare earth compounds. *J. Less Comm. Metals*, 94:69–74, 1983.

[177] B. K. Cho, P. C. Canfield, L. L. Miller, D. C. Johnston, W. P. Beyermann, and A. Yatskar. Magnetism and superconductivity in single-crystal $ErNi_2B_2C$. *Phys. Rev. B*, 52:3684, 1995.

[178] R. N. Shelton, L. S. Hausermann-Berg, M. J. Johnson, P. Klavins, and H. D. Yang. Coexistence of superconductivity and long-range magnetic order in $ErPd_2Sn$. *Phys. Rev. B*, 34:199, 1986.

[179] E. Bauer, G. Hilscher, H. Michor, Ch. Paul, E. W. Scheidt, A. Gribanov, Yu. Seropegin, H. Noël, M. Sigrist, and P. Rogl. Heavy Fermion Superconductivity and Magnetic Order in Noncentrosymmetric $CePt_3Si$. *Phys. Rev. Lett.*, 92:027003, 2004.

[180] J. Goraus, A. Ślebarski, and M. Fijałkowski. Experimental and theoretical study of CePdBi. *J. Phys.: Condens. Matter*, 25:176002, 2013.

[181] N. R. Werthamer, E. Helfand, and P. C. Hohenberg. Temperature and Purity Dependence of the Superconducting Critical Field, H_{c2}. III. Electron Spin and Spin-Orbit Effects. *Phys. Rev.*, 147:295–302, 1966.

[182] J. P. Perdew, K. Burke, and M. Ernzerhof. Generalized gradient approximation made simple. *Phys. Rev. Lett.*, 77:3865, 1996.

[183] L. Maron and O. Eisenstein. Do f Electrons Play a Role in the Lanthanide-Ligand Bonds? A DFT Study of $Ln(NR_2)_3$; R = H, SiH_3. *J. Phys. Chem. A*, 104:7140, 2000.

[184] G. Kresse and J. Hafner. Ab initio molecular dynamics for liquid metals. *Phys. Rev. B*, 47:558(R), 1993.

[185] G. Kresse and D. Joubert. From ultrasoft pseudopotentials to the projector augmented-wave method. *Phys. Rev. B*, 59:1758, 1999.

[186] X.-L. Qi, T. L. Hughes, and S.-C. Zhang. Topological field theory of time-reversal invariant insulators. *Phys. Rev. B*, 78:195424, 2008.

[187] O. Pavlosiuk, K. Filar, P. Wiśniewski, and D. Kaczorowski. Magnetic order and SdH effect in half-heusler phase ErPdBi. *Acta Physica Polonica A*, 127:656–658, 2015.

[188] M. Z. Hasan and C. L. Kane. Topological insulators. *Rev. Mod. Phys.*, 82:3045, 2010.

[189] X.-L. Qi and S.-C. Zhang. Topological insulators and superconductors. *Rev. Mod. Phys.*, 83:1057, 2011.

[190] A. P. Schnyder, S. Ryu, A. Furusaki, and A. W. W. Ludwig. Classification of topological insulators and superconductors. *AIP Conf. Proc.*, 1134:10, 2009.

[191] M. Sato. Topological properties of spin-triplet superconductors and Fermi surface topology in the normal state. *Phys. Rev. B*, 79:214526, 2009.

[192] M. Sato. Topological odd-parity superconductors. *Phys. Rev. B*, 81:220604, 2010.

[193] V. Mourik, K. Zua, S. M. Frolov, S. R. Plissard, E. P. A. M. Bakkers, and L. P. Kouwenhoven. Signatures of Majorana fermions in hybrid superconductor-semiconductor nanowire devices. *Science*, 336:1003, 2012.

[194] S. Sasaki, Z. Ren, A. A. Taskin, K. Segawa, L. Fu, and Y. Ando. Odd-parity pairing and topological superconductivity in a strongly spin-orbit coupled semiconductor. *Phys. Rev. Lett.*, 109:217004, 2012.

[195] Binghai Yan and Anne de Visser. Half-Heusler topological insulators. *MRS Bulletin*, 39:859–866, 2014.

[196] L. A. Wray, S.Y. Xu, Y. Xia, Y. S. Hor, D. Qian, A. V. Fedorov, H. Lin, A. Bansil, R. J. Cava, and M. Z. Hasan. Observation of topological order in a superconducting doped topological insulator. *Nature Phys.*, 6:855, 2010.

[197] L. Fu and E. Berg. Odd-parity topological superconductors: Theory and application to $Cu_xBi_2Se_3$. *Phys. Rev. Lett.*, 105:097001, 2010.

[198] S. Sasaki, M. Kriener, K. Segawa, K. Yada, Y. Tanaka, M. Sato, and Y. Ando. Topological superconductivity in $Cu_xBi_2Se_3$. *Phys. Rev. Lett.*, 107:217001, 2011.

[199] N. Levy, T. Zhang, J. Ha, F. Sharifi, A. A. Talin, Y. Kuk, and J. A. Stroscio. Local measurements of the superconducting pairing symmetry in $Cu_xBi_2Se_3$. *Phys. Rev. Lett.*, 110:117001, 2013.

[200] J. A. Schneeloch, R. D. Zhong, Z. J. Xu, G. D. Gu, and J. M. Tranquada. Dependence of superconductivity in $Cu_xBi_2Se_3$ on quenching conditions. *Phys. Rev. B*, 91:144506, 2015.

[201] Shruti, V. K. Maurya, P. Neha, P. Srivastava, and S. Patnaik. Superconductivity by Sr intercalation in the layered topological insulator Bi_2Se_3. *Phys. Rev. B*, 92:020506(R), 2015.

[202] C. Q. Han, H. Li, W. J. Chen, F. Zhu, M.-Y. Yao, Z. J. Li, M. Wang, B. F. Gao, D. Guan, C. Liu, C. L. Gao, D. Qian, and J.-F. Jia. Electronic structure of a superconducting topological insulator Sr-doped Bi_2Se_3. *Appl. Phys. Lett.*, 107:171602, 2015.

[203] M. Neupane, Y. Ishida, R. Sankar, J.-X. Zhu, D. S. Sanchez, I. Belopolski, S.-Y. Xu, N. Alidoust, S. Shin, F. Chou, M. Z. Hasan, and T. Durakiewicz. Electronic structure and relaxation dynamics in a superconducting topological material. *Sci. Rep.*, 6:22557, 2016.

[204] R.A. Klemm. *Layered Superconductors, Volume 1*. Oxford University Press, Oxford, 2012.

[205] R. C. Morris, R. V. Coleman, and R. Bhandari. Superconductivity and magnetoresistance in $NbSe_2$. *Phys. Rev. B*, 5:895, 1972.

[206] M. Tinkham. *Introduction to Superconductivity*. McGraw-Hill Inc., New York, 1996.

[207] Y. Nagai, H. Nakamura, and M. Machida. Rotational isotropy breaking as proof for spin-polarized Cooper pairs in the topological superconductor $Cu_xBi_2Se_3$. *Phys. Rev. B*, 86:094507, 2012.

[208] Z. X. Shi, M. Tokunaga, T. Tamegai, Y. Takano, K. Togano, H. Kito, and H. Ihara. Out-of-plane and in-plane anisotropy of upper critical field in MgB_2. *Phys. Rev. B*, 68:104513, 2003.

[209] K. Takanaka. Upper critical field of anisotropic superconductors. *Sol. State Comm.*, 42:123, 1982.

[210] H. Köhler. Trigonal warping of the Fermi surface in n-Bi_2Se_3. *Sol. State Comm.*, 13:1585, 1973.

[211] E. Lahoud, E. Maniv, M. S. Petrushevsky, M. Naamneh, A. Ribak, S. Wiedmann, L. Petaccia, Z. Salman, K. B. Chashka, Y. Dagan, and A. Kanigel. Evolution of the Fermi surface of a doped topological insulator with carrier concentration. *Phys. Rev. B*, 88:195107, 2013.

[212] A. M. Clogston. Upper limit for the upper critical field in hard superconductors. *Phys. Rev. Lett.*, 9:266, 1962.

[213] L. Fu. *private communication*.

[214] P. L. Krotkov and V. P. Mineev. Upper critical field in a trigonal unconventional superconductor: UPt_3. *Phys. Rev. B*, 65:224506, 2002.

[215] M. Kriener, K. Segawa, Z. Ren, S. Sasaki, S. Wada, S. Kuwabata, and Y. Ando. Electrochemical synthesis and superconducting phase diagram of $Cu_xBi_2Se_3$. *Phys. Rev. B*, 84:054513, 2011.

[216] C. Mann, D. West, I. Miotkowski, Y. P. Chen, S. Zhang, and C.-K. Shih. Observation of Coulomb repulsion between Cu intercalants in $Cu_xBi_2Se_3$. *Phys. Rev. B*, 89:155312, 2014.

[217] Du Xing Chen, Enric Pardo, and Alvaro Sanchez. Demagnetizing factors of rectangular prisms and ellipsoids. *IEEE Transactions on Magnetics*, 38:1742–1752, 2002.

List of publications

1. **Y. Pan**, A.M. Nikitin, G.K. Araizi, Y.K. Huang, Y. Matsushita, T. Naka and A. de Visser, *Rotational symmetry breaking in the topological superconductor $Sr_xBi_2Se_3$ probed by upper-critical field experiments*, (**2016**) Sci. Rep., 6, 28632
[Chapter 7]

2. T. Naka, A.M. Nikitin, **Y. Pan**, A. de Visser, T. Nakane, F. Ishikawa, Y. Yamada, M. Imai, and A. Matsushita, *Composition induced metal-insulator quantum phase transition in the Heusler type Fe_2VAl*, (**2016**) J. Phys.: Condens. Matter, 28, 285601

3. **Y. Pan**, A.M. Nikitin, D. Wu, Y.K. Huang, A. Puri, S. Wiedmann, U. Zeitler, E. Frantzeskakis, E. van Heumen, M.S. Golden and A. de Visser, *Quantum oscillations of the topological surface states in low carrier concentration crystals of $Bi_{2-x}Sb_xTe_{3-y}Se_y$*, (**2016**) Solid State Comm., 227, 13-18
[Chapter 5]

4. A.M. Nikitin, **Y. Pan**, X. Mao, R. Jehee, G.K. Araizi, Y.K.Huang, C. Paulsen, S.C. Wu, B.H. Yan and A. de Visser, *Magnetic and superconducting phase diagram of the half-Heusler topological semimetal HoPdBi*, (**2015**) J. Phys.: Condens. Matter, 27, 275701

5. E. Frantzeskakis, N. de Jong, B. Zwartsenberg, T.V. Bay, Y.K. Huang, S.V. Ramankutty, A. Tytarenko, D. Wu, **Y. Pan**, S. Hollanders, M. Radovic, N.C. Plumb, N. Xu, M. Shi, C. Lupulescu, T. Arion, R, Ovsyannikov, A. Varykhalov, W. Eberhardt, A. de Visser, E. van Heumen and M.S. Golden, *Dirac states with knobs on: Interplay of external parameters and the surface electronic properties of three-dimensional topological insulators*, (**2015**) Phys. Rev. B, 91, 205134

6. E. Frantzeskakis, N. de Jong, B. Zwartsenberg, Y.K. Huang, T.V. Bay, P. Pronk, E. van Heumen, D. Wu, **Y. Pan**, M. Radovic, N.C. Plumb, N. Xu, M. Shi, A. de Visser, and M.S. Golden, *Micro-metric electronic patterning of a topological band structure using a photon beam*, (**2015**) Sci. Rep., 5, 16309

7. **Y. Pan**, D. Wu, J.R. Angevaare, H. Luigjes, E. Frantzeskakis, N. de Jong, E. van Heumen, T.V. Bay, B. Zwartsenberg, Y.K. Huang, M. Snelder, A. Brinkman, M.S. Golden and A. de Visser, *Low carrier concentration crystals of the topological insulator $Bi_{2-x}Sb_xTe_{3-y}Se_y$: a magnetotransport study*, (**2014**) New J. Phys., 16, 123035
   [Chapter 4]

8. M. Snelder, C.G. Molenaar, **Y. Pan**, D. Wu, Y.K. Huang, A. de Visser, A.A. Golubov, W.G. van der Wiel, H. Hilgenkamp, M.S. Golden, A. Brinkman, *Josephson supercurrent in a topological insulator without a bulk shunt*, (**2014**) Supercond. Sci. Technol., 27, 104001

9. **Y. Pan**, A.M. Nikitin, T.V. Bay, Y.K. Huang, C. Paulsen, B.H. Yan and A. de Visser, *Superconductivity and magnetic order in the noncentrosymmetric half-Heusler compound ErPdBi*, (**2013**) Europhys. Lett., 104, 27001
   [Chapter 6]

10. E. Frantzeskakis, N. de Jong, B. Zwartsenberg, Y.K. Huang, **Y. Pan**, X. Zhang, J.X. Zhang, F.X. Zhang, L.H. Bao, O. Tegus, A. Varykhalov, A. de Visser and M.S. Golden, *Kondo hybridization and the origin of metallic states at the (001) surface of SmB_6*, (**2013**) Phys. Rev. X, 3, 041024

11. **Y. Pan**, X.H. Gong, Y.J. Chen, Y.F. Lin, J.H. Huang, Z.D. Luo and Y.D. Huang, *Polarized spectroscopic properties of Er^{3+}:$BaGd_2(MoO_4)_4$*, (**2012**) Opt. Mater., 34, 1143-1147

12. **Y. Pan**, Y.J. Chen, Y.F. Lin, X.H. Gong, J.H. Huang, Z.D. Luo and Y.D. Huang, *Structure, spectral properties and laser performance of Tm^{3+} doped $Li_3Ba_2La_3(WO_4)_8$*, (**2012**) CrystEngComm., 14, 3930-3935

Acknowledgements

In the end, I would like to gratefully acknowledge and thank all the people who have helped me during the 4 years of my Ph.D. Without your professional and kind support I would not have been able to successfully complete my Ph.D thesis.

First I would like to express my sincere gratitude to my supervisor Dr. Anne de Visser and promotor Prof. Mark Golden for offering me the great opportunity to join in the Quantum Matter group as a Ph.D candidate. Dear Anne, thank you very much for introducing me to the fascinating world of quantum matter, particularly the novel topological materials. Thank you very much for your kind guidance with great patience in the course of the work, from helping me get familiar with the experimental techniques and understand the physics problems to carefully checking and correcting my manuscript. Your immense knowledge, insight and perseverance towards scientific research were invaluable, by which I am both consciously and unconsciously influenced and motivated to keep moving forward in my life. Thank you for supporting me to attend different international conferences within my research field, which gave me a great opportunity to present my results, broaden my view and enlarge my network. Thank you for helping me adapt to a new scientific and social environment. Likewise, I am very grateful to Prof. Mark Golden. Thank you very much for your constant support and constructive comments in my research, my education and my work. Every time, after a "tough" discussion with you, I would have a clearer view and better understanding about the problems at hand. Thank you for your encouragement to challenge myself, which strengthened me a lot. Thank you for helping me improve my English, using your precious time to practice with me.

Thanks Dr. Yingkai Huang and Dr. Dong Wu for your high quality samples, without which I would not be able to conduct my experiments. Thanks Dr. Erik van Heumen for your valuable discussions in the group meetings. Your passion on research inspired and motivated me to work harder. Thanks Dr. Emmanouil Frantzeskakis for your nice work on the angle resolved photoemission spectroscopy measurements on $Bi_{2-x}Sb_xTe_{3-y}Se_y$ samples and for your great advice and suggestions. Thanks Hugo Schlatter and Huib Luigjes for your kind assistance in some sample preparation and characterization.

As regards to collaborations outside the university, I would like to thank Prof. Alexander Brinkman and his research group at the University of Twente for great discussions and all the productive collaborations. Many thanks to Dr. Steffen Wiedmann, Dr. Alessandro Puri and Dr. Uli Zeitler at the Radboud University for their kind help in conducting the high magnetic field experiments, to Dr. Binghai Yan at the Max Planck Institute for Chemical Physics of Solids, Germany for helping calculate the electronic structure of ErPdBi, and to Dr. Yoshitaka Matsushita and Dr. Takashi Naka at the National Institute for Materials Science, Japan for doing the low temperature X-ray diffraction measurements.

I would also like to acknowledge all staff members of the Van der Waals-Zeeman Institute for all the help they did to make my research work smoothly. Thanks to Gerrit Hardeman, Johan Mozes, Tijs van Roon and many others from the mechanical and electronic workshops for support and Rita Vinig, Anne Marieke, Natalie Wells, Fatima Ouazza and Ineke Baas for all administration assistance.

I would like to thank all members of my thesis committee for your time, interest and comments as regards to the manuscript.

Furthermore, I would like to thank the friendly Ph.D colleagues and Postdoc researchers in the Quantum Matter group, with whom I spent most of my Ph.D time. I enjoyed very much working with you all. We helped each other in difficulties, discussed problems and shared opinions. I will never forget the good times we had in various social gatherings and activities, such as coffee breaks, lunch club, BBQs etc. Artem, thanks for your assistance in the daily lab work, for your bicycle guide to the lab in the first month of my Amsterdam life, and for your kind help in many aspects in social life. I enjoyed working and discussing with you. I could also not forget you, Bay, for the kind help with the experiment when I started my work in the lab and for the special Vietnamese food. Thanks Nick for your kind help, your well-cooked pizza and the big TV screen with the movie Matrix. Golden flowers, Shyama and Alona, thanks for your company, encouragement and help. Shyama, I will always remember your suggestion on my English improving and your delicious Indian dishes. Alona, you are great at dancing and always have a lot of fun games to play. Thanks Bo for your kind help, nice discussion and encouragement. I would also like to thank many other people in the group: Erik, Berend, George, Gijsbert, Roos, Peter, Vincent, Joran, Vinh, Xingyu, Shrawan and Dona. I am also thankful to other people within the IoP: Zhongcheng, Shan, Rens, Bart, Arnon, Alex, Benjamin and Chunchia. Another group of people I wish to express my sincere gratitude to are my Chinese friends, whom I have met in the Netherlands. Thank you all for the warm relationships and making me feel at home.

My special thanks to my beloved family: my parents, my sisters and my husband Bin Xiao for their constant support, encouragement and love.